Impact of 3D Stellar Macrophysics: Gigayear White Dwarf Cooling Uncertainties and Minutes-to-Hours IGW Signatures in Massive Star Variability

by

Praneet Pathak
BS-MS, IISER Mohali, India, 2022

A Thesis Submitted in Partial Fulfillment of the
Requirements for the Degree of

MASTER OF SCIENCE

in the Department of Physics and Astronomy

We acknowledge and respect the Lək̓ʷəŋən (Songhees and Xʷsepsəm/Esquimalt) Peoples on whose territory the university stands, and the Lək̓ʷəŋən and W̱SÁNEĆ Peoples whose historical relationships with the land continue to this day.

Impact of 3D Stellar Macrophysics: Gigayear White Dwarf Cooling Uncertainties and Minutes-to-Hours IGW Signatures in Massive Star Variability

by

Praneet Pathak
BS-MS, IISER Mohali, India, 2022

Supervisory Committee

Dr. Falk Herwig, Supervisor
(Department of Physics and Astronomy)

Dr. Pavel Kovtun, Departmental Member
(Department of Physics and Astronomy)

Abstract

Three-dimensional stellar physics affects observable stellar phenomena across different timescales. This thesis studies these effects through two investigations: gigayear-scale uncertainties in white dwarf cooling that affect galactic age determinations, and minutes-to-hours internal gravity wave signatures that produce variability in massive star light curves. These studies show how 3D physical processes, often neglected in one-dimensional stellar models, introduce uncertainties that limit our ability to extract reliable information from stellar observations.

White dwarfs serve as cosmic clocks for determining ages of stellar populations. Current practice reports cooling ages with uncertainties from observational errors in temperature and mass measurements, neglecting uncertainties in cooling models themselves. We expected that uncertainties in core composition profiles would dominate cooling age errors. However, investigation of twelve model parameters using `MESA` shows that envelope hydrogen and helium layer thicknesses contribute more to cooling age uncertainties than core composition variations. For a $0.6\,M_{\odot}$ white dwarf, model uncertainties reach 0.8 Gyr at 4000 K, comparable to observational uncertainties. This sensitivity analysis shows how one-dimensional parameter studies can identify physical processes that require three-dimensional investigations to understand their impact on stellar evolution. This 1D investigation identifies key sources of systematic uncertainty in white dwarf age determinations, providing guidance for future observational and theoretical studies. The insights gained from such parameter studies inform the design of targeted 3D simulations that focus on the most physically significant processes identified through the sensitivity analysis.

Massive main-sequence stars show stochastic low-frequency variability in their light curves, but the physical mechanisms remain debated. Competing theories propose core convection-driven internal gravity waves versus subsurface convection as the source. 3D `PPMstar` simulations of a $25\,M_{\odot}$ zero-age main-sequence star enable comparison between theoretical predictions and observational power spectra. Our simulations reproduce spectral characteristics that are qualitatively and quantitatively similar to observations, with two orders of magnitude power variation across frequencies. Controlled experiments isolating different stellar regions show that internal gravity waves excited at subsurface convective boundaries, rather than core convection, dominate the low-frequency excess. This finding resolves a question in massive star asteroseismology and validates the capability of 3D simulations to model observable stellar phenomena.

These investigations show how computational stellar physics can identify and quantify uncertainties that limit astronomical applications. The white dwarf study provides uncertainty

estimates for galactic chronometry, while the massive star simulations establish a validated framework for interpreting asteroseismic observations. Both works show the importance of understanding model limitations in stellar physics applications.

Table of Contents

List of Tables

List of Figures

Acknowledgements

First, I want to thank my family back home in India for always supporting and encouraging me throughout this journey. I cannot thank my supervisor, Prof. Falk Herwig, enough for being so kind and supportive during my Master's program. He is very understanding and helped me a lot in learning how to do science. I am very grateful to Dr. Simon Blouin, who I worked with on my first paper. We had many helpful discussions, and he patiently taught me the basics of the `PPMstar` code. I want to thank Prof. Paul Woodward for creating this amazing `PPMstar` code and for the interesting one-on-one meetings where he shared his knowledge and helped me understand how the code works. I also want to thank my friend Joshua Issa for helping me so much with coding and for all our great discussions. Special thanks to Dr. Pavel Denissenkov for teaching me the `GYRE` code and always being there to help when I had problems. I am thankful to all the members of the Computational Stellar Astrophysics (CSA) group for our weekly meetings and their helpful suggestions. Finally, I want to thank my friend group *Batkaein*, who stayed in touch with me and helped me stay sane.

Dedication

I dedicate this thesis to my beloved village Kaphalet,
situated in the beautiful hills of the Himalayas in India.

Chapter 1

Introduction

1.1 Overview and Motivation

Stars serve as the sites of element nucleosynthesis in the universe. Through nuclear fusion processes occurring in their interiors, stars transform primordial H and He into heavier elements that constitute the building blocks of planets and life (Arnett, 1996; Woosley et al., 2002). Despite stellar evolutionary timescales ranging from millions to billions of years, astronomical observations combined with theoretical modeling enable the study of stellar structure and evolution from Earth within our lifetimes.

According to the standard cosmological model, the Big Bang occurred approximately 13.8 billion years ago, producing primarily H (∼75% by mass) and He (∼25% by mass), with trace amounts of Li and Be through Big Bang nucleosynthesis (Cyburt et al., 2016; Fields et al., 2020). The first stars, known as Population III stars, formed from the gravitational collapse of primordial gas clouds composed exclusively of these light elements at redshifts $z \sim 20-30$ (Bromm, 2013).

Stellar explosions and winds enrich the interstellar medium with heavy elements, providing the raw material for subsequent generations of stars. Contemporary stellar populations contain metals (elements heavier than He) inherited from previous stellar generations. Figure 1.1 shows a rough illustration of the periodic table color-coded by the origin of the elements in the Solar System.

This complex chemical evolution spans multiple astrophysical domains, from Big Bang nucleosynthesis through Population III star formation, galactic chemical evolution, and ongoing stellar along with other nucleosynthesis. Each stage represents an active area of research that could refine our understanding of nucleosynthesis.

Stellar evolution proceeds through distinct phases determined by initial mass, metallicity, and other physical parameters. Stars with masses $M < 8M_{\odot}$ evolve through hydrogen

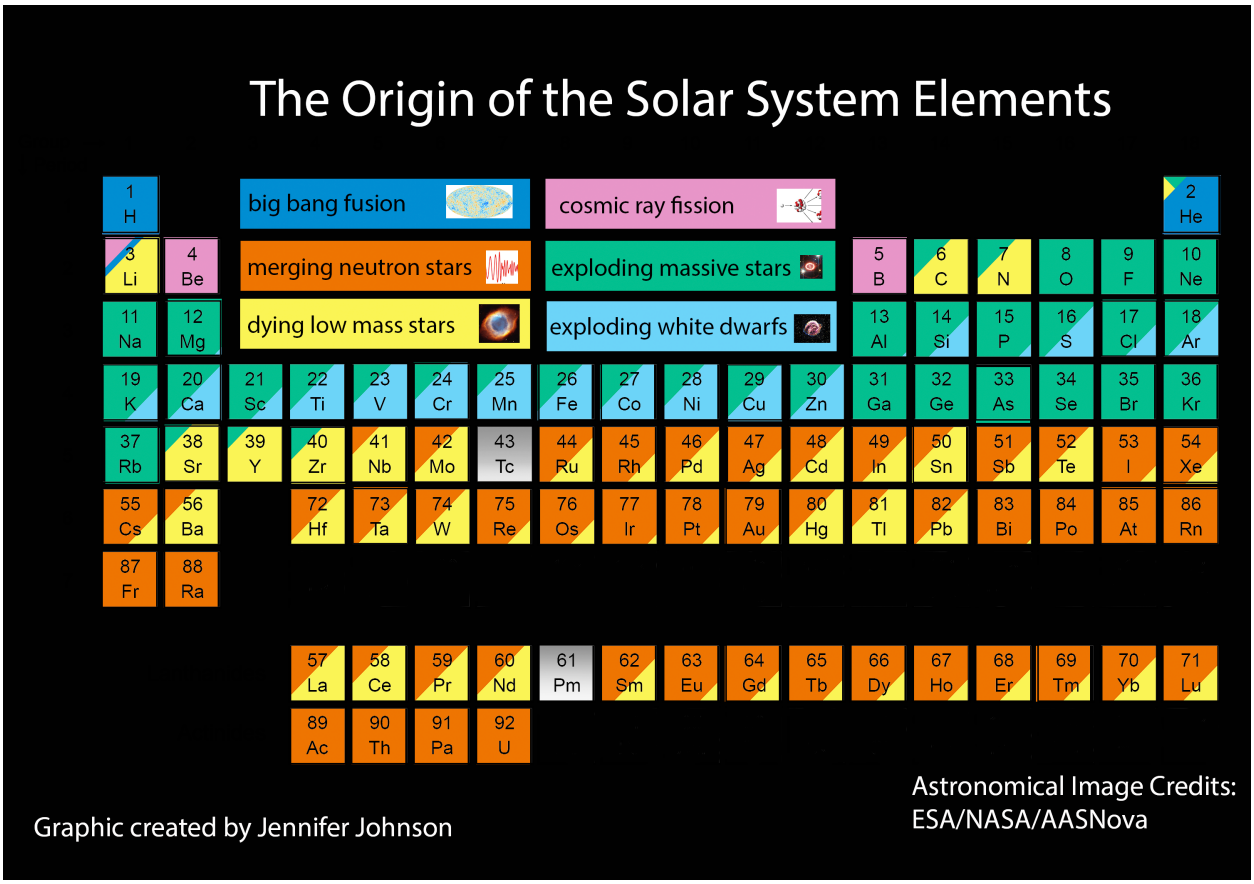

Figure 1.1: Periodic table elements with different nucleosynthesis sites. Image taken from https://blog.sdss.org/2017/01/09/origin-of-the-elements-in-the-solar-system/.

burning, helium burning, and eventually form white dwarfs (Herwig, 2013). More massive stars ($M > 8M_{\odot}$) proceed through successive nuclear burning stages, synthesizing elements up to iron through fusion processes (Kippenhahn et al., 2013). The final fate of these stars depends critically on their initial mass: stars with $8M_{\odot} < M < 25M_{\odot}$ typically undergo core-collapse supernovae, while more massive stars may directly collapse to black holes (Heger et al., 2003; Smartt, 2009; Peters and Hirschi, 2013).

Stellar evolution modeling requires solving the coupled partial differential equations governing stellar structure: mass conservation, hydrostatic equilibrium, energy generation and transport, and compositional changes (Hansen et al., 2004). These equations cannot be solved analytically except in highly simplified cases, necessitating numerical approaches.

Computational advances have enabled increasingly sophisticated stellar evolution calculations. One-dimensional stellar evolution codes solve the stellar structure equations under assumptions of spherical symmetry, hydrostatic equilibrium, and local thermodynamic equi-

librium. Convective energy transport is typically treated using mixing length theory (MLT), which parameterizes turbulent convection through a characteristic mixing length (Böhm-Vitense, 1958; Cox and Giuli, 1968). Many 1D stellar evolution codes like `MESA` (Modules for Experiments in Stellar Astrophysics) (Paxton et al., 2011a, 2013a, 2015a, 2018a, 2019a) have reproduced observed stellar properties including main sequence lifetimes, evolutionary tracks in the Hertzsprung-Russell diagram, and stellar yields (Dotter, 2016; Choi et al., 2016).

However, current computational limitations prevent full three-dimensional simulations of complete stellar evolution. The relevant physical processes span spatial scales from centimeters (turbulent eddies) to stellar radii ($\sim 10^{11}$ cm), and temporal scales from hours (convective turnover) to gigayears (nuclear burning). This multi-scale, multi-physics nature makes three-dimensional stellar evolution modeling computationally prohibitive with current resources.

Consequently, 3D hydrodynamic simulations are typically restricted to specific evolutionary phases or regions of stars due to computational limitations, using initial conditions derived from 1D models. The computational expense of full three-dimensional stellar evolution necessitates strategic selection of simulation targets where three-dimensional effects are expected to provide insights not accessible through one-dimensional modeling. Prior to conducting computationally intensive 3D simulations, systematic parameter studies using 1D stellar evolution codes can identify the most critical physical processes and uncertain parameters for specific astrophysical questions.

Understanding convective boundary mixing (CBM) during the core helium burning phase is crucial for accurate white dwarf cooling models, as it determines the carbon-to-oxygen composition profile of white dwarf cores. Blouin et al. (2024) conducted the first full-sphere 3D hydrodynamics simulations of core helium burning stars using `PPMSTAR`, investigating two different CBM prescriptions: `MESA`'s predictive mixing and convective premixing schemes. Their simulations revealed that semiconvective layers are dominated by internal gravity waves that produce no measurable mixing, while overshooting motions from the convective core gradually erase semiconvective interfaces on timescales much shorter than evolutionary phases. This finding implies that current cooling models using semiconvective prescriptions systematically underestimate core homogeneity and oxygen abundance, directly affecting crystallization energetics and cooling timescales. The resulting uncertainties in white dwarf core composition profiles introduce systematic errors of approximately 1 Gyr in age determinations, highlighting the need for comprehensive uncertainty quantification in white dwarf cooling models.

The white dwarf cooling age uncertainty study presented in Chapter 2 exemplifies a sen-

sitivity analysis, employing `MESA` to quantify the impact of various uncertain stellar evolution parameters, such as core C–O composition, trace core ^{22}Ne composition, envelope He and H thickness, and conductive opacities, on white dwarf cooling timescales. This 1D investigation identifies key sources of systematic uncertainty in white dwarf age determinations, providing essential guidance for future observational and theoretical studies. The insights gained from such parameter studies subsequently inform the design of targeted 3D simulations that focus on the most physically significant processes identified through the sensitivity analysis.

Additionally, 1D stellar evolution models provide the initial conditions required for 3D hydrodynamic simulations, establishing the baseline stellar structure from which 3D effects can be investigated.

The 3D hydrodynamic simulations of massive main-sequence stars presented in Chapter 3 demonstrate this approach, where we investigate the physical origin of observed stochastic low-frequency variability in the power spectra of O- and B-type stellar light curves. These simulations enable direct comparison with observational data and address specific astrophysical phenomena that cannot be adequately modeled using 1D approaches, such as the excitation and propagation of internal gravity waves and their interaction with convective regions.

1.2 Stellar Evolution Theory

The modeling of stellar evolution requires several fundamental assumptions that significantly simplify the complex physical processes occurring in stellar interiors.It is assumed that stars are isolated systems with no gravitational interactions from nearby companions, neglecting binary effects including mass transfer, tidal forces, and orbital evolution. Magnetic fields are omitted from consideration, excluding magnetohydrodynamic processes and magnetic pressure contributions to hydrostatic equilibrium. Stellar rotation is neglected, eliminating centrifugal forces, meridional circulation, and rotational mixing processes. We further assume spherical symmetry, excluding asphericity effects such as convective asymmetries and surface inhomogeneities. Hydrostatic equilibrium is assumed throughout stellar interiors, neglecting dynamical instabilities and pulsational phenomena. Local thermodynamic equilibrium is assumed, requiring that radiation and matter maintain thermal equilibrium on timescales much shorter than evolutionary timescales. Stellar winds and mass loss processes are either neglected or treated as prescribed boundary conditions rather than self-consistently coupled phenomena. Chemical evolution is treated through simplified nuclear reaction networks, often employing reduced isotope sets that may not capture the full complexity of

nucleosynthesis pathways, etc.

While these assumptions do not accurately represent the full complexity of real stellar systems, they provide a tractable framework that retains sufficient physical complexity to yield meaningful predictions about stellar structure, evolution, and observable properties.

The most significant limitation of these assumptions is that one-dimensional stellar evolution models cannot capture three-dimensional macroscopic physics effects. These 3D effects include turbulent convection, magnetic field interactions, stellar rotation, and aspherical mass loss processes. The inability to model these 3D phenomena represents a fundamental constraint on our understanding of stellar evolution. This thesis addresses this limitation by investigating 3D macroscopic physics effects in stellar systems.

1.2.1 Stellar structure equations

The matter inside stars exists in an extremely hot and dense plasma state, and its dynamics, can be described using the equations of fluid dynamics. The complete set of stellar structure equations under these assumptions are:

$$v \cdot \nabla X_i =$$

$$\mathrm{X}_i\big(\rho,\, T,\, \{X_j\}\big)$$

$$\frac{\partial \rho}{\partial t} + \nabla \cdot (\rho\, \mathbf{v}) = 0 \qquad \frac{\partial \mathbf{v}}{\partial t} + \mathbf{v} \cdot \nabla \mathbf{v} = -\frac{1}{\rho}\nabla P - \nabla \Phi \qquad \frac{\partial (\rho\, E)}{\partial t} + \nabla \cdot \big[\mathbf{v}\,(\rho\, E + P)\big] = -\nabla \cdot \big(k\, \nabla T\big) + \rho\, \epsilon_{\mathrm{nuc}} - \rho\, \epsilon_\nu \qquad \nabla^2 \Phi = 4$$

$$\mathrm{v} \cdot \nabla X_i =$$

$$\mathrm{X}_i\big(\rho,\, T,\, \{X_j\}\big)$$

In the above equations, $\rho(\mathbf{x}, t)$ denotes the mass density, and $\mathbf{v}(\mathbf{x}, t)$ is the fluid velocity vector field. The pressure is represented by $P(\mathbf{x}, t)$, and $\Phi(\mathbf{x}, t)$ is the gravitational potential, determined by Poisson's equation. The total specific energy is denoted by $E = e + \frac{1}{2}|\mathbf{v}|^2$, where $e(\mathbf{x}, t)$ is the specific internal energy. The temperature is denoted by $T(\mathbf{x}, t)$, and $k(\mathbf{x}, t)$ represents the thermal conductivity (or radiative diffusivity, depending on the context, which we will discuss later). The terms $\epsilon_{\mathrm{nuc}}(\rho, T, \{X_j\})$ and $\epsilon_\nu(\rho, T, \{X_j\})$ represent the specific nuclear energy generation rate and specific neutrino loss rate, respectively. The nuclear energy generation rate is calculated as $\epsilon_{\mathrm{nuc}} = \sum_k Q_k \langle \sigma v \rangle_k n_i n_j$, where Q_k is the energy released per reaction, $\langle \sigma v \rangle_k$ is the thermally averaged reaction rate coefficient that depends exponentially on temperature, and n_i, n_j are number densities of reacting nuclei determined

by density and composition. The neutrino loss rate includes contributions from various processes such as plasma neutrino emission, photoneutrino processes, and pair annihilation, each with distinct temperature and density dependencies. The quantity $X_i(\mathbf{x}, t)$ is the mass fraction of the i-th nuclear species, and its source term $\dot{X}_i(\rho, T, \{X_j\})$ represents changes due to nuclear reactions. All fields are generally functions of both spatial position $\mathbf{x}$ and time t, unless otherwise noted.

Equation (1.2.1) represents local mass conservation expressed as the continuity equation. This equation can be written in integral form as:

$$\frac{d}{dt}\int_V \rho \, dV = -\oint_S \rho \mathbf{v} \cdot \hat{\mathbf{n}} \, dS, \tag{1.5}$$

which states that the total integrated mass inside any closed surface S increases or decreases over time if there is net flux of mass flowing in or out normal to the surface.

Equation (1.2.1) represents Newton's second law $\mathbf{F} = m\mathbf{a}$ written for an infinitesimal fluid element. The pressure gradient term $-\frac{1}{\rho}\nabla P$ and the gravitational force term $-\nabla\Phi$ constitute the two force terms acting on the fluid element. Viscous terms could appear on the right-hand side; however, they are neglected for stellar interiors as the Reynolds numbers are quite high for stellar plasma, $\sim 10^{16}$, therefore viscous effects are negligible (Kippenhahn et al., 2013).

Equation (1.2.1) represents local energy conservation. The first term on the right-hand side is the thermal/radiative diffusion term. The conductivity can be written as having both thermal and radiative components: $k = k_{\text{th}} + k_{\text{rad}}$. The thermal conductivity k_{th} represents electron conduction, which is relevant for white dwarfs. The interaction of radiation with matter is treated in the diffusive approximation, valid for stellar interiors where the photon mean free path is much smaller than the scale heights of fluid variables. This approximation breaks down near stellar photospheres where the photon mean free path becomes comparable to or larger than local scale heights. In the diffusive approximation, the radiative conductivity is written as:

$$k_{\text{rad}} = \frac{16\sigma T^3}{3\kappa\rho} \tag{1.6}$$

where σ is the Stefan-Boltzmann constant, T is the temperature, κ is the Rosseland mean opacity, and ρ is the density.

The opacity quantifies the interaction between matter and radiation, fundamentally determining the radiative energy transport within stellar interiors. While opacity is inherently frequency-dependent due to varying electromagnetic spectrum interactions with matter, stel-

lar evolution calculations employ frequency-integrated (Rosseland mean) opacities. In hot, dense stellar plasmas, the dominant radiative processes involve electrons through four primary mechanisms:

1. **Electron scattering** encompasses Thomson scattering in the non-relativistic regime and Compton scattering for relativistic conditions, where photons scatter off free electrons.

2. **Free-free absorption** occurs when a free electron absorbs a photon and transitions to a higher energy state, with the inverse process (bremsstrahlung) resulting in photon emission.

3. **Bound-free absorption**, or photoionization, involves photon absorption leading to electron removal from an atom, while the reverse process constitutes radiative recombination.

4. **Bound-bound absorption** represent photon absorption by bound electrons transitioning between discrete energy levels, subsequently followed by photon emission through either collisional de-excitation or spontaneous radiative decay.

The opacity coefficient incorporates contributions from all these radiative processes, computed as functions of local density, temperature, and chemical composition to accurately model stellar radiative transfer.

Equation (1.2.1) represents the gravitational Poisson equation, expressing Newton's law of gravitation. The Poisson equation is computationally challenging to solve numerically alongside other partial differential equations due to its non-local nature. For practical purposes, its spherical solution $\Phi(r) = -GM(r)/r$ is often used directly in the force balance equation (1.2.1).

Equation (1.2.1) describes the time evolution of mass fractions of chemical species X_i in stars. This equation states that local changes in a chemical species (e.g., ^{16}O) result from either advection/mixing processes due to fluid dynamics or production/destruction via nuclear reactions.

If we count the total number of independent variables in equations 1.2.1, 1.2.1, 1.2.1, 1.2.1, and 1.2.1, the independent variables are $\rho(\mathbf{x}, t)$, $\mathbf{v}(\mathbf{x}, t)$ (3 components in 3D), $P(\mathbf{x}, t)$, $\Phi(\mathbf{x}, t)$, $T(\mathbf{x}, t)$, $X_i(\mathbf{x}, t)$, and $e(\mathbf{x}, t)$. Including N species, the total number of equations is $N + 6$. However, the total number of independent variables is $N + 8$ as listed above. This system of equations is under-determined and requires additional information to make the

total number of equations equal to the total number of independent variables. The additional information comes from assuming local thermodynamic equilibrium, where via the first law of thermodynamics and assuming the fluid variables follow equations of state, the specific internal energy and pressure can be written as functions of ρ, T, and X_i: $e = e(\rho, T, X_i)$ and $P = P(\rho, T, X_i)$. Therefore, the additional information from equations of state completes the system of stellar structure equations.

The equations of state for a mixture of photon and ideal gas are:

$$e(\rho, T, \mu) = \frac{R\,T}{(\gamma - 1)\,\mu} + \frac{a\,T^4}{\rho} \tag{1.7}$$

$$P(\rho, T, \mu) = \frac{R\,\rho\,T}{\mu} + \frac{a\,T^4}{3} \tag{1.8}$$

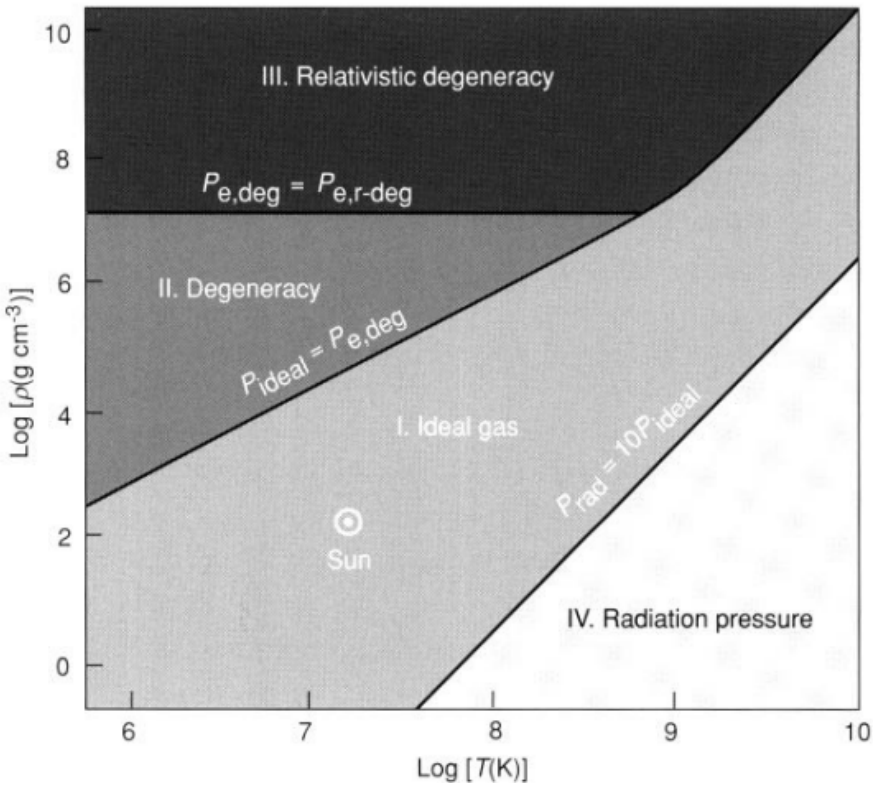

Figure 1.2: Temperature-density plane showing regions with dominant ideal or non-ideal effects. Figure taken from Prialnik (2009).

In these equations, R is the gas constant, γ is the adiabatic index, a is the radiation constant, and μ is the mean molecular weight. Non-ideal effects such as electron degeneracy

may need to be included in the equations of state depending upon the stellar phase and the relative non-ideal contribution. Figure 1.2 shows the density-temperature plane divided into regions where individual ideal/non-ideal effects are dominant.

For a partially or fully ionized gas, the ideal gas pressure receives contributions from both ions and free electrons:

$$P = \frac{\rho R T}{\mu} \tag{1.9}$$

where the mean molecular weight μ accounts for all particles present in the gas. This can be expressed as:

$$\frac{1}{\mu} = \frac{1}{\mu_{\rm ion}} + \frac{1}{\mu_e} \tag{1.10}$$

where $\mu_{\rm ion}$ and μ_e are the mean molecular weights of ions and electrons, respectively.

The ionic contribution is defined as:

$$\frac{1}{\mu_{\rm ion}} = \sum_i \frac{X_i}{A_i} \tag{1.11}$$

where X_i is the mass fraction and A_i is the atomic mass of the i-th ionic species. The electron contribution is given by:

$$\frac{1}{\mu_e} = \sum_i \frac{X_i Z_i}{A_i} \tag{1.12}$$

where Z_i is the atomic number of the i-th species, representing the number of free electrons per ion.

For example, consider a fully ionized hydrogen-helium mixture with mass fractions $X = 0.7$ and $Y = 0.3$. The ionic contribution yields $\mu_{\rm ion}^{-1} = 0.7/1 + 0.3/4 = 0.775$, while the electron contribution gives $\mu_e^{-1} = 0.7 \times 1/1 + 0.3 \times 2/4 = 0.85$. The total mean molecular weight becomes $\mu^{-1} = 0.775 + 0.85 = 1.625$, resulting in $\mu = 0.615$ (Kippenhahn et al., 2013).

1.2.2 Timescales in stellar evolution

Understanding the different timescales in stellar evolution is essential because they determine which physical processes dominate at different evolutionary phases and which approximations are valid in stellar modeling.

The temporal evolution of stellar structure is governed by three distinct physical processes, each characterized by a specific timescale. This treatment follows the framework

presented in Prialnik (2009). These timescales are defined through the general relation

$$\tau = \phi/\dot{\phi}, \tag{1.13}$$

where ϕ represents a physical quantity and $\dot{\phi}$ denotes its time derivative. The three fundamental timescales in stellar evolution are the dynamical, thermal, and nuclear timescales.

Dynamical timescale

The dynamical timescale $\tau_{\rm dyn}$ characterizes the time required for significant structural rearrangement of the stellar configuration under gravitational forces. This timescale corresponds to the time for a gravitational disturbance to propagate across the stellar radius or, equivalently, the free-fall collapse time. The dynamical timescale is expressed as:

$$\tau_{\rm dyn} \approx \frac{R}{v_{\rm esc}} \approx \sqrt{\frac{1}{G\bar{\rho}}} \tag{1.14}$$

where R is the stellar radius, $v_{\rm esc} = \sqrt{2GM/R}$ is the escape velocity, G is the gravitational constant, M is the stellar mass, and $\bar{\rho}$ is the mean stellar density.

For the Sun, with $M_\odot = 1.989 \times 10^{30}$ kg and $R_\odot = 6.96 \times 10^8$ m, the mean density is $\bar{\rho}_\odot = 3M_\odot/(4\pi R_\odot^3) = 1.41 \times 10^3$ kg m^{-3}. The dynamical timescale becomes:

$$\tau_{\rm dyn} = \sqrt{\frac{1}{G\bar{\rho}_\odot}} = 3.26 \times 10^3 \text{ s} \approx 54 \text{ minutes} \tag{1.15}$$

Thermal timescale

The thermal timescale $\tau_{\rm th}$, also known as the Kelvin-Helmholtz timescale, represents the time required for the star to radiate away its total thermal energy content at the current luminosity. This timescale governs thermal equilibrium adjustments within the stellar interior and is given by:

$$\tau_{\rm th} \approx \frac{U}{L} \approx \frac{GM^2}{RL} \tag{1.16}$$

where U is the total thermal energy content and L is the stellar luminosity. The approximation $U \sim GM^2/R$ follows from the virial theorem for a self-gravitating gas.

For the Sun, the thermal timescale is:

$$\tau_{\rm th} = \frac{GM_\odot^2}{R_\odot L_\odot} = 9.9 \times 10^{14} \text{ s} \approx 31.4 \times 10^6 \text{ years} \tag{1.17}$$

Nuclear timescale

The nuclear timescale $\tau_{\rm nuc}$ characterizes the time required to convert a significant fraction of the stellar mass into energy through nuclear processes. This timescale represents the longest evolutionary phase and is expressed as:

$$\tau_{\rm nuc} \approx \frac{\varepsilon M c^2}{L} \tag{1.18}$$

where ε is the nuclear burning efficiency (typically $\varepsilon \sim 0.007$ for hydrogen burning via the proton-proton chain) and c is the speed of light.

For the Sun, assuming hydrogen burning efficiency $\varepsilon = 0.007$, the nuclear timescale becomes:

$$\tau_{\rm nuc} = \frac{0.007 \times M_\odot c^2}{L_\odot} = \frac{0.007 \times 1.989 \times 10^{30} \times (2.998 \times 10^8)^2}{3.83 \times 10^{26}} = 3.3{\times}10^{17}\ \text{s} \approx 1.0{\times}10^{10}\ \text{years} \tag{1.19}$$

However, nuclear reaction timescales can become very short when temperatures are high enough, particularly in convective reactive environments where new fuel is mixed into convection zones. For example, during hydrogen ingestion into helium shell convection, the reaction timescale becomes as short as the convective turnover timescale, approximately 15 minutes.

Hierarchical ordering and stellar evolution

Under typical main-sequence conditions (core H burning phase), these timescales exhibit a hierarchical ordering:

$$\tau_{\rm dyn} \ll \tau_{\rm th} \ll \tau_{\rm nuc} \tag{1.20}$$

This ordering implies that structural adjustments occur rapidly compared to thermal evolution, which in turn proceeds much faster than nuclear evolution. Consequently, stars maintain hydrostatic equilibrium (dynamical equilibrium) and thermal equilibrium on timescales much shorter than nuclear evolution.

However, this hierarchical relationship does not hold universally throughout stellar evolution. During catastrophic events such as core collapse in massive stars or helium flash episodes in low-mass stars, the dynamical timescale can become comparable to or shorter than the thermal timescale, leading to rapid structural reorganization. Similarly, during advanced evolutionary phases when nuclear fuel becomes depleted in stellar cores, the nuclear timescale approaches the thermal timescale, resulting in complex interactions between

thermal and nuclear processes.

The nuclear timescale represents the fundamental clock governing stellar evolution, as nuclear processes provide the energy source that sustains stellar luminosity against gravitational collapse. The pace of stellar evolution is therefore predominantly determined by the rate of nuclear energy generation relative to the energy loss through radiation.

This hierarchical ordering of timescales explains why complete stellar evolution cannot be simulated in three dimensions. The nuclear timescale spans billions of years, while 3D simulations are limited to dynamical timescales of hours to years due to computational constraints. Therefore, 3D simulations can only capture short episodes of stellar evolution, requiring the use of 1D models to follow the long-term evolutionary sequence.

1.2.3 1D stellar evolution

This section follows the formulation presented in Kippenhahn et al. (2013) and Herwig (2013). Solving the complete stellar structure equations discussed in Section 1.2.1 in three spatial dimensions is computationally prohibitive due to several complications. These include the necessity to resolve turbulent convection processes, the enormous dynamical range between characteristic timescales discussed in Section 1.2.2, and the inherent complexity of three-dimensional magnetohydrodynamic phenomena in stellar interiors.

Therefore, these equations are typically solved under the assumption of spherical symmetry using the Lagrangian mass coordinate m, representing the enclosed mass within radius r. In one dimension (the radial dimension), the stellar structure equations reduce to:

$$\frac{\partial r}{\partial m} = \frac{1}{4\pi r^2 \rho} \tag{1.21}$$

$$\frac{\partial P}{\partial m} = -\frac{Gm}{4\pi r^4} \tag{1.22}$$

$$\frac{\partial l}{\partial m} = \epsilon_{\mathrm{nuc}} + \epsilon_{\mathrm{grav}} - \epsilon_{\nu} \tag{1.23}$$

$$\frac{\partial T}{\partial m} = -\frac{GmT}{4\pi r^4 P}\nabla \tag{1.24}$$

$$\frac{\partial X_i}{\partial t} = \left.\frac{\partial X_i}{\partial t}\right|_{\mathrm{nuc}} + \frac{\partial}{\partial m}\left[\left(4\pi r^2 \rho\right)^2 D(m) \frac{\partial X_i}{\partial m}\right] \tag{1.25}$$

In these equations, $r(m,t)$ is the radius at mass coordinate m, $P(m,t)$ is the pressure, $l(m,t)$ is the luminosity passing through the mass shell m, $T(m,t)$ is the temperature, and $X_i(m,t)$ represents the mass fraction of nuclear species i. The density $\rho(m,t)$ is related to

radius through equation (1.21). The nuclear energy generation rate per unit mass is denoted by $\epsilon_{\rm nuc}$, the gravitational energy release rate per unit mass by $\epsilon_{\rm grav}$, and ϵ_ν represents the neutrino energy loss rate per unit mass. The first term in the last equation is the change in the mass fraction of species i as a result of nuclear reactions and second term represents its change as a result of mixing processes, characterized by a diffusion coefficient D(m). The temperature gradient ∇ is defined as:

$$\nabla = \frac{d\ln T}{d\ln P} \tag{1.26}$$

The value of ∇ depends on the dominant energy transport mechanism. For radiative transport, $\nabla = \nabla_{\rm rad}$, where:

$$\nabla_{\rm rad} = \frac{3\kappa l P}{64\pi^2\sigma G m T^4} \tag{1.27}$$

where κ is the opacity and σ is the Stefan-Boltzmann constant. For convective transport, $\nabla = \nabla_{\rm ad}$, the adiabatic temperature gradient, which depends on the equation of state. We will discuss more about this in the following Section 1.2.4.

These equations are solved implicitly assuming hydrostatic equilibrium using timesteps of order $\min(\tau_{\rm th}, \tau_{\rm nuc})$. The implicit treatment ensures numerical stability across the vast range of evolutionary timescales while maintaining physical consistency.

`MESA` (Modules for Experiments in Stellar Astrophysics) (Paxton et al., 2011a, 2013a, 2015a, 2018a, 2019a; Jermyn et al., 2023) is one such open-source 1D stellar evolution code widely used by the stellar evolution community. `MESA` provides a comprehensive framework for modeling stellar structure and evolution from pre-main-sequence to advanced evolutionary phases.

There are numerous scenarios where the 1D assumption becomes inadequate. For example, turbulent processes in convective regions, effects of stellar rotation, magnetic field interactions, and binary mass transfer. In such cases, non-spherically symmetric effects become significant, necessitating 3D treatment of the stellar structure equations to capture the full complexity of stellar physics.

1.2.4 Energy Transport

This section follows the framework presented in García-Berro and Althaus (2013). Energy transport in stellar interiors proceeds through three primary mechanisms: radiation, conduction, and convection. Each mechanism operates under distinct physical conditions and dominates in different stellar regions depending on local thermodynamic properties.

Radiative transport

Radiative energy transport occurs through photon diffusion in the stellar plasma. The mean free path of photons in stellar interiors is approximated as:

$$\ell_{\rm ph} = \frac{1}{\kappa_{\rm rad}\,\rho} \tag{1.28}$$

where $\kappa_{\rm rad}$ is the radiative opacity and ρ is the density. Typical values of photon mean free paths are of order 1 cm, which are extremely small compared to stellar radii. For the Sun, with $R_\odot = 6.96 \times 10^{10}$ cm, the ratio $\ell_{\rm ph}/R_\odot \sim 10^{-10}$, justifying the diffusion approximation.

Due to these small photon mean free paths, radiative transport can be treated as a diffusive process. The radiative energy flux is given by:

$$F_{\rm rad} = -\frac{4\pi}{3\,\kappa_{\rm rad}\,\rho}\nabla B = -\frac{4\,a\,c\,T^3}{3\,\kappa_{\rm rad}\,\rho}\nabla T \tag{1.29}$$

where B is the integrated Planck function, a is the radiation constant, c is the speed of light, and T is the temperature.

In the spherically symmetric case, the luminosity is related to the flux by $l = 4\pi r^2 F_{\rm rad}$, and the radiative diffusion equation becomes:

$$\frac{dT}{dr} = -\frac{3\,\kappa_{\rm rad}\,\rho\,l}{16\,\pi\,a\,c\,T^3\,r^2} \tag{1.30}$$

The radiative flux can also be expressed as:

$$F_{\rm rad} = -D$$

$\mathrm{d(a\,T^4)}dr(1.31)$ where aT^4 is the radiation energy density and D is the diffusion coefficient defined as:

$$D = \frac{c}{3\,\kappa_{\rm rad}\,\rho} = \frac{1}{3}c\,\ell_{\rm ph} \tag{1.32}$$

Conductive transport

Conductive energy transport occurs through particle collisions resulting from thermal motions. This mechanism becomes significant in degenerate stellar environments, particularly through electron conduction in white dwarf interiors. The conductive flux is expressed as:

$$F_{\rm cd} = -D_e$$

dTdr (1.33)

where D_e is the electron thermal diffusivity.

Analogous to radiative opacity, a conductive opacity can be defined such that:

$$F_{\rm cd} = -\frac{4\,a\,c\,T^3}{3\kappa_{\rm cd}\,\rho}\frac{dT}{dr} \tag{1.34}$$

where $\kappa_{\rm cd}$ is the conductive opacity.

The total energy flux combines radiative and conductive contributions:

$$F = F_{\rm rad} + F_{\rm cd} = -\frac{4\,a\,c\,T^3}{3\,\kappa_{\rm tot}\,\rho}\frac{dT}{dr} \tag{1.35}$$

where the total opacity is defined as:

$$\frac{1}{\kappa_{\rm tot}} = \frac{1}{\kappa_{\rm rad}} + \frac{1}{\kappa_{\rm cd}} \tag{1.36}$$

When conduction dominates over radiation ($\kappa_{\rm cd} \ll \kappa_{\rm rad}$), the total opacity approaches the conductive opacity: $\kappa_{\rm tot} \approx \kappa_{\rm cd}$.

For combined radiative and conductive transport, it is convenient to express the temperature gradient from equation (1.30) in the dimensionless form:

$$\nabla_{\rm rad} = \frac{d\,\ln T}{d\,\ln P} = \frac{3\,\kappa_{\rm tot}\,l\,P}{16\,\pi\,a\,c\,G\,m\,T^4} \tag{1.37}$$

where $\nabla_{\rm rad}$ represents the logarithmic temperature gradient in hydrostatic equilibrium when energy transport occurs through radiation and conduction.

Convective transport

Convective energy transport occurs through large-scale fluid motions driven by buoyancy forces in gravitational fields. The onset of convection is determined by the stability of fluid elements against vertical displacements.

Consider a fluid element displaced from its equilibrium position within the stellar interior due to internal perturbations. The stability criterion depends on the restoring force acting on the displaced element. If the net force acts toward the original position, the configuration remains convectively stable, and the fluid element oscillates around equilibrium. Conversely, if the net force acts away from the original position, the element continues moving, indicating

convective instability.

The condition for convective stability can be expressed as:

$$\left(\frac{d\rho}{dr}\right)_{\rm int} > \left(\frac{d\rho}{dr}\right)_{\rm ext} \tag{1.38}$$

where $(d\rho/dr)_{\rm int}$ represents the internal density gradient of the displaced fluid element and $(d\rho/dr)_{\rm ext}$ is the external environmental density gradient. Gravitational forces provide the restoring mechanism, opposing buoyant forces when this inequality is satisfied.

Using the equation of state $\rho = \rho(P, T, \mu)$, where μ is the mean molecular weight, the stability condition can be expressed through the Ledoux criterion:

$$\frac{d\ln T}{d\ln P} < \nabla_{\rm ad} + \frac{\varphi}{\delta}\frac{d\ln \mu}{d\ln P} \tag{1.39}$$

where $\nabla_{\rm ad}$ is the adiabatic temperature gradient, and φ and δ are *thermodynamic derivatives* defined as:

$$\nabla_{\rm ad} = \left(\frac{d\ \ln T}{d\ \ln P}\right)_s = \frac{P\,\delta}{C_P\,\rho\,T} \tag{1.40}$$

$$\varphi = \left(\frac{\partial \ln \rho}{\partial \ln \mu}\right)_{P,T} \tag{1.41}$$

$$\delta = -\left(\frac{\partial \ln \rho}{\partial \ln T}\right)_{P,\mu} \tag{1.42}$$

This derivation assumes that displaced fluid elements undergo adiabatic processes, maintaining constant composition and energy during displacement due to insufficient time for thermal or chemical exchange with surroundings.

For chemically homogeneous regions where $d\mu/dr = 0$, the Ledoux criterion reduces to the Schwarzschild criterion:

$$\frac{d\ln T}{d\ln P} < \nabla_{\rm ad} \tag{1.43}$$

When $\nabla_{\rm rad} > \nabla_{\rm ad}$, convective instability develops, and energy transport proceeds through convective motions rather than radiative diffusion.

1.2.5 Convective Boundary and the Mixing Length Theory

This section draws from the treatment presented in García-Berro and Althaus (2013). The convective boundary represents the interface separating radiative or conductive regions from convective zones within stellar interiors. Understanding the physics of these boundaries and

the modeling of convective transport constitutes a fundamental challenge in stellar evolution theory.

Convective boundary determination

From the Schwarzschild and Ledoux criteria established in the previous section, a chemically homogeneous stellar region becomes convectively unstable due to two primary mechanisms: enhanced energy generation from nuclear reactions (exemplified by core convection in main-sequence stars during hydrogen burning) or elevated opacity values (such as subsurface convection zones associated with opacity bumps in hydrogen, helium, or iron ionization regions near stellar surfaces).

For chemically homogeneous regions, the Schwarzschild boundary is defined as the location where:

$$\nabla_{\rm rad} = \nabla_{\rm ad} \tag{1.44}$$

More generally, the Ledoux convective boundary occurs where:

$$\nabla_{\rm rad} = \nabla_{\rm ad} + \frac{\varphi}{\delta}\frac{d\ln\mu}{d\ln P} \tag{1.45}$$

This boundary represents the location where downward gravitational forces exactly balance upward buoyant forces acting on fluid parcels. However, fundamental Newtonian mechanics tells us that zero net force does not necessarily imply zero velocity. Consequently, convective plumes possess finite velocities and penetrate beyond the formally defined convective boundary through a process termed convective overshooting.

Figure 1.3 illustrates this penetration of convective plumes observed in three-dimensional hydrodynamic simulations, revealing the inadequacy of sharp boundary prescriptions in capturing the true extent of convective mixing.

Mixing Length Theory

The calculation of the convective temperature gradient $\nabla_{\rm conv}$ required for determining convective flux represents a significant theoretical challenge. 1D stellar evolution codes typically employ the mixing-length theory (MLT) to model convective transport, despite its inherent limitations.

The mixing-length theory assumes that convective flux transport occurs through the largest-scale fluid motions. These macroscopic fluid elements, when averaged over time, traverse a characteristic distance $\ell_{\rm MLT}$ before dissipating their energy to the surrounding

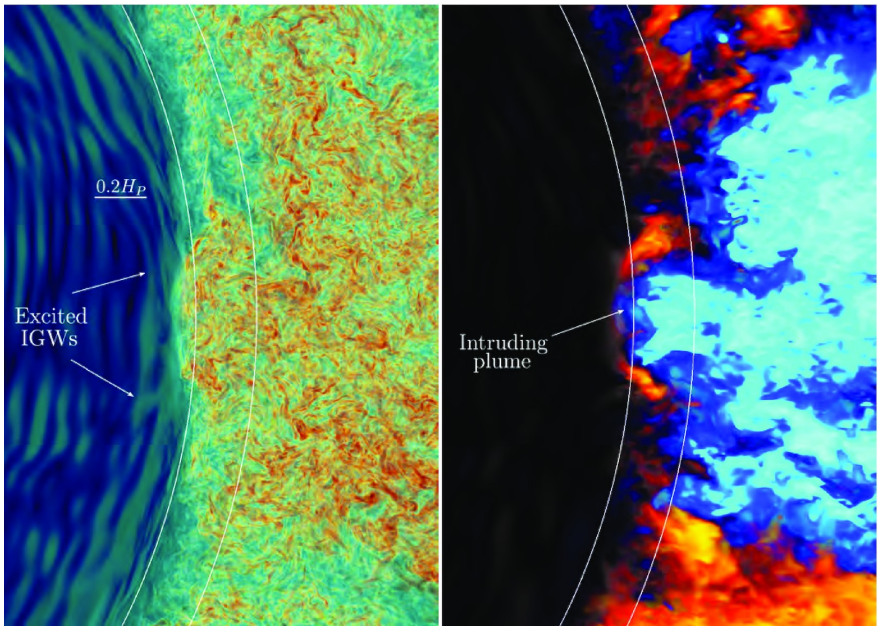

Figure 1.3: Volume rendering of vorticity magnitude (left) and radial velocity (right) from a high-resolution (2880^3) 3D hydrodynamic `PPMstar` simulation of a $1.2\,M_\odot$ red giant branch star. The radially outer circle indicates the Schwarzschild convective boundary. Figure taken from Blouin et al. (2023).

medium. This mixing length is parametrized as:

$$\ell_{\rm MLT} = \alpha_{\rm MLT} H_P \tag{1.46}$$

where $\alpha_{\rm MLT}$ is a free parameter not predicted by the theory and H_P is the pressure scale height at the convective boundary.

The free parameter $\alpha_{\rm MLT}$ is typically calibrated using solar observations, yielding $\alpha_{\rm MLT} \approx 1.6$. This value is often applied to other stellar masses and evolutionary phases in 1D stellar evolution calculations, representing an extrapolation of a highly simplified theoretical framework whose general validity remains uncertain.

Diffusive overshooting models

A more sophisticated approach treats convective overshooting as a diffusive process. A commonly employed two-parameter diffusive model defines the mixing coefficient as:

$$D(r) = \begin{cases} D_0 & \text{for } r_{\rm CB} - \ell_{\rm ov} \leq r \leq r_{\rm CB} (\text{overshoot/penetration region}) \\ D_0 \exp\left(-\frac{2(r-r_{\rm CB})}{f_{\rm ov} H_P}\right) & \text{for } r > r_{\rm CB} \end{cases} \tag{1.47}$$

where $r_{\rm CB}$ denotes the convective boundary radius, $\ell_{\rm ov}$ represents the extent of the fully mixed overshooting region, D_0 is the reference diffusion coefficient, and $f_{\rm ov}$ characterizes the exponential decay scale length in units of pressure scale heights.

The free parameters $\ell_{\rm ov}$ and $f_{\rm ov}$ require calibration against observational constraints or limited 3D hydrodynamic simulations, which remain computationally expensive and therefore restricted to specific evolutionary phases and stellar configurations.

Limitations of mixing-length theory

The fundamental limitations of mixing-length theory are aptly summarized by Cox and Giuli (1968):

> "The mixing length theory represents an extreme simplification of the actual physical process of convection. One does not therefore expect quantitative results derived on the basis of this theory to have high accuracy or reliability. One of the principal sources of uncertainty in the theory is the value to be used for the mixing length itself... The theory does, however, yield a qualitatively reasonable picture of convective heat transfer... It is therefore simply for want of a better theory that astrophysicists commonly use the mixing length theory in the construction of stellar models in spite of its drawbacks. Moreover, stellar models constructed on the basis of the mixing length theory do not show any obvious contradictions with observations. Let it be emphasized again, however, that users of this theory should be well aware of the possible quantitative unreliability of results obtained by its use."

This assessment underscores the necessity for improved theoretical frameworks and highlights the importance of three-dimensional hydrodynamic simulations in advancing our understanding of convective processes in stellar interiors.

1.2.6 Evolutionary phases

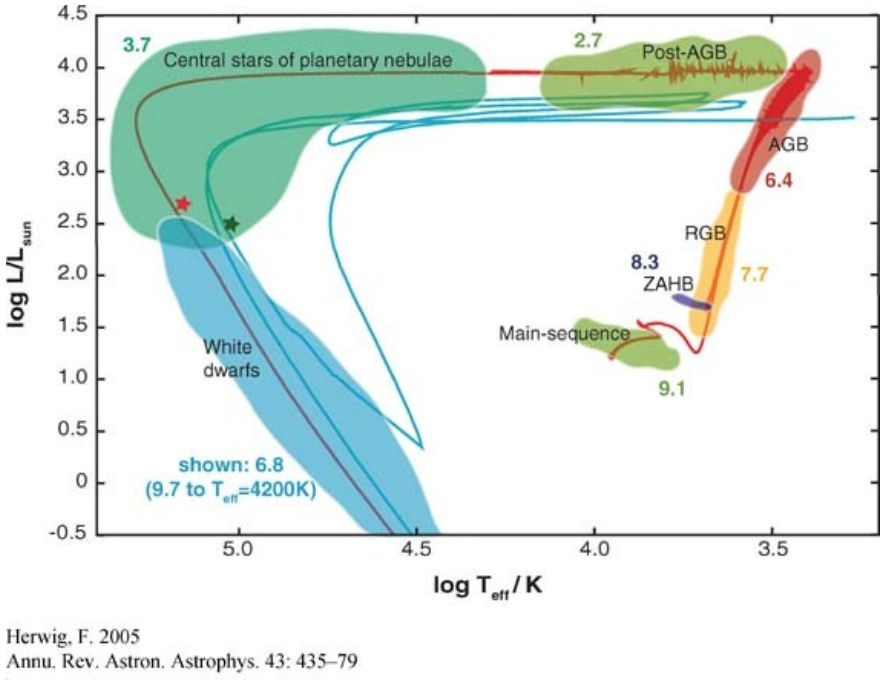

Figure 1.4: Hertzsprung-Russell diagram showing the complete evolutionary track of a $2\,M_\odot$ star from main sequence to white dwarf phase. Numbers indicate the logarithm of approximate phase durations in years. Figure taken from Herwig (2005).

This section is inspired from Herwig (2005). The stellar structure equations presented in the preceding sections are solved with varying initial parameters including stellar mass, metallicity (defined as the mass fraction of elements heavier than helium), and initial composition. The solutions provide the temporal evolution of stellar properties, which can be visualized through the Hertzsprung-Russell (HR) diagram plotting luminosity versus effective temperature, as illustrated in Figure 1.4.

In the theoretical framework, stellar luminosity, radius, and effective temperature are related through the Stefan-Boltzmann law:

$$L = 4\pi R^2 \sigma T_{\text{eff}}^4 \tag{1.48}$$

where σ is the Stefan-Boltzmann constant.

The stellar evolutionary sequence begins with the core hydrogen burning phase, commonly referred to as the main sequence. During this phase, hydrogen is converted to helium through either the proton-proton chain reaction in lower-mass stars or the CNO cycle in

more massive stars. The main sequence represents the longest evolutionary phase in stellar lifetimes. For the Sun, the main sequence lifetime is approximately $\tau_{\rm MS} \approx 10^{10}$ years, corresponding to the nuclear timescale discussed in Section 1.2.2.

Following core hydrogen exhaustion, nuclear energy generation in the stellar core ceases, initiating gravitational contraction on the Kelvin-Helmholtz timescale $\tau_{\rm KH}$. The star transitions to hydrogen shell burning, where nuclear reactions continue in a thin shell surrounding the inert helium core. This configuration drives the stellar envelope expansion and surface cooling, causing the star to evolve toward the red giant branch (RGB) in the HR diagram.

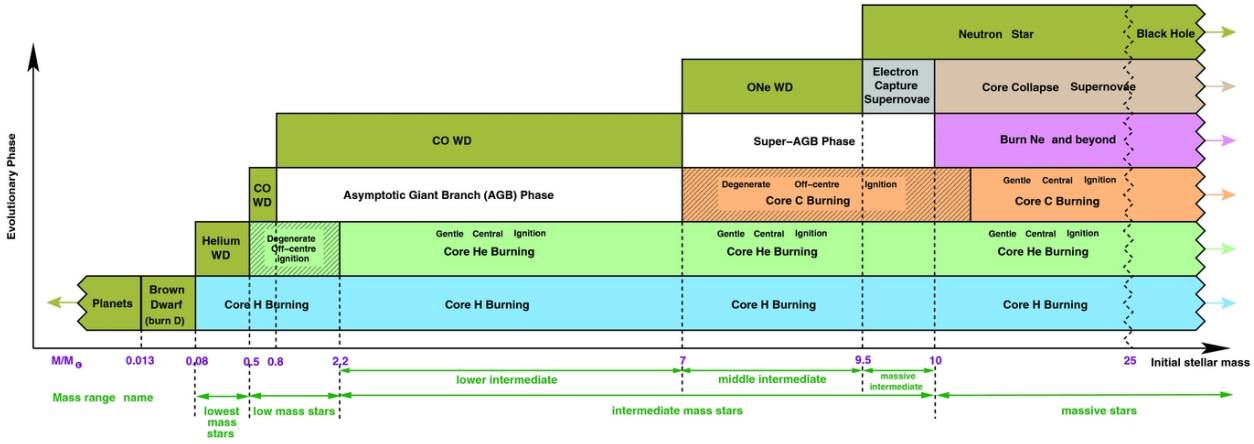

Figure 1.5: A diagram illustrating how a star's mass controls which nuclear fusion processes occur during its lifetime (assuming solar metallicity), and what type of stellar remnant it becomes after death. Image taken from Karakas and Lattanzio (2014)

The subsequent evolutionary pathway depends critically on the initial stellar mass, as depicted in Figure 1.5. The boundaries depicted in the figure are often not well defined theoretically, as they are sensitive to specific parameters including mass loss rates and mixing algorithms employed in the models. When the contracting core reaches sufficient temperature and density, helium burning may commence through the triple-alpha process, producing carbon and oxygen. However, whether core helium ignition occurs depends on the competition between nuclear heating and electron degeneracy pressure.

For stars with initial masses $M \lesssim 1.8\,M_{\odot}$, the helium core becomes electron degenerate before reaching helium ignition temperatures. These stars experience a violent degenerate helium flash, subsequently settling onto the zero-age horizontal branch (ZAHB). More massive stars ignite core helium burning in a non-degenerate, thermally stable manner.

The core helium burning phase proceeds significantly more rapidly than core hydrogen burning, typically lasting approximately one-tenth the main sequence lifetime. This phase produces a carbon-oxygen core through helium fusion reactions. Stars with initial masses

$M \lesssim 8\,M_\odot$ do not achieve sufficient core temperatures for carbon ignition, resulting in electron degenerate carbon-oxygen cores.

Following core helium exhaustion, stars enter the asymptotic giant branch (AGB) phase, characterized by helium shell burning surrounding the inert carbon-oxygen core. The AGB phase exhibits complex thermal pulse cycles due to the interaction between hydrogen and helium burning shells. Eventually, the stellar envelope is expelled through stellar winds and thermal pulses, exposing the hot central core. The remnant evolves into a white dwarf composed primarily of carbon and oxygen, though oxygen-neon white dwarfs can form from more massive progenitors approaching the Chandrasekhar limit. White dwarf evolution and properties are examined in greater detail in Section 1.5.

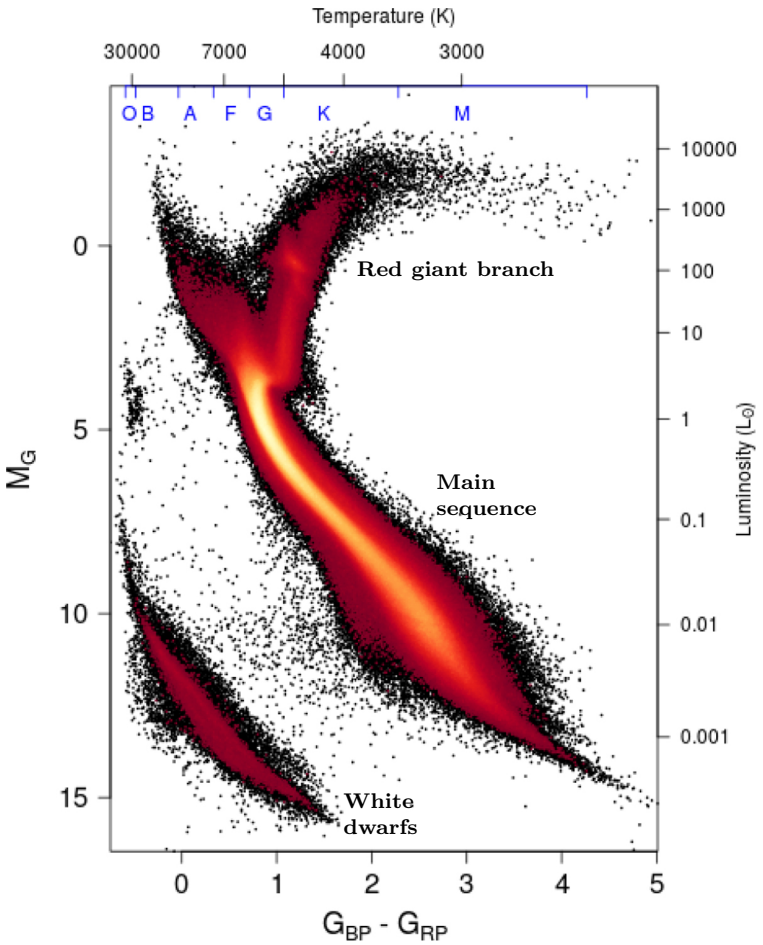

Figure 1.6: Observational Hertzsprung-Russell diagram from the European Space Agency (ESA) satellite Gaia's Data Release 2, showing 4.3 million low-extinction stars. The color scale represents stellar density. Approximate temperature and luminosity scales for main sequence stars are indicated on the top and right axes. Figure taken from Gaia Collaboration et al. (2018a).

The theoretical predictions from stellar evolution models require observational validation. While luminosity and effective temperature are not directly observable quantities, they can be inferred from photometric measurements. Observers construct color-magnitude diagrams analogous to theoretical HR diagrams, plotting apparent or absolute magnitudes against color indices, as exemplified in Figure 1.6.

Observational HR diagrams reveal prominent stellar concentrations corresponding to different evolutionary phases. The diagonal main sequence concentration reflects the extended duration of core hydrogen burning relative to other evolutionary phases. Additional concentrations appear for RGB stars and white dwarfs, consistent with theoretical predictions.

A fundamental distinction exists between theoretical and observational HR diagrams. Theoretical diagrams trace the temporal evolution of individual stars, while observational diagrams represent instantaneous distributions of stellar populations with varying ages and masses. Isochrones provide the critical link between these perspectives, representing theoretical tracks of constant age for stellar populations with different initial masses, enabling direct comparison between evolutionary models and observational data.

1.3 `PPMstar` simulations

`PPMstar` is a three-dimensional explicit gas dynamics code that solves the Euler equations using a higher-order Godunov method called the Piecewise Parabolic Method (PPM) (Colella and Woodward, 1984; Woodward et al., 2015, 2019; Andrassy et al., 2020, 2022; Mao et al., 2024). The code solves equations (1.2.1), (1.2.1), (1.2.1), (1.2.1), and (1.2.1) along with the equations of state. However, the gravitational Poisson equation is not solved directly; instead, its spherically symmetric solution $\Phi(r) = -GM(r)/r$ is employed in the momentum equation.

The equations are solved in a perturbative fashion with respect to a base state, enabling computations in 32-bit precision while maintaining high accuracy. The PPM method is a flux-conserving approach that solves 3D Euler equations in discretized grid cells using directional splitting. The fluid variables are assumed to follow parabolic profiles within individual grid cells, hence the name "piecewise parabolic method."

The `PPMstar` code incorporates a fourth-order Piecewise Parabolic Boltzmann (PPB) scheme to track two distinct fluids with different mean molecular weights. This capability proves particularly valuable for studying species mixing across convective boundaries and compositional interfaces.

The code has been applied to simulate various stellar evolutionary phases across multiple

research publications. These applications include post-AGB stellar environments (Herwig et al., 2011, 2014), O-burning shell convection (Jones et al., 2017), He shell flash convection zones and hydrogen ingestion in rapidly accreting white dwarfs (Denissenkov et al., 2019), H-He shell interactions in massive Population III stars (Clarkson et al., 2019), C-O shell mergers (Andrassy et al., 2020), RGB evolution in 1.2 $M_\odot$ stars (Blouin et al., 2023), main-sequence convection in 25 $M_\odot$ stars (Herwig et al., 2023; Thompson et al., 2024; Mao et al., 2024), and core He burning in 3 $M_\odot$ stars (Blouin et al., 2024).

The Courant-Friedrichs-Lewy (CFL) condition imposes a grid-size-dependent upper bound on allowed timesteps in the simulations, ensuring that information does not propagate between nearest-neighbor grid cells within a single timestep:

$$\Delta t \leq \frac{\Delta x}{c_s} \tag{1.49}$$

where Δt is the timestep, Δx is the grid spacing, and c_s is the local sound speed.

This constraint significantly impacts computational cost scaling. Decreasing grid resolution by a factor of 2 increases the effective computational cost by a factor of $2^4 = 16$ (factors of two in each spatial dimension plus a factor of two for smaller allowed timesteps from the CFL condition). This scaling makes high-resolution simulations computationally expensive. To illustrate the computational requirements, the M424 simulation presented in Chapter 3 evolved 3800 hours of stellar time with average timesteps of approximately 2 seconds, requiring approximately 3.4 million timesteps. This simulation consumed 2.7 million core-hours of computing time.

Due to their computationally demanding nature, initial conditions for `PPMstar` simulations are typically extracted from 1D stellar evolution models calculated with `MESA`, allowing focused study of specific evolutionary phases rather than complete stellar lifetimes.

1D stellar evolution codes often predict stratifications characterized by extremely low Mach numbers ($< 10^{-5}$) within convective zones. Resolving such low Mach number flows in three-dimensional simulations that can be completed within reasonable computational timeframes proves challenging, even with access to powerful supercomputing resources. To address this limitation, nuclear heating rates are often artificially enhanced by factors like 10^3 or even larger. Multiple simulations employing different artificial heating factors demonstrate that convective velocities scale with the luminosity enhancement factor L as $L^{1/3}$. Consequently, a heating boost factor of 1000 increases convective velocities by only a factor of 10, explaining the necessity for extremely large enhancement factors in 3D stellar simulations.

1.4 Stellar Oscillations

This section is inspired from Handler (2013). Stars exhibit oscillatory behavior analogous to the vibrational modes of musical instruments such as guitar strings. However, stellar interiors are characterized by hydrostatic equilibrium, where gravitational forces balance pressure gradient forces as described by equation (1.22). Consequently, special physical mechanisms are required to drive or self-excite oscillation modes in stellar environments.

Four primary driving mechanisms have been proposed to explain stellar pulsations:

1. ε **mechanism** (Rosseland and Randers, 1938): Excitation through varying nuclear reaction rates. Compression of nuclear burning zones elevates the temperature, increasing nuclear energy generation rates. This enhanced energy production triggers expansion, which subsequently decreases pressure and energy output, reversing the initial compression and establishing oscillatory behavior.

2. κ-γ **mechanism** (Baker and Kippenhahn, 1962): Driving through opacity variations in ionization zones. When stellar material undergoes compression, increased opacity reduces radiative cooling efficiency, leading to thermal expansion. The subsequent decrease in opacity during expansion enhances cooling, restoring the initial compression phase.

3. **Convective blocking or convective driving** (Brickhill, 1991): Modulation of convective energy transport efficiency through interaction between pulsation phases and convective flows.

4. **Stochastic excitation**: Random forcing of oscillation modes through turbulent convective motions in stellar interiors.

The study of stellar oscillations and the extraction of information about stellar interiors from observational measurements of surface pulsations constitutes the field of asteroseismology. This discipline draws inspiration from terrestrial seismology, where earthquake-generated oscillation modes provide insights into Earth's internal structure and composition.

Stellar oscillation modes are understood as non-spherical perturbations superimposed on stratified mean stellar models, which remain spherically symmetric in one-dimensional treatments. In the linear perturbation framework, fluid variables are decomposed as:

$$A(r, \theta, \phi, t) = A_0(r) + A'(r, \theta, \phi, t) \tag{1.50}$$

where $A_0(r)$ represents the background stratification and $A'(r, \theta, \phi, t)$ denotes the perturbation. The perturbations are assumed to be significantly smaller than the background quantities ($A' \ll A_0$), enabling linearization of the non-linear fluid equations.

This linearization procedure yields a Sturm-Liouville type eigenvalue problem, exhibiting mathematical similarities to the Schrödinger equation for the H atom. Solving these perturbation equations produces dispersion relations connecting oscillation frequencies with corresponding wavenumbers. A comprehensive derivation of stellar oscillation modes is presented in Aerts et al. (2010).

The analysis yields both radial and non-radial solutions. Non-radial solutions, analogous to hydrogen atom wavefunctions in quantum mechanics, are proportional to spherical harmonics:

$$Y_\ell^m(\theta, \phi) = \sqrt{\frac{2\ell + 1}{4\pi} \frac{(\ell - |m|)!}{(\ell + |m|)!}} P_\ell^{|m|}(\cos\theta) e^{im\phi} \tag{1.51}$$

where ℓ is the degree ($\ell = 0, 1, 2, \ldots$), m is the azimuthal order ($m = -\ell, -\ell+1, \ldots, \ell-1, \ell$), $P_\ell^{|m|}$ are the associated Legendre polynomials, θ is the colatitude, and ϕ is the azimuthal angle.

Two major categories of non-radial pulsation modes are distinguished based on the dominant restoring force:

- **p-modes (pressure modes)**: Oscillations where pressure gradients provide the primary restoring force.
- **g-modes (gravity modes)**: Oscillations where gravitational forces constitute the dominant restoring mechanism.

Modes are commonly labeled according to their number of radial nodes or overtones, for example, p_3 denotes a p-mode with three radial nodes. Fundamental modes (f-modes) represent oscillations with no interior nodes.

The propagation characteristics of oscillation modes are governed by two characteristic frequencies: the Brunt-Väisälä frequency N and the Lamb frequency L_ℓ, defined as:

$$N^2 = -\frac{g}{\gamma P}\left(\frac{dP}{dr} - \gamma \frac{\rho g}{\gamma}\right) \tag{1.52}$$

$$L_\ell^2 = \frac{\ell(\ell + 1)c_s^2}{r^2} \tag{1.53}$$

where g is the local gravitational acceleration, γ is the adiabatic index, P is the pressure, ρ is the density, c_s is the local sound speed, and r is the radial coordinate.

The relationship between oscillation frequency ω and these characteristic frequencies determines mode classification:

- A mode with $\omega > N$ and $\omega > L_\ell$ experiences pressure as the dominant restoring force and is classified as a p-mode.
- A mode with $\omega < N$ and $\omega < L_\ell$ is classified as a g-mode.
- Modes that satisfy neither condition are evanescent and do not propagate through the stellar interior.

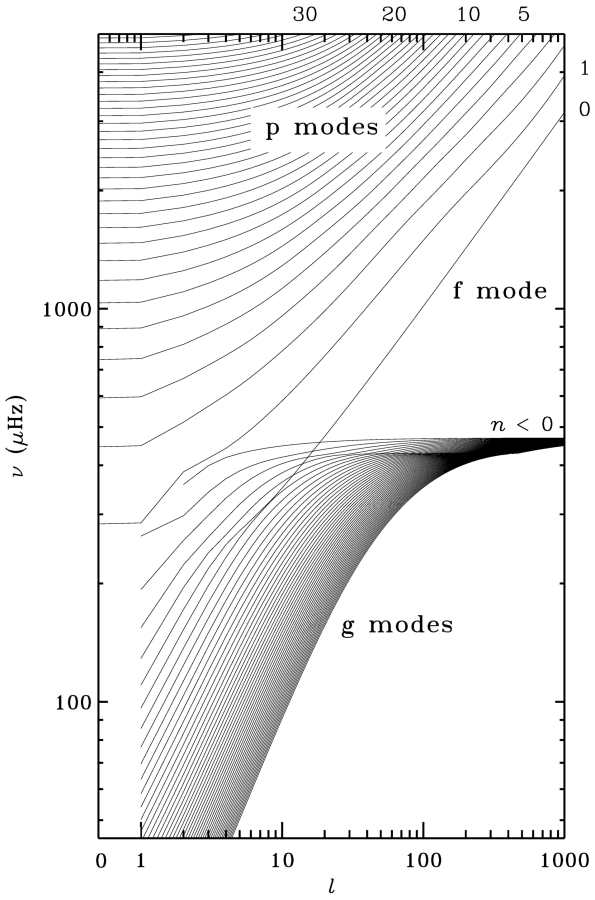

Figure 1.7: Frequency $\nu = \omega/2\pi$ - spherical harmonic degree ℓ diagram for stellar oscillation modes in a solar model, displaying p-modes (positive n) and g-modes (negative n) with labeled radial orders. Figure taken from Aerts et al. (2010).

Figure 1.7 illustrates the dispersion relation of oscillation modes computed for the Sun, demonstrating the characteristic frequency ranges for different mode types.

1.5 White Dwarf stars

This section is inspired from Blouin (2024).

1.5.1 Formation and basic properties

White dwarfs represent dense compact stellar objects formed as the final evolutionary products of stars with initial masses $M \lesssim 8\,M_\odot$ (Herwig, 2013). Following the exhaustion of nuclear fuel and the ejection of their outer envelopes during the asymptotic giant branch phase, these stellar remnants exhibit significantly reduced luminosities compared to nuclear-burning main-sequence, red giant branch, and asymptotic giant branch stars.

White dwarfs are characterized by extreme densities of approximately 10^6 g cm^{-3}, where electron degeneracy pressure provides the dominant force balancing gravitational collapse. These objects occupy the lower-left region of the Hertzsprung-Russell diagram, reflecting their high surface temperatures and low luminosities relative to main-sequence stars of comparable effective temperatures.

The fundamental physical limit governing white dwarf masses was established by Chandrasekhar (1931), who derived a critical upper mass limit of approximately $1.4\,M_\odot$ using the equation of state for extreme relativistic electron degeneracy pressure. This theoretical contribution, known as the Chandrasekhar limit, earned him the Nobel Prize in Physics in 1983. When a white dwarf approaches this mass limit, electron degeneracy pressure can no longer balance gravitational forces. The star undergoes rapid gravitational contraction, causing the carbon-oxygen core to reach ignition temperatures. This triggers explosive carbon burning throughout the core. The degenerate conditions prevent thermal expansion, causing the nuclear burning rate to increase exponentially with temperature. This thermonuclear runaway propagates throughout the entire star within seconds, resulting in a Type Ia supernova explosion.

The mass-radius relationship for white dwarfs exhibits an inverse correlation: more massive white dwarfs possess smaller radii due to enhanced gravitational compression. This relationship can be approximated using polytropic stellar structure models, yielding the scaling relation $M \propto R^{-3}$. Figure 1.8 illustrates the mass-radius relationship for white dwarfs calculated using modern one-dimensional stellar evolution codes, demonstrating the quantitative validation of this theoretical prediction.

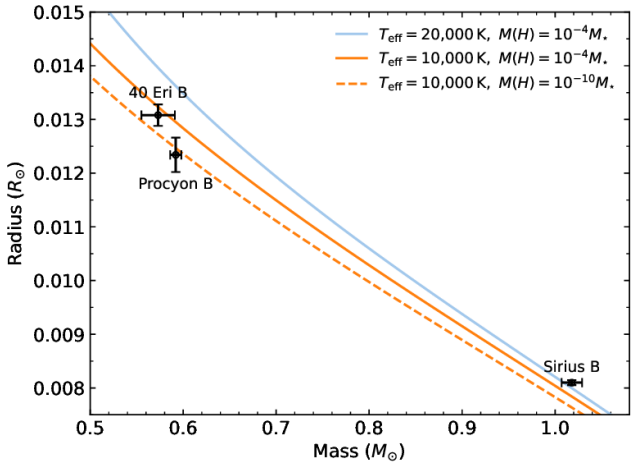

Figure 1.8: Mass-radius relationship for white dwarfs calculated using modern stellar evolution models, demonstrating the inverse correlation $M \propto R^{-3}$. Theoretical predictions are shown for different effective temperatures and hydrogen layer masses, with three observed white dwarfs indicated for comparison. Figure taken from Blouin et al. (2024).

1.5.2 Internal Structure and Composition

Figure 1.9 illustrates the typical chemical composition profile of a carbon-oxygen white dwarf, which constitutes the majority of observed white dwarf populations. The interior is predominantly composed of ^{12}C and ^{16}O, with trace amounts of ^{22}Ne (1–2%) distributed throughout the core region. This carbon-oxygen core is surrounded by a thin helium envelope, which is itself enveloped by an even thinner hydrogen layer.

The carbon-oxygen core forms as the product of helium burning during the pre-white dwarf evolutionary phases. The qualitative characteristics of the composition profile depend on several physical processes, including core and envelope helium burning, the number of thermal pulses experienced during asymptotic giant branch evolution, and mixing processes such as convection and convective overshooting or penetration from burning regions. Thermal pulses represent episodic helium burning events in the helium shell surrounding the inert carbon-oxygen core, driven by the thermal instability arising from the temperature and density dependence of the triple-alpha reaction rate.

The ^{12}C(α,γ)^{16}O reaction rate represents the most critical nuclear physics input determining the final ^{12}C/^{16}O ratio within the core. The abundance of ^{22}Ne results from α-capture on ^{14}N, where ^{14}N is produced through the CNO cycle during hydrogen burning phases. The thickness of the helium and hydrogen envelope layers depends on the extent of hydrogen burning that occurred during pre-white dwarf evolution and the mass loss efficiency of stellar winds during the asymptotic giant branch phase.

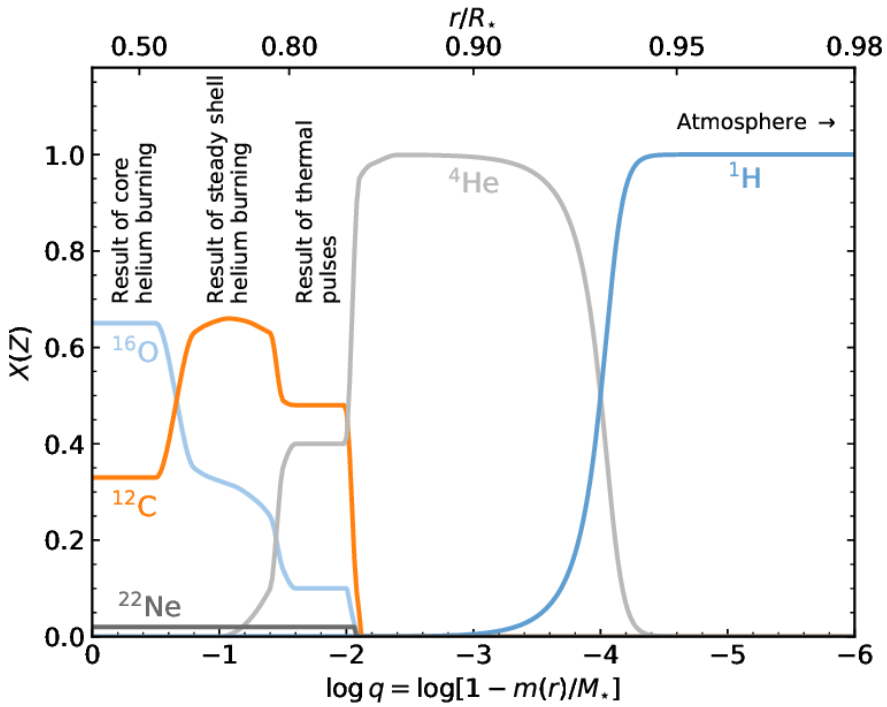

Figure 1.9: Chemical stratification of a typical C-O white dwarf interior, showing the distribution of nuclear species by mass fraction. The central region contains predominantly ^{12}C and ^{16}O with minor ^{22}Ne contributions, while the outer layers comprise ^{4}He and ^{1}H shells. Figure taken from Blouin et al. (2024).

White dwarf progenitors with initial masses approaching $\sim 10\,M_{\odot}$ may undergo core carbon burning, producing oxygen-neon cores composed primarily of ^{16}O and ^{20}Ne, along with trace amounts of ^{12}C, ^{22}Ne, ^{23}Na, and ^{24}Mg as products of carbon burning reactions. However, these oxygen-neon white dwarfs represent a rare subset of the white dwarf population.

The precise chemical stratification of white dwarf interiors remains subject to significant uncertainties arising from two primary sources: uncertainties in nuclear reaction rates, particularly the ^{12}C(α,γ)^{16}O reaction for core composition, and the uncertain treatment of convective boundary mixing in one-dimensional stellar evolution models.

1.5.3 White Dwarf Cooling

The majority of white dwarfs do not sustain nuclear burning reactions following their formation. A newly formed white dwarf represents a thermal reservoir containing substantial heat energy accumulated during preceding stellar evolutionary phases. Consequently, white dwarf evolution proceeds through a relatively simple cooling process, as illustrated in Figure 1.10,

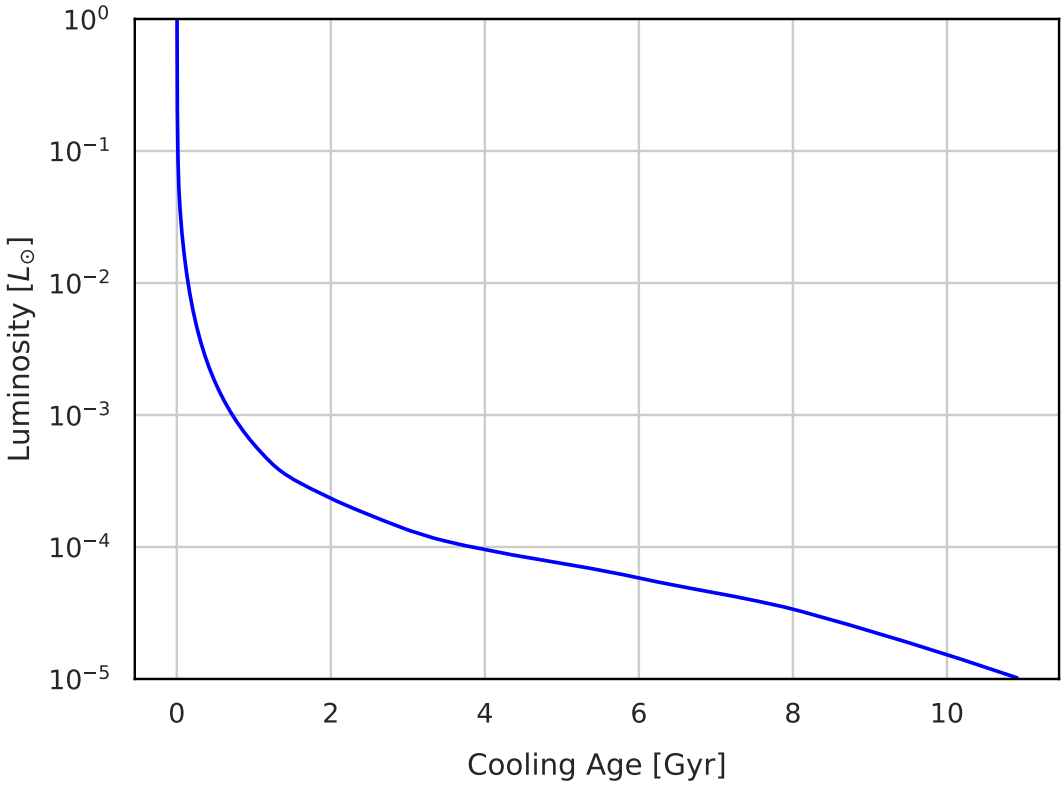

Figure 1.10: Cooling curve of a typical 0.6 $M_\odot$ white dwarf generated using `MESA`.

wherein the star gradually cools and dims over timescales of several billion years. This contrasts markedly with the complex nuclear burning phases characterizing main-sequence, red giant branch, and asymptotic giant branch evolution.

During the initial few hundred million years of cooling, neutrino emission constitutes the dominant energy loss mechanism. However, photon radiation represents the primary cooling channel throughout the majority of white dwarf evolutionary history. The fundamental simplicity of this cooling process has established white dwarfs as valuable cosmic chronometers for age determinations of stellar populations and galactic components (Winget et al., 1987; Fontaine et al., 2001; Isern, 2019).

The utility of white dwarfs as reliable age indicators is limited by incomplete understanding of pre-white dwarf evolutionary phases, as discussed in the preceding sections. The composition of a white dwarf of given mass remains subject to considerable uncertainty due to these theoretical limitations. These compositional uncertainties directly propagate into systematic errors in white dwarf age determinations.

Additional complexity arises during white dwarf cooling when the carbon-oxygen core

undergoes crystallization, a first-order phase transition that releases substantial latent heat. This energy release effectively delays cooling for a few billion years, with the magnitude of the delay depending critically on the core C-O composition ratio. The uncertain core composition therefore introduces significant systematic uncertainties in cooling age calculations.

Improving theoretical understanding of stellar evolution processes, particularly those governing core composition during helium burning phases and convective boundary mixing, will enhance the precision of white dwarf chronometry and strengthen their application as cosmic clocks.

1.6 Thesis outline

This thesis presents computational studies of stellar evolution through two complementary investigations, each forming the basis of a separate publication. Chapter 2 presents systematic uncertainties in white dwarf cooling age determinations, based on work published in the Astrophysical Journal. Chapter 3 investigates the physical origin of stochastic low-frequency variability observed in massive main-sequence stars through high-resolution three-dimensional hydrodynamic `PPMstar` simulations of a non-rotating zero-age main-sequence $25\,M_\odot$ star, based on work under preparation for publication. Finally, Chapter 4 summarizes the findings and outlines directions for future research.

Chapter 2

Quantifying Systematic Uncertainties in White Dwarf Cooling Age Determinations

The contents of this chapter are based on a paper that has been published in the Astrophysical Journal (https://iopscience.iop.org/article/10.3847/1538-4357/adc10f). This project was initiated as a course project in ASTR 501. The contributors to this paper are myself (P.P.), Dr. Simon Blouin (S.B.), and Dr. Falk Herwig (F.H.). A detailed breakdown of their contributions is described below.

Conceptualization: S.B. conceived the original idea for this paper. **Methodology:** P.P. conducted all `MESA` simulations and developed the computational framework for the analysis. **Software:** P.P. developed all Python scripts, bash scripts, and Jupyter notebooks for the analysis of simulation results. S.B. provided extensive guidance in the development of these analytical tools. **Validation:** S.B. and F.H. provided feedback on the results and their interpretation throughout the project. **Formal analysis:** P.P. conducted the formal analysis of the simulation results under the guidance of S.B. **Investigation:** P.P. conducted the primary investigation by running simulations and analyzing the results. **Writing (original draft):** P.P. wrote the initial draft of the paper with guidance and feedback from S.B. and F.H., which forms the basis of this thesis chapter. **Writing (review & editing):** S.B. subsequently modified and tailored this initial draft to produce the final version of the paper that was submitted for publication. S.B. and F.H. provided extensive comments and engaged in productive discussions throughout the project. **Supervision:** S.B. and F.H. provided supervision and guidance throughout the project development and analysis phases.

2.1 Abstract

Cooling ages of white dwarfs are routinely determined by mapping effective temperatures and masses to ages using evolutionary models. Typically, the reported uncertainties on cooling ages only consider the error propagation of the uncertainties on the spectroscopically or photometrically determined $T_{\rm eff}$ and mass. However, cooling models are themselves uncertain, given their dependence on many poorly constrained inputs. This paper estimates these systematic model uncertainties. We use `MESA` to generate cooling sequences of $0.5 - 1.0\,M_{\odot}$ hydrogen-atmosphere white dwarfs with carbon–oxygen cores under different assumptions regarding the chemical stratification of their core, the thickness of their helium envelope, their hydrogen content, and the conductive opacities employed in the calculations. The parameter space explored is constrained by the range of values predicted by a variety of stellar evolution models and inferred from asteroseismological studies. For a $0.6\,M_{\odot}$ white dwarf, we find an uncertainty of 0.03 Gyr at 10,000 K (corresponding to a 5% relative uncertainty) and 0.8 Gyr at 4000 K (9%). This uncertainty is significant, as it is comparable to the age uncertainty obtained by propagating the measurement errors on $T_{\rm eff}$ and mass for a typical white dwarf. We also separately consider the potential impact of ^{22}Ne shell distillation, which plausibly leads to an additional uncertainty of ~ 1 Gyr for crystallized white dwarfs. We provide a table of our simulation results that can be used to evaluate the systematic model uncertainty based on a white dwarf's $T_{\rm eff}$ and mass. We encourage its use in all future studies where white dwarf cooling ages are measured.

2.2 Introduction

White dwarfs represent the final evolutionary stage for the vast majority of stars. Having exhausted their nuclear fuel, they enter a long cooling phase that is relatively simple compared to earlier stages of stellar evolution (Mestel, 1952; Fontaine et al., 2001; Althaus et al., 2010). This cooling process spans billions of years and, if accurately modeled, can allow white dwarfs to be used as cosmic clocks. White dwarfs have been used to estimate the ages and star formation histories of various stellar populations (Winget et al., 1987; García-Berro et al., 2010; Kalirai, 2012; Kilic et al., 2017; Fantin et al., 2019; Isern, 2019; Cukanovaite et al., 2023), constrain the Hubble constant (Cimatti and Moresco, 2023), and date ancient planetary systems (Hollands et al., 2018; Kaiser et al., 2021; Blouin and Xu, 2022; Elms et al., 2022). However, our understanding of both the late stages of stellar evolution leading to white dwarf formation and the subsequent white dwarf cooling process remains incomplete, which limits our ability to accurately determine white dwarf cooling ages.

A first major source of uncertainty is the core composition profile of white dwarfs. This ratio is determined by the helium-burning phases of the progenitor star, where three key uncertainties come into play. First, the $^{12}C(\alpha,\gamma)^{16}O$ reaction rate is poorly constrained, leading to variations of about ± 0.1 in the central oxygen mass fraction (De Gerónimo et al., 2017; Chidester and Timmes, 2022; Pepper et al., 2022). Second, the physics of convective boundary mixing during helium burning is not well understood, affecting both the final C/O ratio and the size of the homogeneous core region (Straniero et al., 2003; Constantino et al., 2015; Salaris and Cassisi, 2017; Giammichele et al., 2022; Blouin et al., 2024). Third, the thermal pulse phase on the asymptotic giant branch introduces additional complexity, as the uncertain number of pulses influence the chemical profile of the outer region of the core (Herwig, 2000; Weiss and Ferguson, 2009; De Gerónimo et al., 2017)

Typically, WD cosmochronology involves measuring the effective temperature and mass of a white dwarf through spectroscopy, photometry, and parallax. These measurements are then mapped to age using pre-calculated cooling tracks (Pala et al., 2022; Arazimova et al., 2009; Pala et al., 2017; von Hippel et al., 2020). The observational uncertainties in effective temperature and mass propagate to the uncertainty in the determined cooling age of the WD. Often, the total age of the star is estimated using an Initial-Final Mass Relation and pre-WD lifetime (Cukanovaite et al., 2023; Tremblay et al., 2014; Fantin et al., 2019). However, this approach overlooks systematic uncertainties in white dwarf cooling models, which arise from poorly constrained inputs (Salaris, 2009). These inputs include uncertainties in the microphysics, such as conductive opacities of the envelope, resulting in Gyr-scale cooling differences at low temperatures (Cassisi et al., 2021).

The core chemical composition of a white dwarf, given a fixed mass and effective temperature ($T_{\rm eff}$), remains uncertain mainly due to poorly constrained nuclear reaction rate uncertainties and overshooting beyond the Schwarzschild boundary during convection during the core He-burning phase (Salaris and Cassisi, 2017). For example, Chidester and Timmes (2022) demonstrated that the uncertainty in the $^{12}C(\alpha,\gamma)^{16}O$ reaction rate causes variations in the core ^{16}O mass fraction by about ± 0.1. Blouin et al. (2024) examines the additional mixing across the Schwarzschild boundary by conducting 3D hydrodynamic simulations of a core helium-burning(CHeB) $3M_{\odot}$ star, Constantino et al. (2015) explained asteroseismic observation of CHeB stars using 'maximal-overshoot' scheme. Straniero et al. (2003) predicted a variation in the core ^{16}O mass fraction between 0.3 and 0.9, taking into account the uncertainties in convection theory as well as the $^{12}C(\alpha,\gamma)^{16}O$ reaction rate, Chidester et al. (2023) studied the asteroseismic signatures of $^{12}C(\alpha,\gamma)^{16}O$ reaction rates in white dwarfs, considering the effect of overshoot during the pre-white dwarf evolutionary phase.

Salaris et al. (2010) used the `BaSTI` code to study WDs with H and He envelopes, finding a 7% variation in cooling timescales due to the $^{12}C(\alpha,\gamma)^{16}O$ reaction rate uncertainty and convective overshoot. Salaris et al. (1997) showed that phase separation of C/O during crystallization can cause nearly a gigayear difference in cooling timescales. On the other hand, Giammichele et al. (2018) determined the chemical composition of few WDs from asteroseismic observations and found higher core ^{16}O mass fraction than the predictions from stellar evolution models thus indicating the need for a better understanding of the core chemical composition of WDs. De Gerónimo et al. (2019) discusses modifying nuclear reaction rates and overshoot parameters during core helium-burning to reconcile asteroseismic predictions with stellar evolution models.

Furthermore, the thickness of the hydrogen and helium layers, which governs the star's energy escape rate, is another critical factor along with the conductive opacities of the envelope. The two main conductive opacity tables used in the literature are those of Cassisi et al. (2007) and Blouin et al. (2020). Cassisi et al. (2021) studied the impact of conductive opacities on WD cooling timescales and found that they are affected by around 40-45 % and $\sim$ 25% at high and low $T_{\rm eff}$ respectively. Salaris et al. (2024) also studied the impact of conductive opacities on WD cooling in the evolutionary models which included ^{22}Ne phase separation and distillation (Blouin and Daligault, 2021).

^{22}Ne distillation during crystallization represents another significant uncertainty in white dwarf cooling. This process (Isern et al., 1991) involves separation of neutron-rich impurities from the carbon–oxygen plasma, releasing gravitational energy that delays cooling. The mechanism likely explains the Gaia "Q branch" overdensity (Gaia Collaboration et al., 2018b; Tremblay et al., 2019; Blouin et al., 2021) and NGC 6791's luminosity function (Salaris et al., 2024). Theoretical models predict 0.5–2.0 Gyr cooling delays for solar-metallicity white dwarfs (Segretain, 1996; Blouin et al., 2021), though observational confirmation of shell distillation remains missing (Venner et al., 2023).

Standard white dwarf age determination maps spectroscopic $T_{\rm eff}$ and mass measurements to pre-calculated cooling tracks (Renedo et al., 2010; Bédard et al., 2020; Salaris et al., 2022). Reported uncertainties typically reflect only observational errors (Kiman et al., 2022), neglecting systematic uncertainties in the cooling models themselves. This work quantifies these systematic uncertainties and provides results for incorporation into future studies.

This study quantifies the impact of these various uncertainties on the cooling timescales of hydrogen atmosphere WDs, emphasizing that systematic uncertainties must be included with reported cooling ages until these issues are resolved. In Section 2.3, we provide a detailed description of the methodologies used, including an explanation of the tools employed to

simulate WD cooling with the code developed by Bauer (2023). Section 2.4 discusses our findings, particularly how different input profile parameters correlate with the cooling age of white dwarfs. Finally, Section 2.5 summarizes our conclusions and outlines potential future research directions, contextualizing our findings within the wider field of white dwarf studies and astrophysics.

2.3 Methods, Simulations

In this work we have used open-source stellar evolution software instrument Modules for Experiments in Stellar Astrophysics (MESA) Paxton et al. (2011b, 2013b, 2015b, 2018b, 2019b); Jermyn et al. (2023) (version `r23.05.1`) to simulate WD evolution. This MESA version includes the implementation of carbon-oxygen phase separation and crystallization (see Bauer, 2023), which an important input physics for WD cooling. A repository of MESA inlist files and scripts used in this work can be found at the DOI 10.5281/zenodo.13831121

2.3.1 Parametrization of WD composition profiles

For parametrizing the core ^{16}O composition we have used 8-parameter Akima spline profiles as discussed in Giammichele et al. (2017). This parametrization is motivated from pre-WD evolution models and asteroseismology. We are also including a small but constant amount of ^{22}Ne in the core of the WD and whatever is left is ^{12}C. Outside the core, we add a thick layer of ^{4}He which is followed by a thin ^{1}H envelope. There the complete chemical composition profile is 11-parameter profile as shown in the Figure 2.1.

2.3.2 Restricting the parameter space

To find the suitable range of values for the 8-parameters, we have fitted it against core ^{16}O profiles of $0.6 M_{\odot}$ WD from evolutionary models (Straniero et al., 2003; Salaris et al., 2022; Renedo et al., 2010) as well as the profiles inferred from asteroseismology (De Gerónimo et al., 2017; Giammichele et al., 2022). The spread in core-O mass fraction of these profiles are shown in Figure 2.2 . We use the same range of values for the core ^{16}O's 8-parameters for all the WD masses. Oxygen abundance profiles derived from sampling these eight Akima spline parameter distributions are displayed in Figure 2.3. Each profile represents an individual stellar model subsequently evolved using `MESA`.

To determine the range for the parameter `envl_o`, we calculated $1 - \max(X_{^{12}\mathrm{C}})$ for all the fitted profiles in the outer core region. This value can be considered as the maximum value for the parameter `envl_o` parameter.

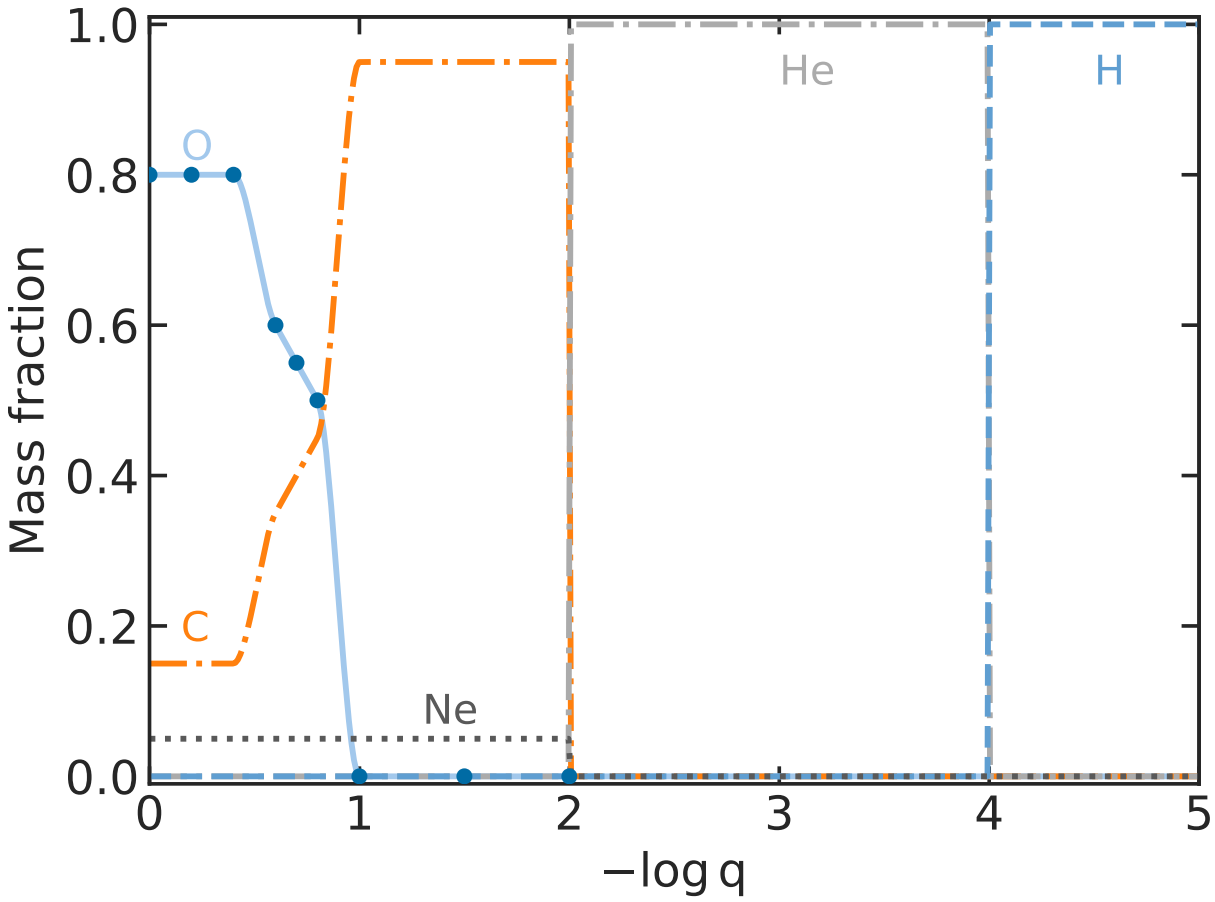

Figure 2.1: Chemical composition profile of a white dwarf (WD) with 11 parameters. The nine red dots represent data points from Giammichele et al. (2017), and the ^{16}O profile (dot-dashed blue) is interpolated using Akima splines. The green solid line, dot-dashed black line, orange dashed line, and dark pink dotted line correspond to $X_{^{12}C}$, $X_{^{4}He}$, $X_{^{1}H}$, and $X_{^{22}Ne}$, respectively.

For the range of values for ^{4}He and ^{1}H we have the upper limit as the one allowed such that it can be a WD rather than a nuclear burning AGB star. This upper limit is different for different WD masses (see Table 1 of Renedo et al., 2010). We studied hydrogen envelopes that are relatively thick (with `-log qH` ≤ 6), which is relevant for hydrogen atmosphere white dwarfs.

For the range of values for ^{22}Ne we choose it from a log-normal distribution with a mean equal to the metallicity [Fe/H], with [Fe/H] $= -0.2 \pm 0.5$. This implies Therefore the ^{22}Ne mass fraction is

$$X_{^{22}Ne} = 0.014 \times 10^{[Fe/H]}. \tag{2.1}$$

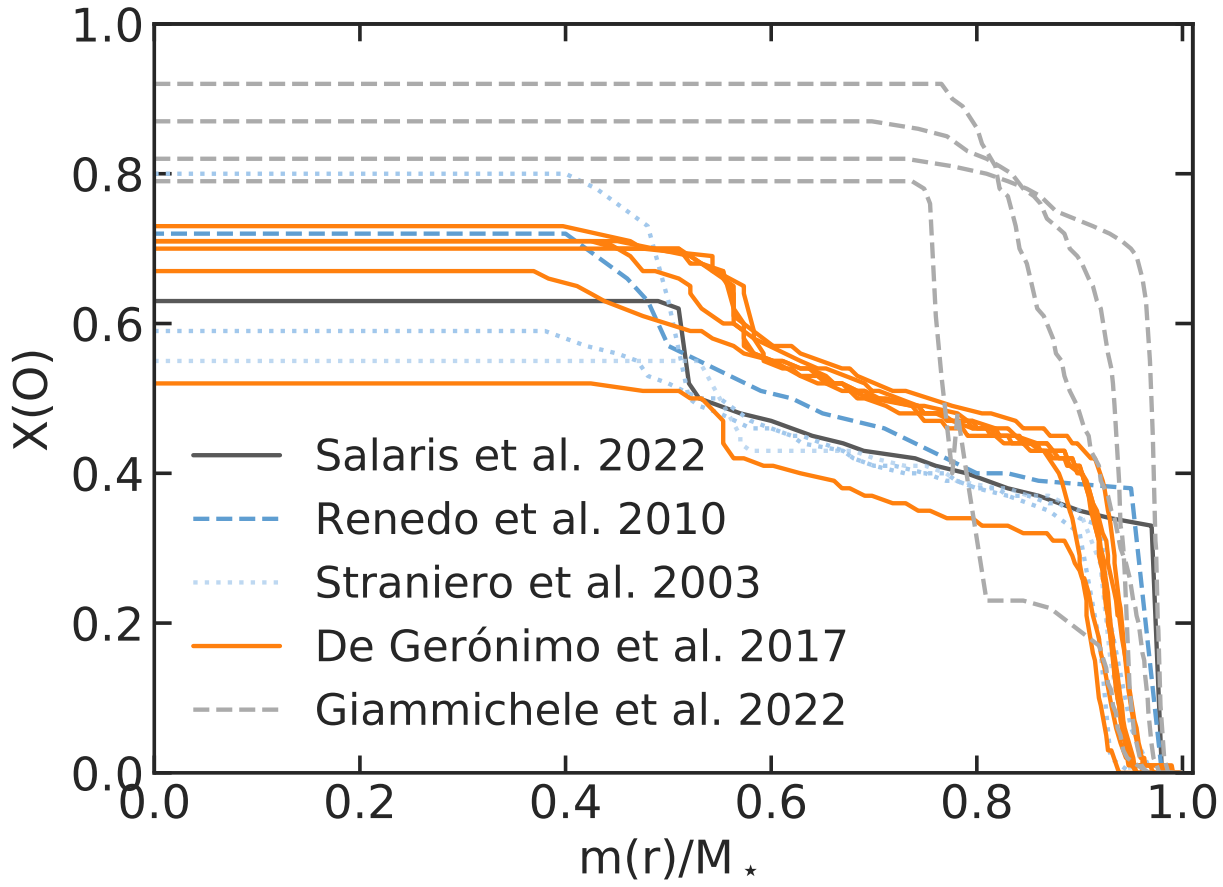

Figure 2.2: Oxygen mass fraction profiles for $\simeq 0.6\,M_{\odot}$ white dwarfs derived from evolutionary models and asteroseismological observations. These profiles defined the parameter range investigated in this work.

The final range of values for the 11-parameters are shown in the table 2.1.

For building the initial models of WDs with desired chemical composition profiles, we have used a MESA tool called `wd_builder`[1].

2.3.3 Other input physics

In MESA we have two options for conductive opacities, that is from Cassisi et al. (2007) and Blouin et al. (2020). Since it is still not clear which one is more appropriate for WD cooling, we have used both of them in our simulations.

We have also used the `atm_table = 'WD_tau_25'` option in MESA to include the opacity

[1]Developed by Josiah Schwab. It is now part of the MESA contrib repository (https://github.com/MESAHub/mesa-contrib).

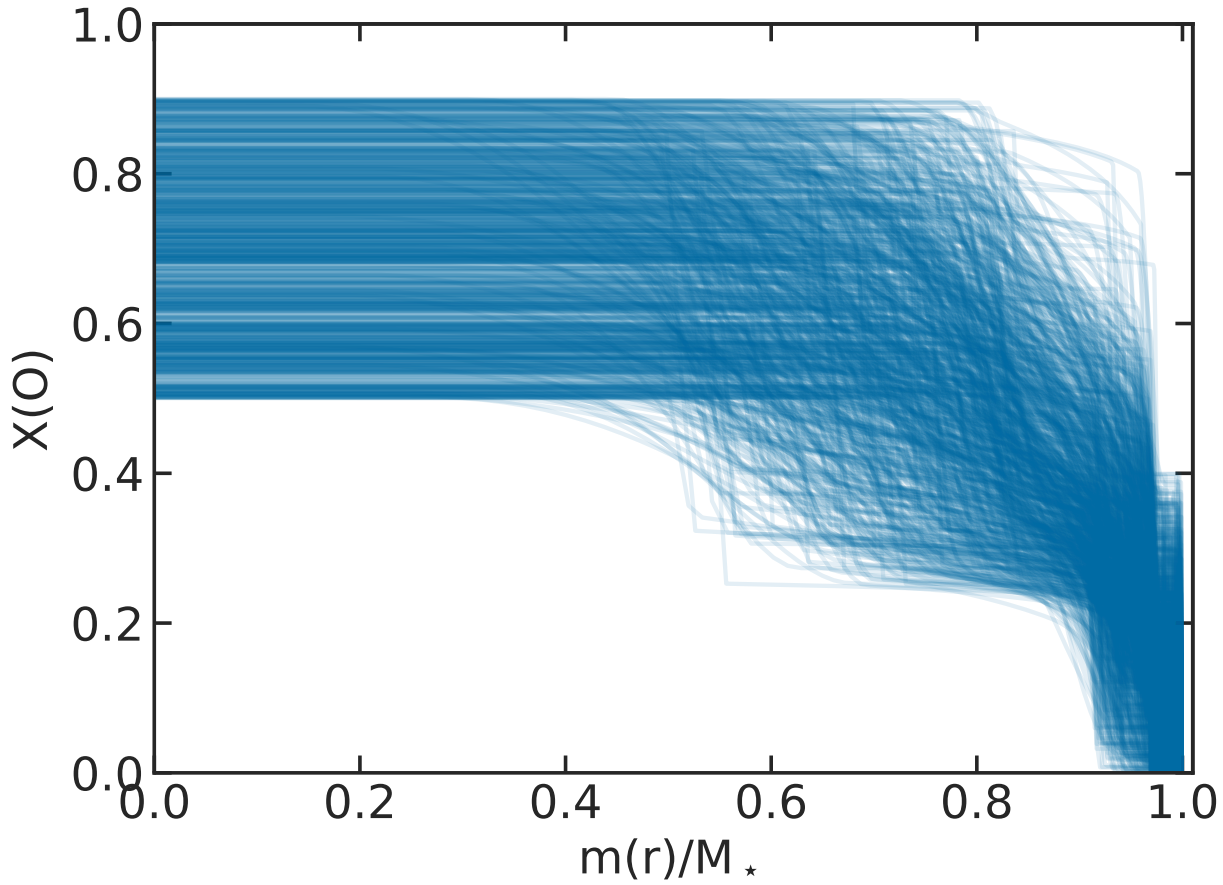

Figure 2.3: Oxygen abundance profiles derived from randomly sampling of the eight Akima spline parameter distributions defined in Table 2.1.

tables from Rohrmann et al. (2011) which is relevant to hydrogen atmosphere WD atmospheres.

Although ^{22}Ne diffusion is an important input physics for WD cooling, we have not included it in our simulations. As compared to cooling delays due to variations in the core ^{16}O composition, the cooling delays due to ^{22}Ne diffusion are much smaller (Bauer, 2023).

2.4 Results and Discussion

In this paper we have estimated the uncertainty in the cooling time scales of WDs coming from uncertain chemical composition and conductive opacities. For WD mass from 0.5 to 1.0 $M_{\odot}$, we have used the core composition motivated from asteroseismology Giammichele et al. (2017) as well as pre-WD evolution models.

Figure 2.1 shows the 11-parameter profile of the WD used in this analysis. All the ^{16}O

Table 2.1: Range of parameter values used in the study. See Giammichele et al. (2017) and Section 2.3 for details on these parameters.

Parameter	**Distribution**	**WD Mass ($M_\odot$)**					
		0.5	0.6	0.7	0.8	0.9	1.0
`core_o`	uniform	0.5 - 0.9	Same for all WD masses				
`t1`	uniform	0.30 - 0.80					
`dt1`	uniform	0.00 - 0.25					
`t1_o`	uniform	0.25 - 0.75					
`t2`	uniform	1.05 - 1.60					
`dt2`	uniform	0.00 - 0.25					
`t2_o`	uniform	0.20 - 0.70					
`envl_o`	uniform	0.00 - 0.40					
`X_Ne`	lognormal	0.00279 - 0.0279					
`-logqHe`	uniform	1.5 - 3.0	1.5 - 3.0	5 - 5	1.8 - 3.0	2.1 - 3.0	2.35 - 3.0
`-logqH`	uniform	4.0 - 6.0	4.0 - 6.0	5 - 5	4.3 - 6.0	4.75 - 6.0	4.75 - 6.0

profiles that we have used for the fitting are monotonically decreasing from the core to the surface and we have also restricted the 8-parameters to have this property. This is done so that core-O profiles are consistent from the profiles obtained from standard stellar evolution calculations.

Figure 2.4 demonstrates the model-based cooling age uncertainty that arises from the uncertain input physics in the WD evolution models for 0.6 $M_\odot$ case. The solid black line represents the mean cooling track of all the 1000 grey cooling tracks while the dot-dashed black lines represent the 1 σ spread around the mean, which is the cooling age uncertainty.

Figure 2.5 (Left) shows the age uncertainty (in Gyrs) as a function of effective temperature (in K) for different WD masses. Here the age uncertainty is defined as the standard deviation (σ) of the cooling age distribution at a given effective temperature of all the 1000 profiles for a given WD mass. Almost all the cooling ages uncertainties are within 3 σ. Going from 0.5 to 0.8 $M_\odot$, we see that the age uncertainty increases with increasing WD mass. However this behaviour is not seen after 0.8 $M_\odot$ where the age uncertainty starts to decrease slightly. The plot also shows points where 10 % and 90 % of the WD core is crystallized shown by blue and red stars respectively. Although for a particular WD mass these crystallization points will not be exactly at the same effective temperature, here we calculate these points by taking the middle value of the distribution intervals of all the parameters to get a rough idea of the crystallization points for a given WD mass. As expected, due to their higher densities, higher mass WDs crystallize earlier since the Coulomb coupling parameter (Γ) reaches the

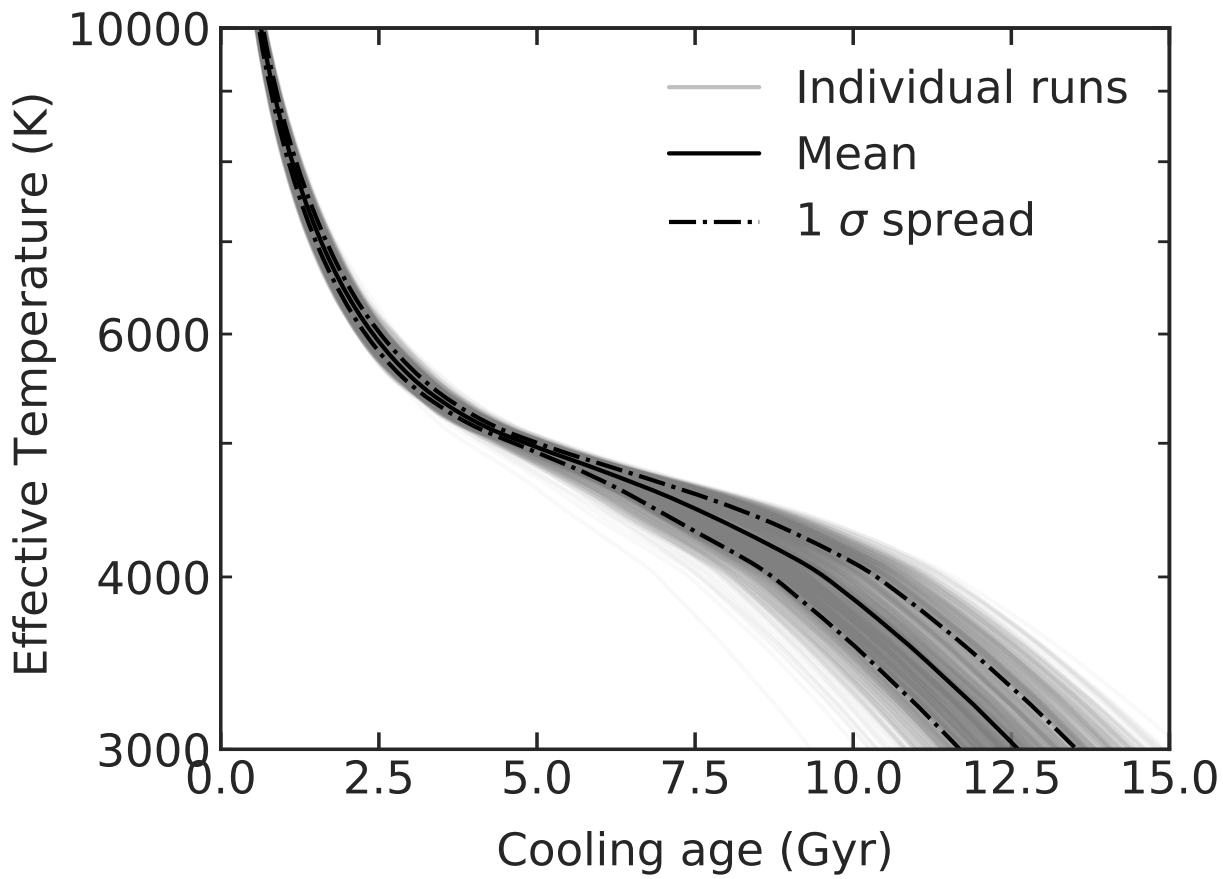

Figure 2.4: Cooling tracks for a $0.6 M_{\odot}$ white dwarf with varying parameters (grey), the mean cooling track (black solid line), and the 1 σ spread around the mean (black dot-dashed line), as discussed in Section 2.3.

critical value sooner. Also we see that even after 90 % of the core is crystallized, the age uncertainty still increases as the WD cools.

To understand this trend in more detail, we have plotted the relative age uncertainty as a function of effective temperature in the Figure 2.5 (Right). Here the relative age uncertainty is defined as the age uncertainty divided by the cooling age. Therefore it is a measure of the fractional uncertainty in the cooling age. We see an interesting trend for all the WD masses at high ($> 20,000\,K$), intermediate ($6,000\,K - 20,000\,K$) and low ($3,000\,K - 6,000\,K$) effective temperatures.

Figure 2.5 show the smoothed curves (orange dashed curve) for the cooling age uncertainty and relative age uncertainty derived from the sample of WDs within 40 pc of the Sun (O'Brien et al., 2024). We have also filtered the data to include only stars with Atmospheric Composition (comp) as `H`, i.e., hydrogen atmosphere WDs.

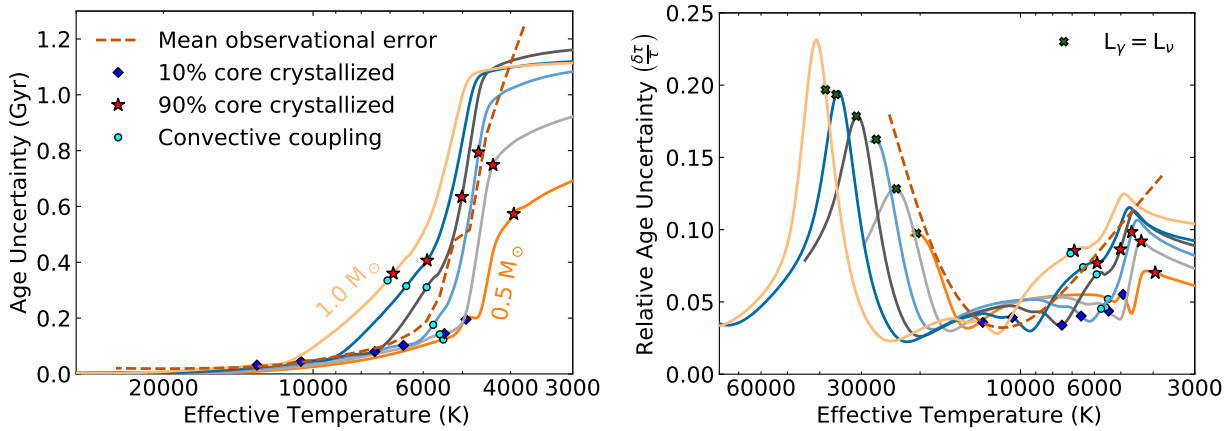

Figure 2.5: (*Left*): Age uncertainty (Gyr) as a function of effective temperature (K) for various white dwarf masses. The leftmost curve corresponds to $1M_\odot$, while the rightmost curve represents $0.5M_\odot$. Moving from left to right, the mass decreases from $1M_\odot$ to $0.5M_\odot$ in steps of $0.1M_\odot$. Blue diamonds indicate the points where 10% of the core crystallizes, red stars mark 90% core crystallization, and neon circles denote the onset of convective coupling with the envelope. The orange dashed line represents the average age uncertainty based on error propagation of $T_{\rm eff}$ and mass measurements (O'Brien et al., 2024). (Right): relative age uncertainty as a function of effective temperature. The green cross markers indicate points where photon luminosity (L_γ) equals neutrino luminosity (L_ν) for various white dwarf masses. Other line and marker legends are consistent with those in left figure.

The figures show that the model-based cooling age uncertainty is quite significant when compared with the reported observational uncertainties (see blue dot-dashed line). Also, as the WD core crystallizes from 10 % to 90 %, the age uncertainty as well as the relative age uncertainty increases. This is because the core crystallization mechanism and hence the cooling age of WD is very sensitive to the core composition (Blouin and Daligault, 2021). The figure also reveals that even after 90 % of the core is crystallized, the age uncertainty still increases as the WD cools, which is reflected in the Figure 2.5 (Right). This behaviour is due to the convective coupling, an efficient heat transfer mechanism between the degenerate core and the surface convective layers formed above as discussed in Blouin et al. (2020). The onset of convective coupling is sensitive to the surface composition which is uncertain and hence causes the low-$T_{\rm eff}$ relative age uncertainty bump in Figure 2.5 (Right).

We also see that there is a high $T_{\rm eff}$ ($T_{\rm eff} > 20{,}000$ K) bump in the relative age uncertainty plot in Figure 2.5. This is again related to two different opacity tables and neutrino cooling, an important cooling mechanism in the high $T_{\rm eff}$ regime, which is discussed in Blouin et al. (2020). A decrease in conductive opacities leads to faster initial core cooling which results in a lower core temperature, reducing the efficiency of neutrino cooling. Consequently, the

Table 2.2: Relative systematic cooling age uncertainty (%) as a function of mass and effective temperature for hydrogen-atmosphere white dwarfs with carbon–oxygen cores

$T_{\rm eff}$ (K)	0.5 $M_\odot$	0.6 $M_\odot$	0.7 $M_\odot$	0.8 $M_\odot$	0.9 $M_\odot$	1.0 $M_\odot$
20000	9.7	8.0	3.9	2.6	2.5	3.1
17500	7.1	3.6	3.2	3.1	3.2	3.7
15000	3.4	3.3	4.1	3.9	3.8	3.7
12500	4.0	4.4	4.8	4.5	4.1	3.2
10000	5.1	5.1	5.1	4.6	3.4	5.1 (+38.2)
9000	5.3	5.2	5.2	4.3	3.3 (+9.4)	6.5 (+52.0)
8000	5.4	5.3	4.8	3.7	5.2 (+33.4)	7.5 (+40.4)
7000	5.5	5.2	4.6	4.3	6.8 (+34.6)	8.4 (+31.0)
6000	5.5	4.9	3.9	6.8 (+20.3)	7.7 (+24.5)	9.0 (+22.8)
5500	5.2	4.5	5.0 (+10.6)	7.0 (+22.5)	8.3 (+19.5)	10.2 (+18.7)
5000	5.6	3.8 (+9.1)	6.9 (+19.8)	8.7 (+17.0)	10.4 (+15.1)	12.3 (+15.8)
4500	5.2 (+12.8)	8.5 (+16.7)	10.6 (+14.5)	11.2 (+13.7)	11.1 (+12.5)	11.8 (+13.9)
4000	7.0 (+16.4)	8.6 (+12.9)	9.6 (+11.9)	10.1 (+11.7)	10.1 (+11.2)	11.1 (+12.9)
3500	6.6 (+13.5)	7.9 (+11.1)	8.8 (+10.6)	9.4 (+10.6)	9.6 (+10.5)	10.7 (+12.4)
3000	6.1 (+11.5)	7.3 (+9.8)	8.2 (+9.6)	8.9 (+9.9)	9.2 (+10.0)	10.4 (+12.0)

Values without parentheses denote the fundamental systematic uncertainty arising from compositional and conductive opacity variations. Values in parentheses denote the potential additional relative age enhancement from ^{22}Ne shell distillation processes.

cooling time for a given effective temperature increases.

The ^{22}Ne distillation process, discussed in Section 2.2 exclusively increases cooling timescales (Renedo et al., 2010; Bédard et al., 2020; Salaris et al., 2022), precluding symmetric uncertainties. We therefore report distillation effects as potential age shifts (Table 2.2).

For a 0.8 $M_\odot$ white dwarf at 20,000 K, where crystallization has not begun, we report 2.6% systematic uncertainty. Below 6000 K, two values appear: baseline systematic uncertainty and potential distillation delay (parentheses). The delay amplitude increases sharply with decreasing $T_{\rm eff}$, reflecting the narrow temperature range where shell distillation occurs, then decreases relatively as total cooling age grows.

For example, a 0.8 $M_\odot$ white dwarf at 5000 K has 8.7% baseline uncertainty but 15.6% potential age increase from distillation. We recommend including baseline uncertainties in quadrature with observational errors and considering distillation delays when applicable. As understanding of ^{22}Ne distillation evolves, these additional uncertainties may be refined or eliminated.

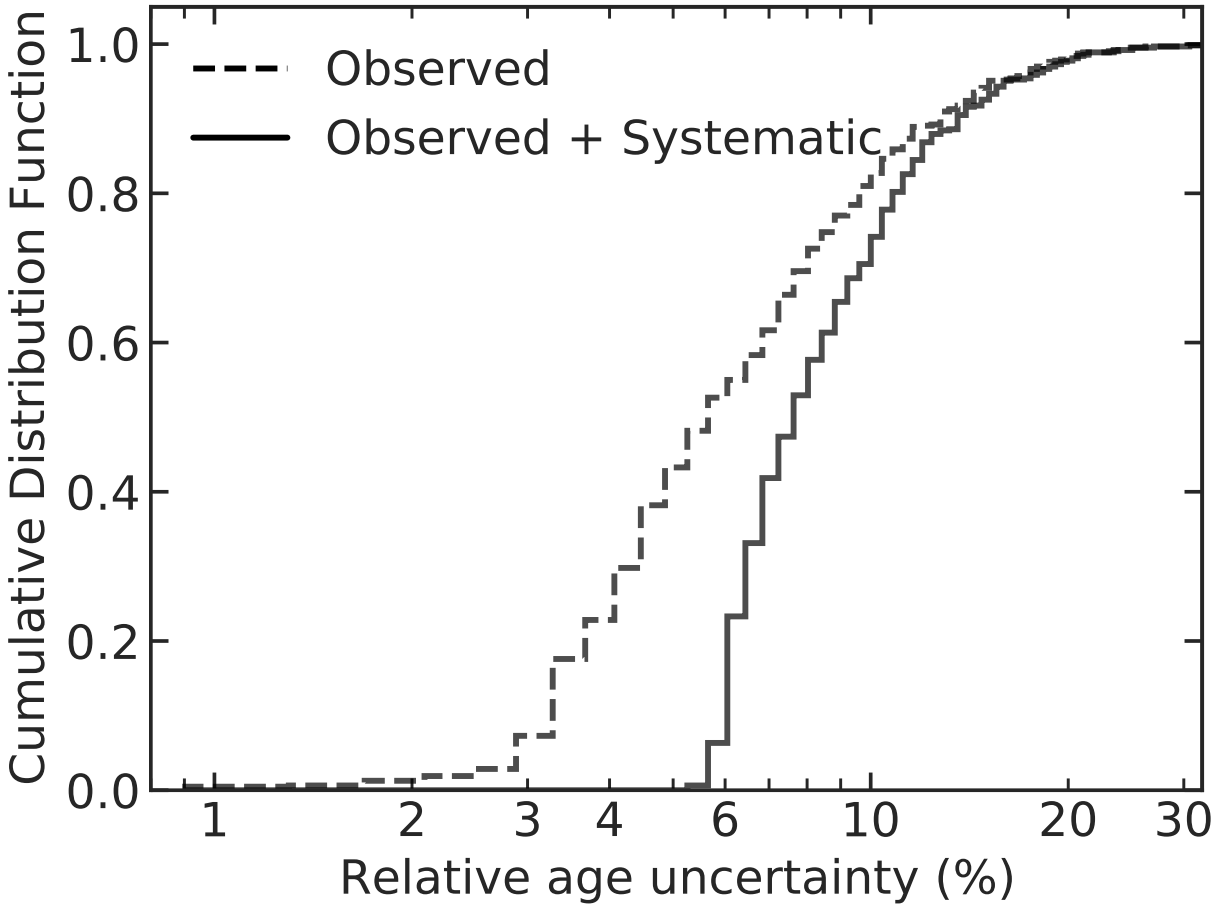

Figure 2.6: Cumulative Distribution Function comparing relative age uncertainty (%) calculated with `wdwarfdate` directly from observations (dashed line) versus incorporating systematic uncertainties (solid line).

2.5 Conclusion

In this study, we have estimated systematic cooling age uncertainties of hydrogen atmosphere WDs. We systematically varied core-O composition, envelope H and He thickness and conductive opacities of WDs to calculated the systematic model-based age uncertainty. The parameter space of was informed with stellar evolution models along with asteroseismic inferred chemical profiles. Additionally, we also provide systematic cooling delays due to ^{22}Ne distillation process. We provide a table of relative age uncertainty at $T_{\rm eff}$ for different WD masses in Table 2.2, which could be instrumental in estimating systematic errors in DA WD age dating. Our results suggests that most uncertainty in the cooling age comes from the uncertain conductive opacity tables (physics of cooling) along with the uncertain surface

composition (`qH` and `qHe`) and the potential occurrence of ^{22}Ne distillation.

This work does not address uncertainties in atmospheric model physics used to determine white dwarf effective temperatures and masses. Such uncertainties can be substantial, exemplified by the well-documented "low-mass problem" in white dwarfs below 6000 K, where atmospheric models produce anomalously low masses (Caron et al., 2023; O'Brien et al., 2024). This affects ∼45% of white dwarfs. Consequently, combining our systematic cooling uncertainties with observational errors likely underestimates the total uncertainty in white dwarf age determinations.

Our results can be incorporated in the age uncertainty assessment of the python package `wdwarfdate` (Kiman et al., 2022) used to derive the *Bayesian* age of a white dwarf, based on its effective temperature ($T_{\rm eff}$) and surface gravity ($\log g$).

Chapter 3

3D hydrodynamic simulations of massive main-sequence stars - IV. Internal gravity waves matter for SLF variability.

The contents of this chapter are based on a paper that has been submitted to *arXiv* (https://arxiv.org/abs/2508.03893) . The contributors to this paper are myself (P.P.), Dr. Simon Blouin (S.B.), Dr. Falk Herwig (F.H.), and Dr. Paul R. Woodward (P.R.W.). A detailed breakdown of their contributions is described below.

Conceptualization: F.H. conceived the original idea for this paper. **Methodology:** S.B. implemented the modification to the `MESA` opacity model. F.H. created the M424 run setup for `PPMstar`. P.R.W. helped in code modifications to the `PPMstar` code. **Software:** P.P. conducted all runs after M424. P.P. performed all data analysis utilizing Python tools developed by present and past members of the Computational Stellar Astrophysics (CSA) group and developed new Python notebooks for the analysis. **Validation:** S.B., F.H., and P.R.W. provided feedback on the results and their interpretation throughout the project. **Formal analysis:** P.P. conducted the formal analysis of the simulation results under the guidance of S.B., F.H., and P.R.W. **Investigation:** P.P. conducted simulations after the primary run M424 and analyzed the results. **Writing (original draft):** P.P. wrote the paper with feedback from S.B., F.H., and P.R.W., which forms the basis of this thesis chapter. **Supervision:** S.B., F.H., and P.R.W. provided supervision and guidance throughout the project development and analysis phases.

3.1 Abstract

The power spectrum of light curves from satellites like CoRoT and TESS of massive main-sequence stars have shown stochastic low-frequency (SLF) variability or excess power in the low frequency regime. To investigate the origin of this phenomenon, we conducted high-resolution 3D hydrodynamic `PPMstar` simulations of a non-rotating $25M_{\odot}$ zero-age main sequence star, modeling 95% of the stellar structure with both core and subsurface convection zones. The subsurface convection zone was implemented through modification of the opacity model, shifting the Fe opacity bump inward and enhancing its amplitude to ensure computational feasibility. The luminosity power spectrum from our primary simulation (M424) exhibits qualitative and quantitative characteristics similar to observed SLF variability, with a two-order-of-magnitude difference between high and low frequencies matching observational data. The spectrum displays distinct features attributable to internal gravity waves (IGWs) evanescent in the subsurface convection zone, originating from the subsurface convective boundary. To isolate the contributions of different stellar regions, we performed controlled numerical experiments with suppressed core convection and subsurface-only configurations. The comparative analysis demonstrates that subsurface convection alone produces significantly less power at low frequencies than the full star configuration. Our results indicate that IGWs excited at the subsurface convection inner boundary and interacting with the subsurface convection are the dominant contributors to SLF variability in our simulations.

3.2 Introduction

Stochastic low-frequency (SLF) variability, characterized by excess power at lower frequencies in the power spectrum of observed light curves, is a ubiquitous phenomenon detected in the luminosity power spectra of O and B type stars (Blomme et al., 2011; Bowman et al., 2019a,b). This variability is observed across diverse metallicity environments, indicating a common underlying physical mechanism (Bowman et al., 2024). Understanding this mechanism is critically important, as internal gravity waves (IGWs) generated in the stellar interior and propagating to the surface represent a potential source of this phenomenon. Confirmation of this hypothesis may potentially facilitate inference of internal stellar structure parameters from external light curve observations, such as convective core mass, radii, internal rotation rate, and other structural properties (Aerts, 2021; Mombarg et al., 2024).

The implications of such findings extend to the constraint of internal stellar stratification parameters, including convective core size and composition, which would refine stellar evolution models and advance stellar physics (Aerts et al., 2010). This approach has previously

yielded significant results in solar-type stars, with investigations determining age and initial composition of 16 Cyg A and B (Metcalfe et al., 2012), He in their atmospheres (Verma et al., 2014), and depths of the surface convective layer and helium ionization zone through acoustic glitch analysis (Mazumdar et al., 2014).

The physical mechanism responsible for SLF variability is still unclear (for a review see Bowman, 2023). Multiple 2D and 3D simulations of massive stars have reproduced frequency spectra from mock luminosity observations with morphology similar to SLF variability (e.g. Rogers et al., 2013; Rogers, 2015; Aerts and Rogers, 2015; Rogers and McElwaine, 2017; Edelmann et al., 2019; Ratnasingam et al., 2019, 2020, 2023; Horst et al., 2020; Varghese et al., 2023; Vanon et al., 2023; Thompson et al., 2024). Among the proposed mechanisms, core convection has been suggested as a source of gravity waves that propagate to the surface, where temperature fluctuations from the superposition of these IGWs produce luminosity variations manifesting as SLF variability in luminosity time series (Aerts and Rogers, 2015).

However, Anders et al. (2023) conducted 3D simulations of massive star convection using a two-component approach: wave generation simulations that directly model core convection and wave excitation, combined with theoretical transfer functions to represent wave propagation through the stellar envelope to the surface. Their wave propagation simulations extended to 93% of the stellar radius with mode lifetimes of $\lesssim 10$ years. Using this methodology, they concluded that gravity waves excited by turbulent core convection do not reach the stellar surface with observable amplitudes due to radiative damping (Lecoanet et al., 2019, 2021; Le Saux et al., 2023).

Some investigations propose that if SLF variability does not originate from gravity waves excited by core convection, it may instead result from turbulence induced by subsurface convection due to the Fe opacity bump near the surface (Cantiello et al., 2009, 2021; Schultz et al., 2022, 2023). Nevertheless, Jermyn et al. (2022) found that main-sequence stars (8-20 $M_\odot$) at SMC-like metallicities lack substantial subsurface convection zones because their Rayleigh numbers fall below the critical value required for convection onset, despite being predicted as convectively unstable by 1D stellar evolution models, yet these stars exhibit SLF variability comparable to stars with such convection zones (Bowman et al., 2024).

Stochastic light variations from wind instability constitute another potential mechanism for SLF variability in massive stars (Krtička and Feldmeier, 2018, 2021). This mechanism, however, is expected to have minimal impact for late O-type and early B-type main-sequence stars due to their optically thin and weak winds, particularly at low metallicity.

In our series of papers on massive main sequence stars, Thompson et al. (2024) conducted 3D hydrodynamic simulations of a 25 $M_\odot$ mid-main-sequence star extending from

the stellar center to approximately 54% of the stellar radius. These simulations, performed without radiative effects, reproduced qualitatively similar spectra to observed SLF variability, demonstrating that core convection can stochastically excite IGWs that produce photometric variability. However, the characteristic frequency obtained ($\nu_{\rm char} \approx 6\,\mu$Hz) was significantly smaller than typical observational values (Bowman et al., 2019a,b, 2020). Additionally, our synthetic observations were extracted from deep within the stellar interior, far from the observable photosphere, and the simulations did not account for subsurface convection zones that may contribute to surface variability. These limitations motivated the present study to investigate the combined effects of both core and subsurface convection in a more complete stellar model.

In this paper, we present high-resolution `PPMstar` simulations of a non-rotating 25 $M_\odot$ ZAMS (Zero Age Main Sequence) star to investigate the origin of low-frequency excess. In Section 3.3, we describe our base state and the modified opacity model employed in the simulations. In Section 3.4, we present power spectra from simulated light curves from different runs and analyze them comprehensively. Finally, in Section 3.5, we discuss our findings and present conclusions outlining directions for future research.

3.3 Methods

3.3.1 Base `MESA` state

This work employs the 3D hydrodynamics `PPMstar` explicit gas dynamics code, which incorporates an ideal gas plus radiation pressure equation of state with radiative diffusion in the energy flux (Colella and Woodward, 1984; Woodward et al., 2015; Herwig et al., 2023; Mao et al., 2024). Initial conditions[1] for the simulations are derived from a Zero Age Main Sequence (ZAMS) state constructed using Modules for Experiments in Stellar Astrophysics (`MESA`) revision 5329 (Paxton et al., 2011a). The base model comprises a non-rotating 25 $M_\odot$ star, with initial metallicity Z = 0.02 at the ZAMS stage. The stellar structure includes a convective core that extends beyond the Schwarzschild boundary through a penetration zone, implemented using a simplified version of the convective boundary prescription described in Mao et al. (2024). The implementation of this convective boundary treatment is evident in the temperature gradient profiles shown in Figure 3.1 (right panel), which demonstrate the smooth transition of $\nabla_{\rm T}$ from the convective core through the penetration zone to the radiative envelope. The Kippenhahn diagram in Figure 3.1 (left panel) marks the base state used in the simulations with the outer boundary $R_{\rm max}$ positioned at 4100

[1]Please refer to the MESA profile available in the Zenodo repository 10.5281/zenodo.15679630.

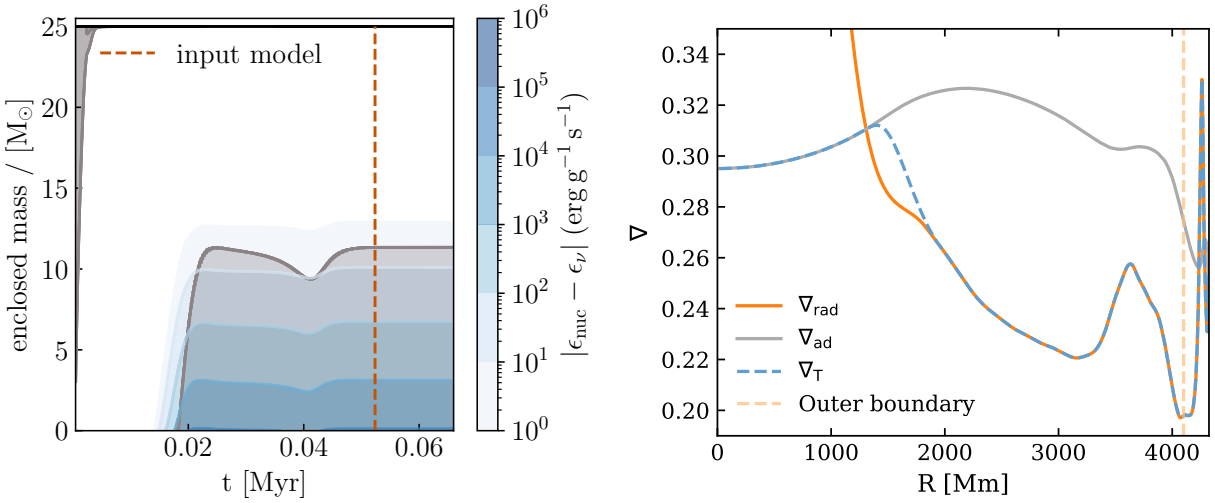

Figure 3.1: (*Left*): Kippenhahn diagram of the ZAMS 25 $M_\odot$ `MESA` model. Grey regions represent convective zones, white regions represent radiative zones, and blue contours indicate nuclear burning regions with intensities shown in the colorbar. The red dashed vertical line marks the initial model used for all the `PPMstar` simulations presented in this work. (*Right*): Radial profiles of the radiative (solid orange line), adiabatic (grey solid line), and actual temperature gradients (blue dashed line) for the ZAMS `MESA` model. The light orange dashed vertical line marks the outer boundary of the simulations presented in this work.

Mm, *encompassingahydrogen−burningconvectivecoreandintermediateradiativeenvelope.Weemploye*

3.3.2 Modified opacity model

Figure 3.2 compares the `MESA` opacity profile with the modified opacity model used in the simulations. The opacity remains unchanged throughout the short simulated time, and we use a fixed-in-time opacity profile. The opacity function $\kappa(r)$ for all runs is:

$$\kappa(r) = p_0 + p_1 \left(\frac{r}{1000\,\mathrm{Mm}}\right)^3 + p_2 \exp\left(-\frac{(r-p_3)^2}{2\,p_4^2}\right) \tag{3.1}$$

with parameter values $p_0 = 0.32587955$

cm^2/g, $p_1 = 0.00658106$

cm^2/g, $p_2 = 50.0$

cm^2/g, $p_3 = 4030$

Mm,$p_4 = 80$

Mm*and*r(Mm)*istheradialcoordinate.Threemodifications*w*eremadetotheopacitymodelascomparedto*M

Mm to 4030

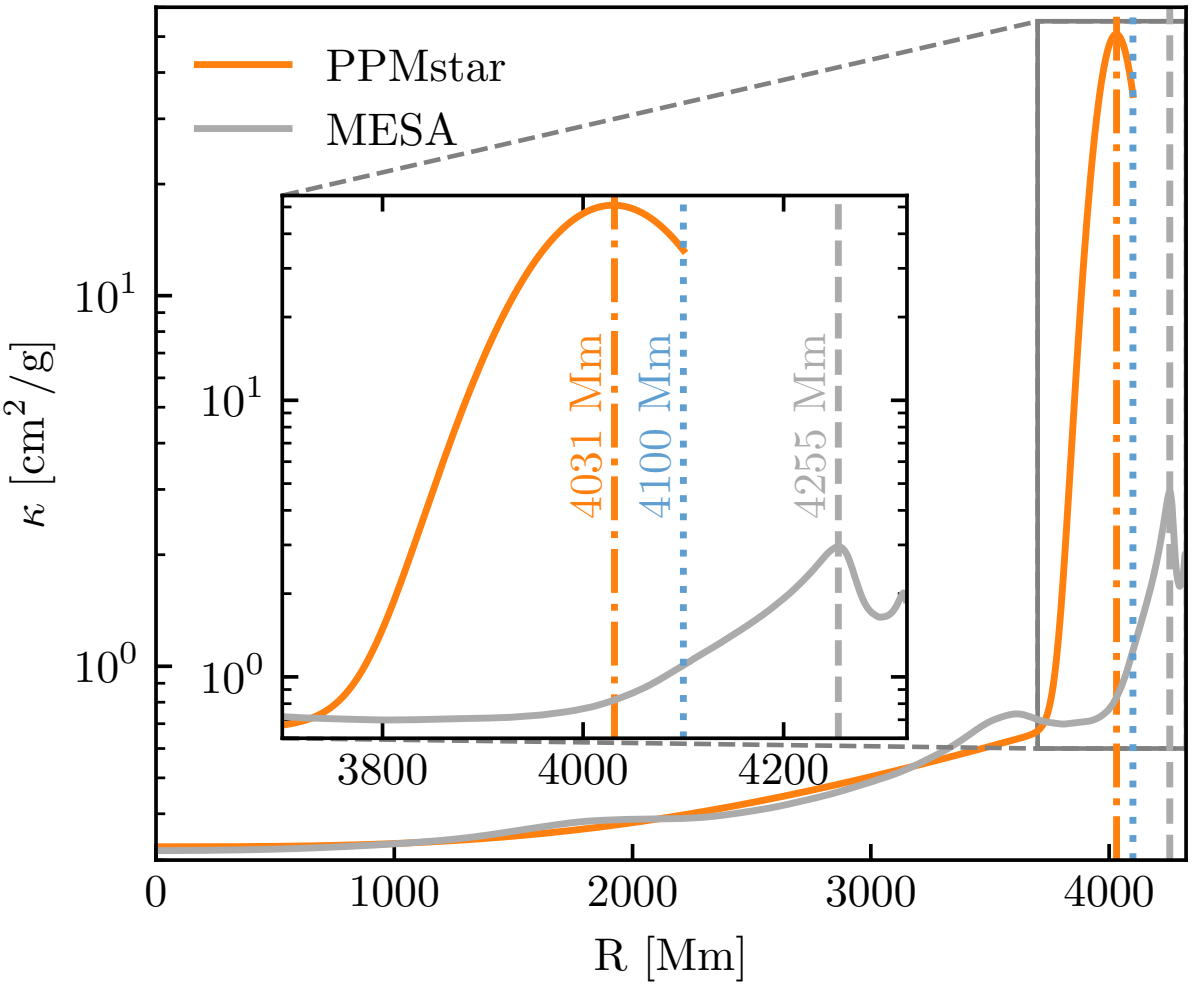

Figure 3.2: Comparison between the `MESA` opacity profile and the modified opacity model used in the `PPMstar` simulations. The grey dashed vertical line indicates the radial location of opacity bump maxima in the `MESA` profile, the orange dot-dashed line shows the radial location of the maxima in the modified opacity model, and the blue dotted line marks the outer boundary of the simulation domain.

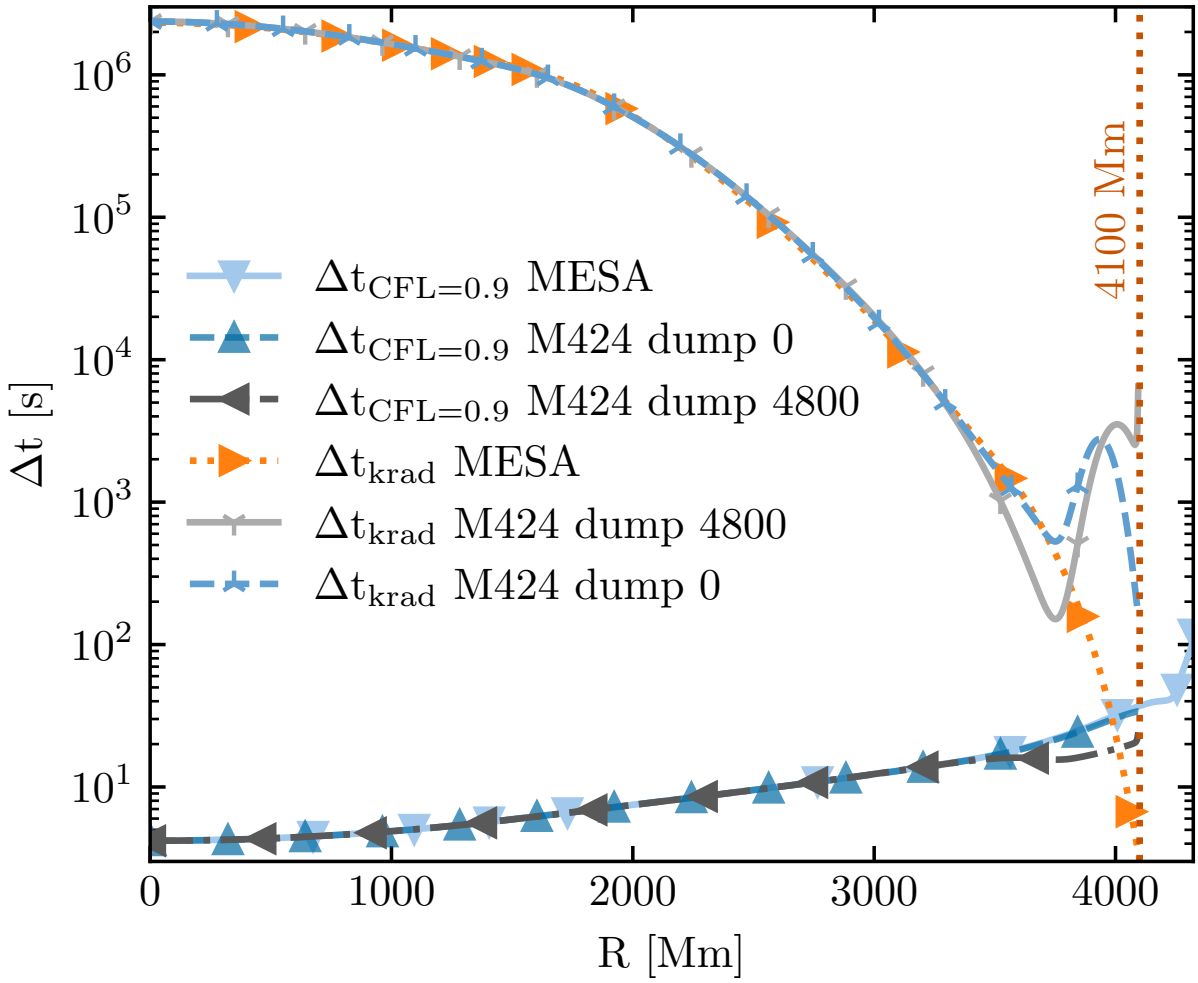

Figure 3.3: Comparison of CFL timestep (Courant et al., 1928) (with Courant number 0.9) with radiation diffusion timestep (Rider and Knoll, 1999) for the `MESA` model, dump 0 and dump 4800 ($\approx$ 3779 h) of run M424. The red dotted line marks the outer boundary of all the runs presented in this paper at 4100 Mm.

Mm*toplaceitwithinthecomputationaldomain.Thespreadofthisbumpwasincreasedtoexpandtheradiale*

We treat radiation in the diffusion limit. We adopt the radiative diffusion timestep $\Delta t_{\rm rad}$ from Rider and Knoll (1999):

$$\Delta t_{\rm rad} = \frac{\Delta x^2}{4\,\nu_{\rm rad}} \tag{3.2}$$

where $\nu_{\rm rad} = \frac{2}{3R}\frac{k_{\rm rad}}{\rho}$ and $k_{\rm rad} = \frac{4\,a\,c\,T^3}{3\,\kappa\,\rho}$. Here Δx is the grid spacing, R is the gas constant, ρ is the density, a is the radiation constant, c is the speed of light, T is the temperature, and κ is the opacity. Near the envelope, $\Delta t_{\rm rad}$ for `MESA` becomes comparable to and even smaller than the CFL timestep limit (Courant et al., 1928), as shown in Figure 3.3. We require $\Delta t_{\rm rad} > \Delta t_{\rm CFL}$ to take sufficiently large timesteps within the CFL limit for long duration simulations needed to perform time series analysis. The `MESA` densities drop rapidly in the outermost layers, and the timestep in those layers becomes prohibitively limited by the radiation timescale because we do explicit diffusion. Reducing the timestep to extend further outward is ineffective because the opacity drops steeply in the outermost layers. This requires us to choose $\rm R_{max}$ such that the radiation timestep constraint is satisfied with our CFL condition. Therefore we choose $\rm R_{max}$ in our simulations such that we can resolve the diffusion in the outermost layers with our modified opacity model. As shown in Figure 3.3, the radiative diffusion timestep limit in M424 remains above the CFL timestep limit (using Courant number 0.9). This characteristic applies to all runs as the same opacity model is used throughout.

Figure 3.4 shows eight orders of magnitude difference in pressure, four orders of magnitude difference in temperature, and six orders of magnitude difference in density between the `MESA` profile and dump 0. Although the outer convection zone is convectively unstable, radiation remains an efficient heat transfer mechanism there. Therefore, we observe that ∇ follows $\nabla_{\rm rad}$ around the opacity bump (Figure 3.1). The Brunt–Väisälä frequency remains positive in the outer convection zone because radiation effectively transports heat, maintaining stability against buoyancy perturbations despite the convective instability.

Table 3.1: Summary of simulation parameters

Run ID	Grid resolution	Core Heating enhancement factor	$\rm R_{min}$ (Mm)	$\rm R_{max}$ (Mm)	Cadence (mins)	Total simulation time (h)
M424	1792^3	100	0	4100	47	3779
M438	1728^3	0	0	4100	46	3947
M484	1792^3	100	3850	4100	44	2603
M487	1792^3	100	0	3600	41	3702

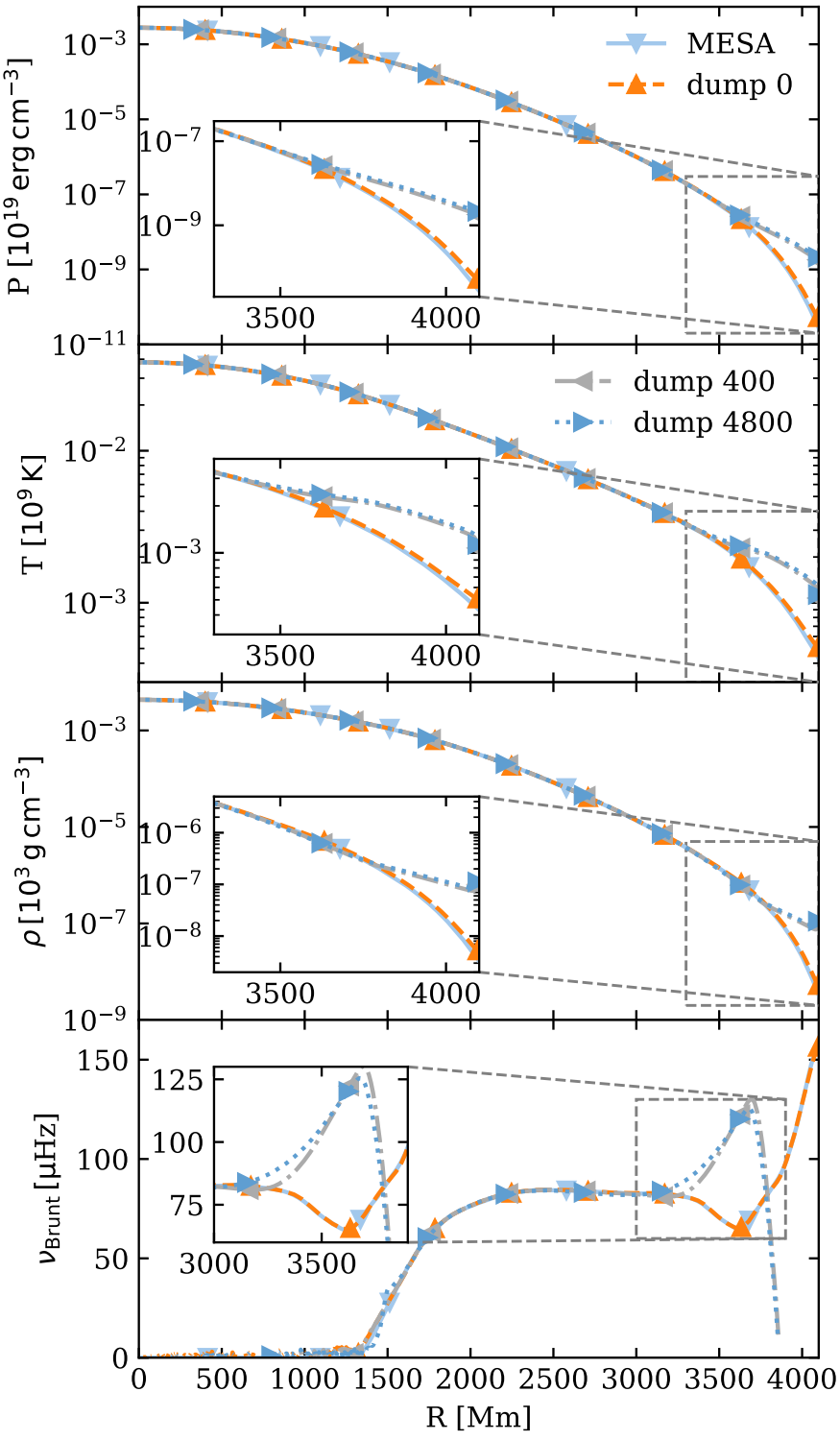

Figure 3.4: Comparison of pressure (P), temperature (T), density (ρ), and Brunt–Väisälä frequency (ν_{Brunt}) stratifications between the `MESA` state, dump 0, dump 100 and dump 4800 ($\approx$ 3779 h) of run M424. All panels share the same legend as shown in the top two panels.

The differences between dump 0 and dump 400 in Figure 3.4 demonstrate the fast initial thermal readjustment of the stellar structure in response to the modified opacity profile. The `PPMstar` simulation begins with the ZAMS `MESA` stratification but immediately starts evolving toward a new thermal equilibrium consistent with the enhanced and repositioned Fe opacity bump. This rapid thermal adjustment, occurring over approximately 310 h (much shorter than the stellar thermal timescale), reflects the star's response to the artificially modified opacity structure and results in the equilibrated stratification profiles shown at dump 400. Therefore, while our initial base state represents 95% of the stellar radius, the outermost 8% layers of the simulated star exhibit approximately ten times higher density than the MESA stellar model. This discrepancy results from the implementation of a convection zone in the outermost layer that is both thicker and positioned deeper than in the actual star. A stellar model with the convection zone present in our equilibrated hydrodynamic setup would likely have a larger stellar radius. The `MESA` ZAMS model has no mean molecular weight (μ) gradient except near the outer boundary due to partial ionization of chemical species as temperature decreases toward the surface. This effect is ignored in the initial setup of all runs, resulting in a flat $\mu = 0.617317$ mean molecular weight profile.

3.3.3 Luminosity post-processing and spectral analysis

`PPMstar` simulations save two different types of compressed data at equal intervals of time (dumps) which are substantially larger than the simulation time steps. These include `rprof`, which contains spherically averaged radial profiles at full grid resolution, and `briquette`, which stores 4x compressed 3D data as described in Stephens et al. (2021).

Temporal mock spectra are generated from the line-of-sight hemispherically averaged light curves at a given radius as described in Thompson et al. (2024). These mock light curves in eight different lines-of-sight are calculated in-line in the code at full grid resolution and output in the `rprof` files. These light curves are detrended with a 3^{rd}-order polynomial to remove the global trend, unity subtracted relative luminosity is computed, individual power spectra are calculated, and the results from all eight different lines of sight are averaged.

The power spectra are fitted with a Lorentzian function (Blomme et al., 2011; Bowman et al., 2019a,b):

$$\alpha(\nu) = \frac{\alpha_0}{1 + \left(\frac{\nu}{\nu_{\text{char}}}\right)^{\gamma}} + C_{\text{w}}, \tag{3.3}$$

where $\alpha(\nu)$ represents the Lorentzian curve in μHz, α_0 is the amplitude at zero frequency

(in μHz), ν and $\nu_{\rm char}$ are the frequency and characteristic frequency respectively (both in μHz), γ is the dimensionless logarithmic amplitude gradient, and $C_{\rm w}$ denotes the frequency independent noise (in μHz).

We use the 3D `briquette` data at a spherical shell of fixed radius R to construct the $\ell - \nu$ diagrams. Here ℓ is the spherical harmonic order and ν is the cyclic frequency. The $\ell - \nu$ diagrams are created for the calculated variable 'unity-subtracted relative luminosity' $\mathcal{L}$ (same as in Thompson et al., 2024), using the `briquette` temperature data (T) as:

$$\mathcal{L} = \frac{\mathrm{T}^4}{\langle \mathrm{T}^4 \rangle} - 1, \tag{3.4}$$

where $\langle \mathrm{T}^4 \rangle$ is the spherical average of 3D `briquette` temperature variable, at the radius of interest, which is used as a base to remove the global luminosity trend as a result of interaction of H-burning core and our artificial subsurface convection zone.

Table 3.1 summarizes all runs with their respective simulation parameters. These configurations enable systematic investigation of the individual and combined contributions of different stellar regions to the observed SLF variability. For the runs presented in this study, a modified opacity model is used as compared to the `MESA` opacity profile. Compared to the `MESA` model, core heating (mimicking core H burning) and thermal diffusivity are boosted by a factor of 100 to achieve numerically tractable fluid velocities and to scale down thermal diffusion timescales, respectively.

Several numerical constraints determine the choice of enhancement factor for core heating and thermal diffusivity. Minimizing the Mach number in the subsurface convection zone requires making thermal diffusivity large enough to reduce flow velocities, yet small enough to preserve convective instability necessary for convection to occur. We boost thermal diffusivity and luminosity by the same factor to maintain global thermal equilibrium and the stratification. Luminosity and radiation diffusion are boosted by the same factor to accelerate the stellar evolution simulation while preserving the underlying physics. This balanced enhancement speeds up both the thermal timescale ($\propto$ boost factor^{-1}) and convective timescale ($\propto$ boost factor$^{-1/3}$), making the ratio of thermal to dynamic timescale smaller with larger boost factors and thus computationally feasible to reach thermal and dynamic equilibrium (Mao et al., 2024). This optimization imposes the most restrictive constraint on the thermal diffusion timestep limit, necessitating the coordinated adjustment of both the boost factor and grid resolution. These competing numerical requirements lead to the 100$\times$ boost factor for core heating and thermal diffusivity enhancement. The combination of 1792^3 resolution with the 100$\times$ boost factor represents an optimal configuration that satisfies these

constraints. Previous convergence studies by Herwig et al. (2023), Thompson et al. (2024), and Mao et al. (2024) demonstrate that this resolution is high enough to achieve convergence for convective dynamics, entrainment rates, and envelope vorticity in 3D stellar convection simulations.

For each simulation, several core-convective turnover times are allowed to elapse before beginning analysis, ensuring fully developed convection in both the core (109 h turnover) and the envelope (3 h turnover).

3.4 Results

3.4.1 Simulation with core convection, radiative zone, and subsurface convection

Figure 3.5[2] shows the turbulent core and subsurface convection, separated by an intermediate radiative zone where wave-like features corresponding to internal gravity waves (IGWs) are evident. The turbulent convective core extends from the center to ≈ 1500

Mm, $exhibitinglarge-scaledipolecirculationpatternsvisibleintheradialvelocityandvarioussmall-scaleturbulentfeaturesapparentinthevorticitymagnitude.Thinring-likeIGWfeaturesarevisibleinthevo$
1500

Mmto3733

Mm. A strong subsurface convection zone appears as a thick ring around the outer boundary from ≈ 3733

Mmto4100

Mm, displaying high relative magnitudes in all three variables. A non-linear color mapping was employed to highlight these multi-scale features. The convective core morphology is discussed in detail in our previous papers (Herwig et al., 2023; Thompson et al., 2024; Mao et al., 2024).

The modified opacity model (Figure 3.2) implemented in our simulations produces strong turbulent subsurface convection with turnover timescale of ≈ 3 h. Figure 3.6 shows that we see a factor of ≈ 10 higher core convective velocities in M424 compared to `MESA` MLT velocities. Previous work by Herwig et al. (2023) shows that core convective velocities scale with luminosity boost factor as boost factor$^{1/3}$. This means at nominal luminosity, the core convective velocities are 4.64 times smaller but still 2-3 times larger than `MESA` MLT velocities. This is consistent with Jones et al. (2017) who found ≈ 2 factor higher velocities as

[2]Volume-rendered visualizations of various fluid variables for all simulations presented in this paper are available at https://www.ppmstar.org/.

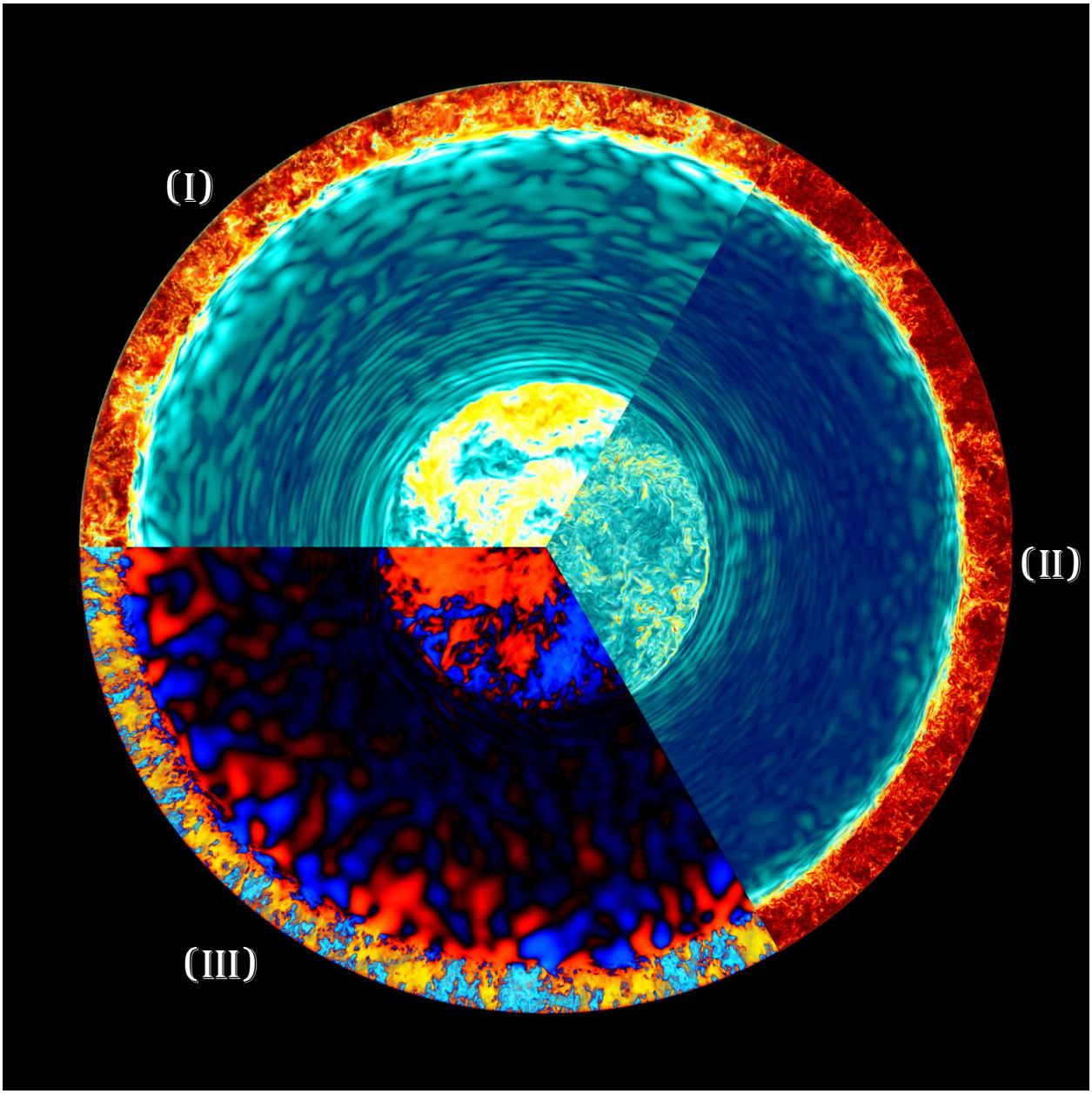

Figure 3.5: Volume-rendered visualization of three fluid variables for the run M424 at dump 2000 (1990 h), generated using a thin equatorial slice: (I) Horizontal velocity magnitude, represented by a color gradient from highest to lowest: dark brown, red, yellow, white, light blue, and dark blue; (II) Vorticity magnitude, depicted with a color scheme from highest to lowest: red, yellow, light blue, and dark blue; (III) Radial velocity, where inward-directed (negative) velocities are shown in light to dark blue (decreasing magnitude), and outward-directed (positive) velocities are shown in yellow, orange, and red (decreasing magnitude).

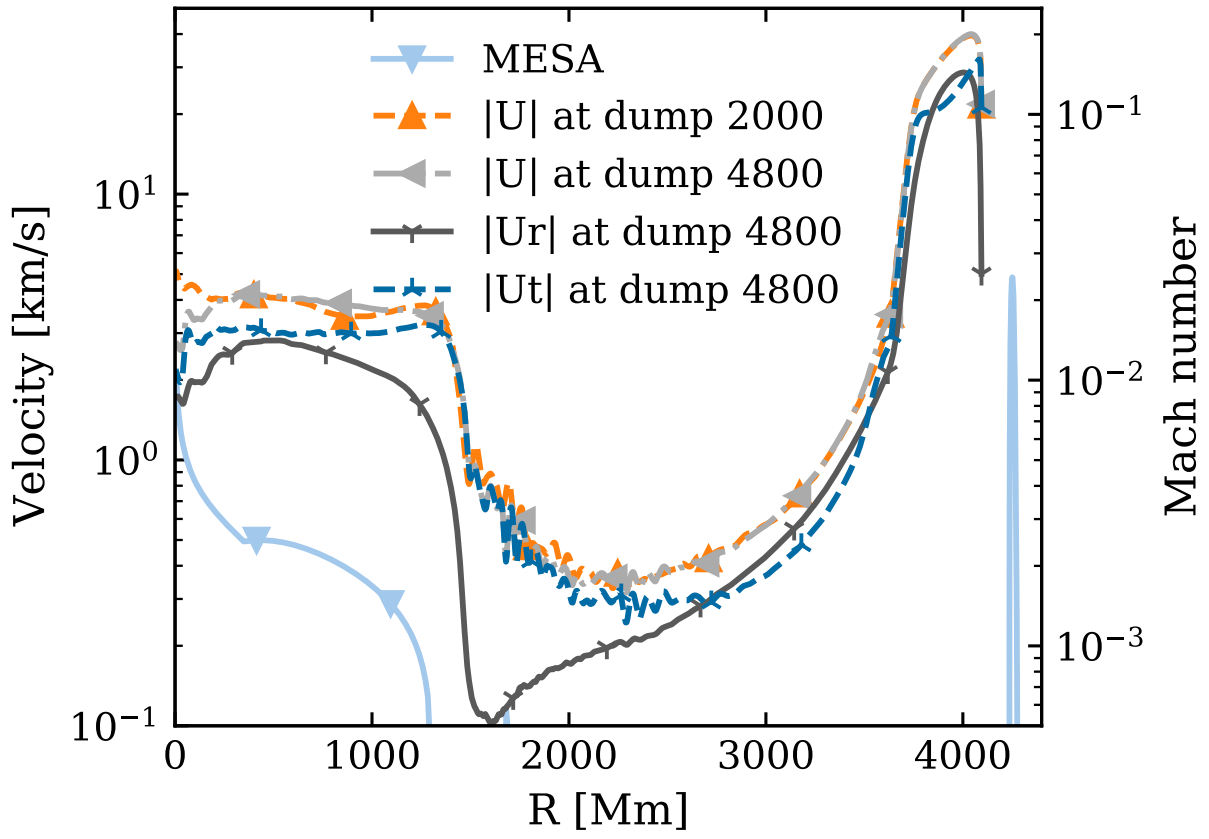

Figure 3.6: Comparison of `MESA` convective velocity profile with velocity magnitude $|U|$ for run M424 at dumps 2000 and 4800, and radial $|U_r|$ and tangential $|U_t|$ velocity magnitudes for M424 at dump 4800. The secondary y-axis shows the Mach number for the M424 profiles.

compared to MESA MLT velocity in their 3D PPMstar simulations of turbulent oxygen-burning shell convection at nominal luminosity. Figure 3.6 also shows that convective velocities in the subsurface zone are five to eight times larger than the subsurface convection in the MESA. Figure 3.7 confirms that the radial velocity U_r spatial power spectrum inside the subsurface convection zone follows the Kolmogorov's power law of $\ell^{-5/3}$, indicating that spatial scales at which most of the power is added to the turbulent convection are well separated and larger than the spatial scales at which energy is dissipated into heat. This figure also indicates that the dominant power is concentrated around the spatial scale of $\ell \approx 40$. This spatial scale corresponds to the radial extent of the subsurface convection zone.

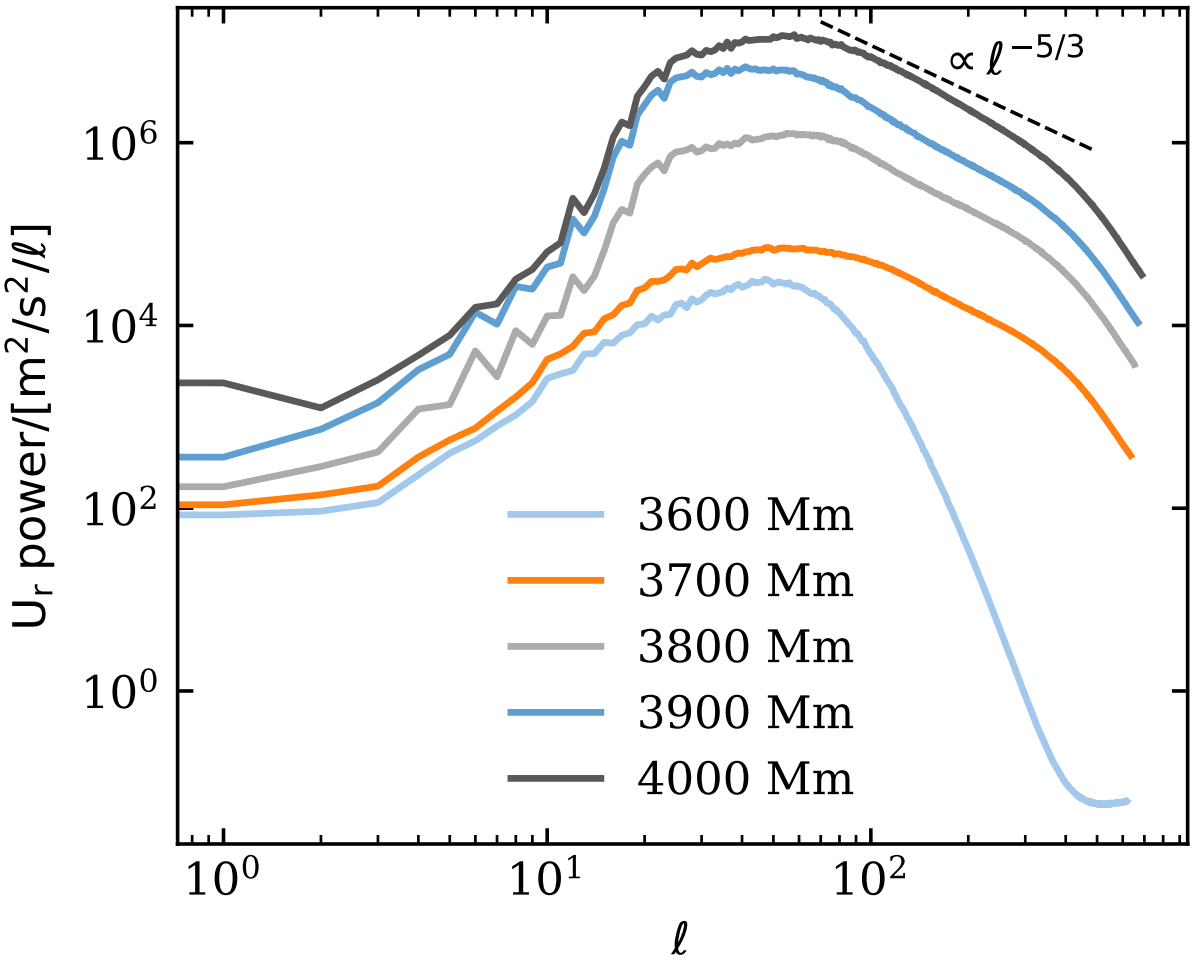

Figure 3.7: Radial velocity spatial spectra of the run M424 at different radial coordinates near the surface averaged over last 100 dumps.

The thermal diffusion timescale of the subsurface convection zone for run M424 is 308 h,

calculated using

$$\tau_{\rm th} = \frac{E_{\rm thermal}}{L}, \tag{3.5}$$

where L is the luminosity and $E_{\rm thermal}$ is the thermal energy computed using the virial theorem as $E_{\rm thermal} = -U_{\rm shell}/2$, where the gravitational potential energy of the shell is

$$U_{\rm shell} = -\int \frac{G\rho(r)M_{\rm enclosed}(r)}{r}\, dV, \tag{3.6}$$

where G is the gravitational constant, $\rho(r)$ is the density at radius r, $M_{\rm enclosed}(r)$ is the mass enclosed within radius r, and dV is the volume element. We assumed the radial extent of the subsurface convection zone from 3733

Mm($peak of Skew \times$ Kurtosis, see Appendix A.1) to the outer boundary 4100

Mm.$Thermal equilibrium gradually moves inward, initially fast, then slowing down as thermal timescale$

Mm to 2500

Mm$is \approx 10^6$ h. We ensure that the outer layers of interest are not changing significantly over the duration needed to create spectra (Figure 3.4). We determine the time interval required to make spectra and wait long enough so that the stratification remains stable over this analysis period. Therefore, we choose to analyze run M424 starting from dump 2000 (1990 h).

Figure 3.8 compares the luminosity power spectrum of run M424 near the surface (4000

Mm)$with observations of the O-star$ HD 46150[3] $using CoRoT (Convection, Rotation and planetary Transit$ $minute cadence, corresponding to a frequency range of 0.5 to 4.1 \times 10^3 \mu$Hz. The CoRoT light curves span the same duration but with variable cadence ranging from 0.5 to 20 minutes due to instrumental periodicities caused by the satellite's low-Earth orbit that create power artifacts in the spectrum. The mock M424 light curve spans 2800 dumps ($\approx$ 2193

h)$with 47-minute cadence, yielding a frequency range of 0.12 to 177 \mu$Hz. We therefore restrict the spectral plots in Figure 3.8 to the frequency range relevant to M424 for comparison. The earlier study of Thompson et al. (2024) showed qualitative similarities with observations but exhibited quantitative differences, such as $\nu_{\rm char} \approx 6$ μHz, which is an order of magnitude smaller than observations. After incorporating a larger radiative envelope and a (modified) subsurface convection zone in this study, the spectrum of run M424 demonstrates both qualitative and quantitative similarities with observations. All three panels display approximately a two-order-of-magnitude difference between power at 180 μHz and 1 μHz, with

[3] HD 46150 is a young main-sequence O dwarf (Bowman et al., 2019a) that is close to our ZAMS simulations.

ν_{char} values of the same order of magnitude as observed spectra. The difference in Lorentzian fit parameters between TESS and CoRoT observations exceeds the difference between the simulation and TESS observation, which is considered more reliable. The dynamic range of spectral features spans several orders of magnitude in both TESS and M424 spectra, although spectral troughs are deeper in the TESS spectrum.

Given that run M424 incorporates a convective core, an intermediate radiative zone, and a convective envelope, the question arises regarding the relative contribution of convection and IGWs generated at both the core and envelope convective boundaries to the observed spectra. Are the features, such as peaks and troughs, observed in the simulations related to eigenmodes?

3.4.2 Run without heating that drives core convection

Run M438 is identical to M424 but omits constant volume heating in the center that in M424 represents the core H burning. As in M424, the core in M438 is isentropic. This modification is evident in Figure 3.9(a), which shows the absence of turbulent core convection compared to Figure 3.5. This experiment was designed to investigate how eliminating core convection, and consequently the IGWs excited at the core-convective boundary, affects the frequency spectrum, particularly the low-frequency excess.

In Figure 3.10, we plot the luminosity power spectrum inside the subsurface convection zone at 4000Mm. For direct comparison between runs, we use the final 1600 dumps from each simulation, as not all runs have sufficient duration for longer time series (Table 3.1). With a cadence of $\approx$ 45 minutes, this yields frequency range from 0.2 to 185 μHz in the luminosity power spectrum. The luminosity power spectra reveal approximately equivalent power in the convective envelope when comparing M424 (with core convection) and M438 (without core convection) at 4000Mm. The integrated total power in M438 is 10% less than in M424. This means that the convective core and the IGWs originating at the convective core boundary contribute only a small (10%) effect to the low-frequency excess.

In Figure 3.10, several marked spectral features appear at identical frequencies in both M424 and M438, which cannot be attributed to convection due to its stochastic nature. The same features appear in the spectral analysis at 3500Mm for both runs in Figure 3.11. The location at 3500Mm is within the radiative zone below the subsurface convection boundary and beyond the convective overshoot region (Appendix A.1). Therefore at 3500Mm, the spectrum and its features must be due to IGWs. Since the same features appear at 4000Mm, they must originate from evanescent IGWs in the subsurface convection zone and

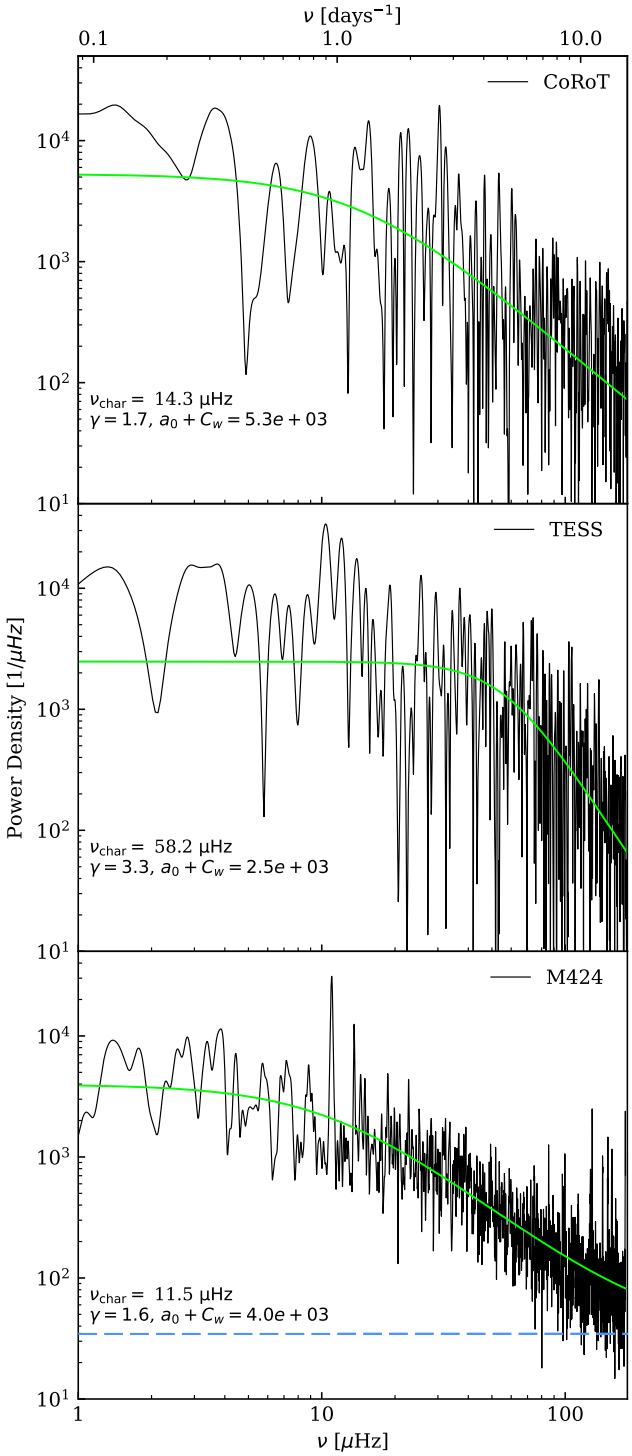

Figure 3.8: Comparison of luminosity power spectra between CoRoT and TESS observations of the O-star HD46150 and M424 simulation at 4000 Mm. The lime curve represents the best-fit semi-Lorentzian function, and the best-fit parameters are shown in the respective plots.

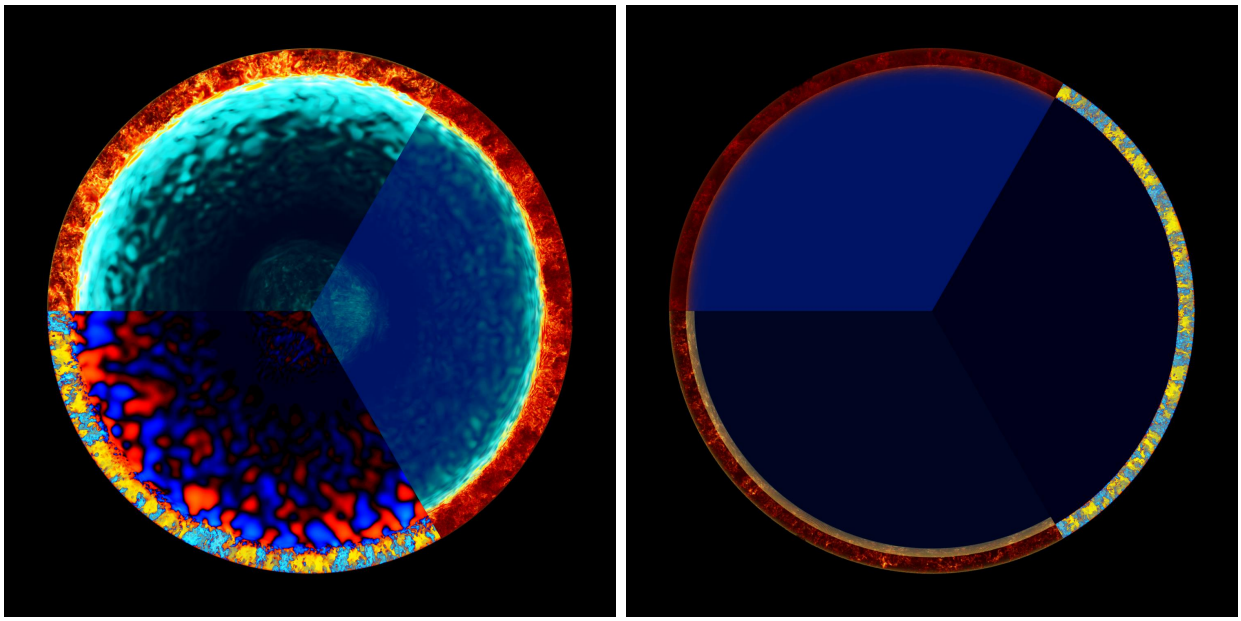

Figure 3.9: Volume rendered images similar to Figure 3.5 for subsequent runs listed in Table 3.1 after M424. (a) M438 (left) (b) M484 (right)

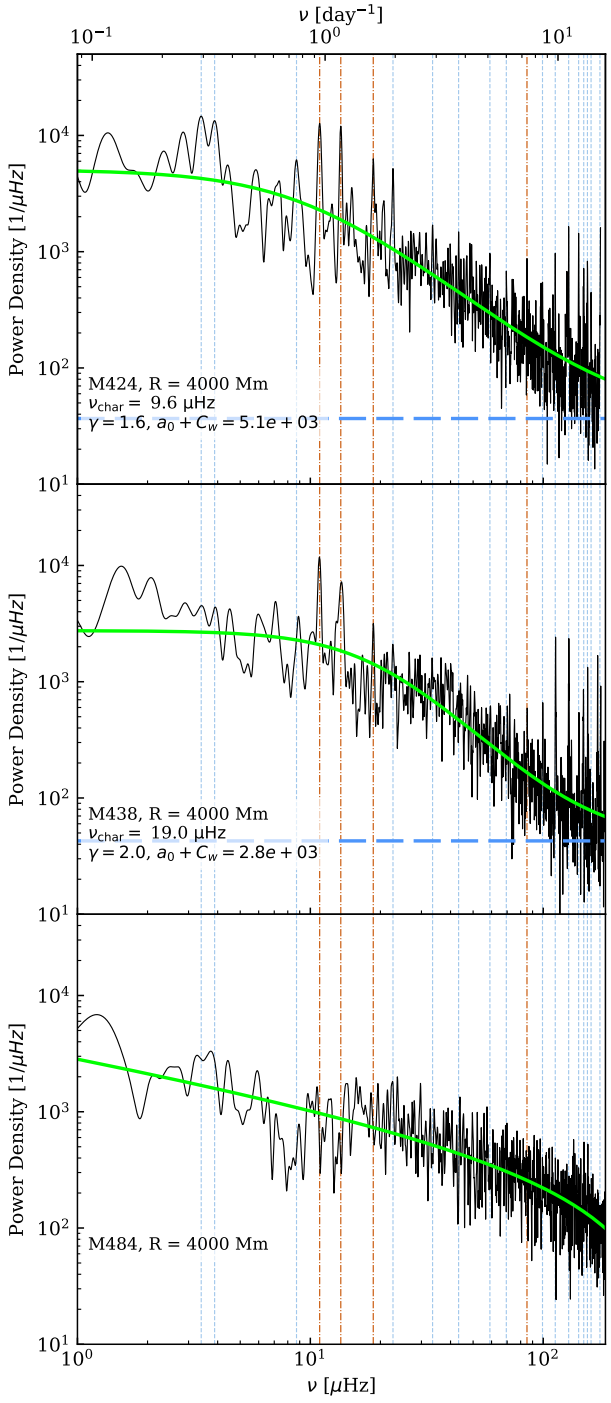

Figure 3.10: Comparison of luminosity power spectra at 4000 Mm across different simulation runs. Each spectrum was generated using the final 1600 dumps (≈ 1200h) of simulation data. We print the name of the run, the radius at which the spectrum was made and the best-fit Lorentzian parameters for respective panels with exception to last panel for M484 where we could not find a good Lorentzian fit. We plot several vertical dotted lines in all the subplots marking the sharp features present in M438 and M424.

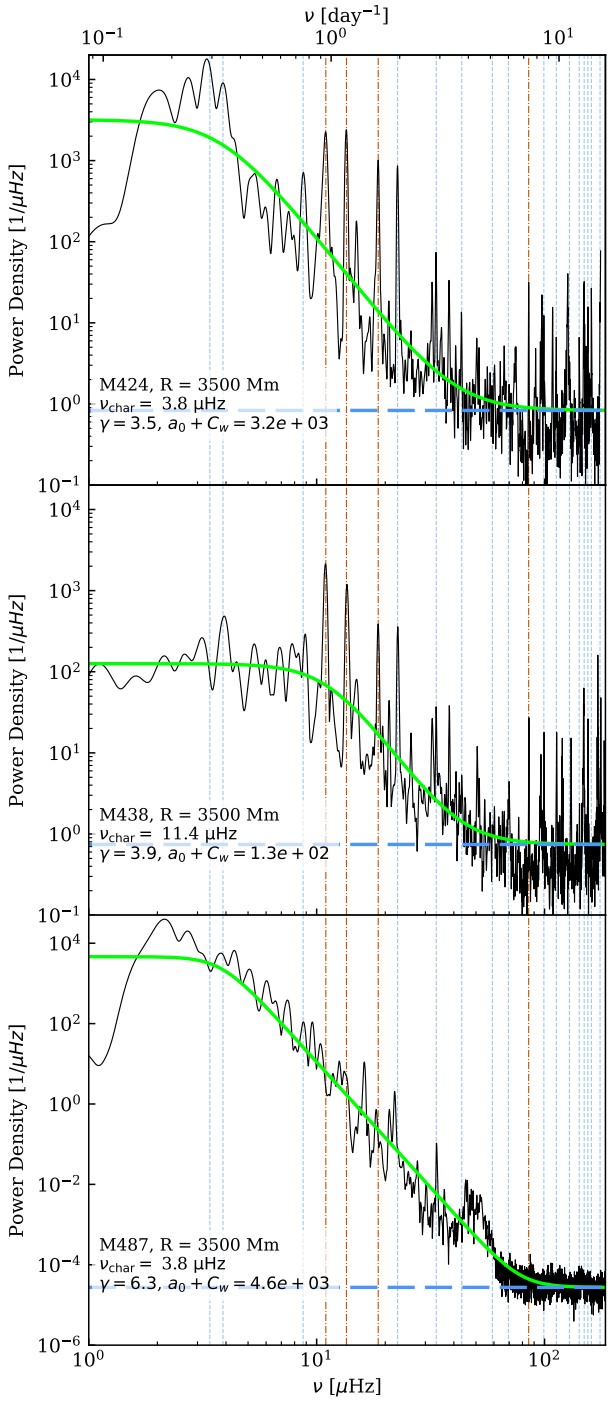

Figure 3.11: Same as Figure 3.10 but the luminosity power spectra made at 3500 Mm across different simulation runs. Same vertical dotted lines are plotted as in Figure 3.10.

the spectrum in these simulations is dominated by IGWs.

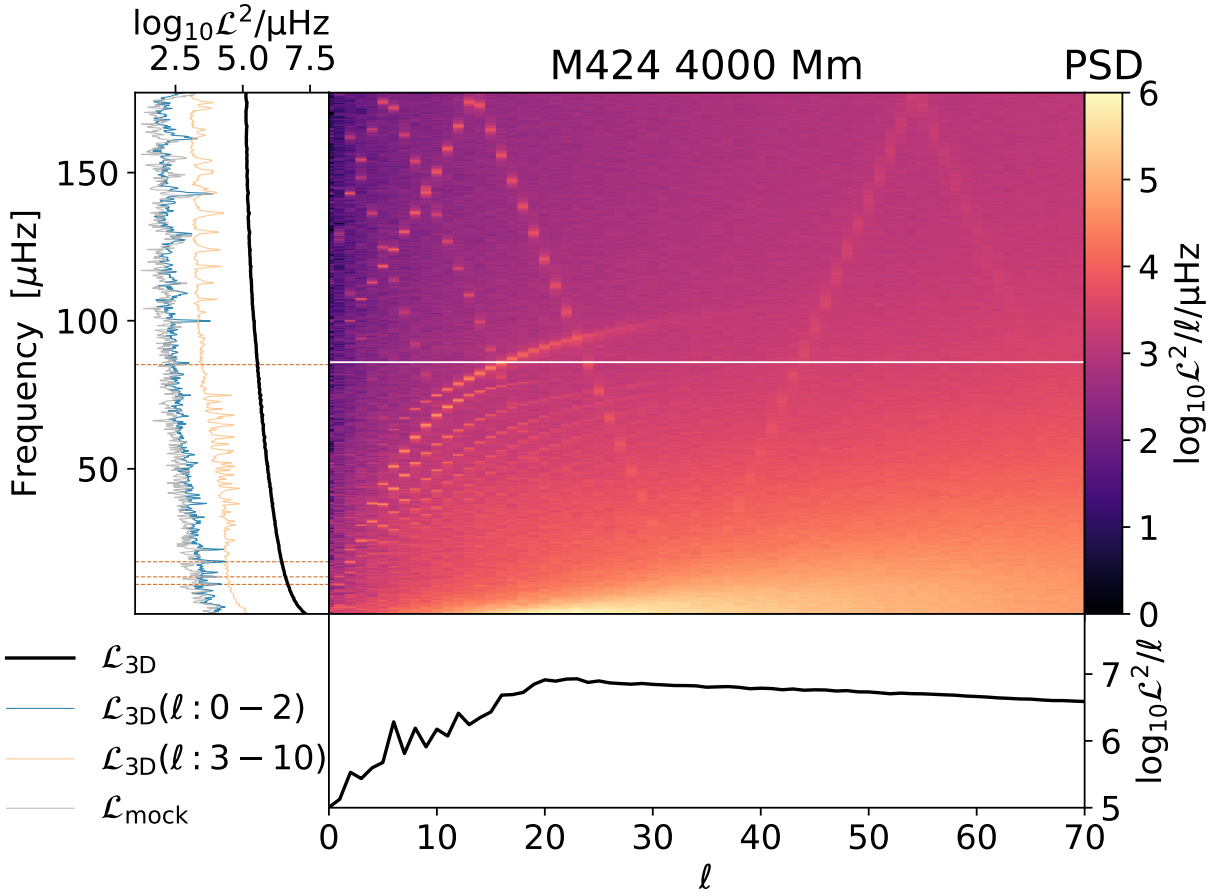

Figure 3.12: Power spectral density (PSD) as a function of spherical harmonic angular degree ℓ and cyclic frequency ν ($\ell - \nu$ diagram) for the variable $\mathcal{L}$ (unity subtracted relative luminosity) for the run M424 at 4000Mm. All $\ell - \nu$ diagrams utilize the final 1600 dumps. Horizontal solid lines marks the subsurface convective frequency. Plots along axes display summed power across each dimension (solid black, $\mathcal{L}_{3D}$). Vertical sub-plot includes power summed over $\ell = 0 - 2$ (blue) and $\ell = 3 - 10$ (orange). Grey curve ($\mathcal{L}_{\text{mock}}$) shows luminosity power spectra from Figure 3.10 and Figure 3.11 for respective runs.

The $\ell - \nu$ diagram of M424 in Figure 3.12 reveals convection spectrum at 4000Mm (left panel) along with evanescent IGW features. The same evanescent IGW features are present and prominent in the $\ell - \nu$ diagram of M424 at 3500Mm in Figure 3.15, within the radiative zone below the subsurface convective boundary, confirming that these features are indeed evanescent IGWs. Since the same evanescent IGW features are present in run M438 without core heating at 4000Mm and prominently at 3500Mm in the Figure 3.13 and 3.16, these evanescent IGWs are excited at the subsurface convection boundary. The $\mathcal{L}_{3D}$

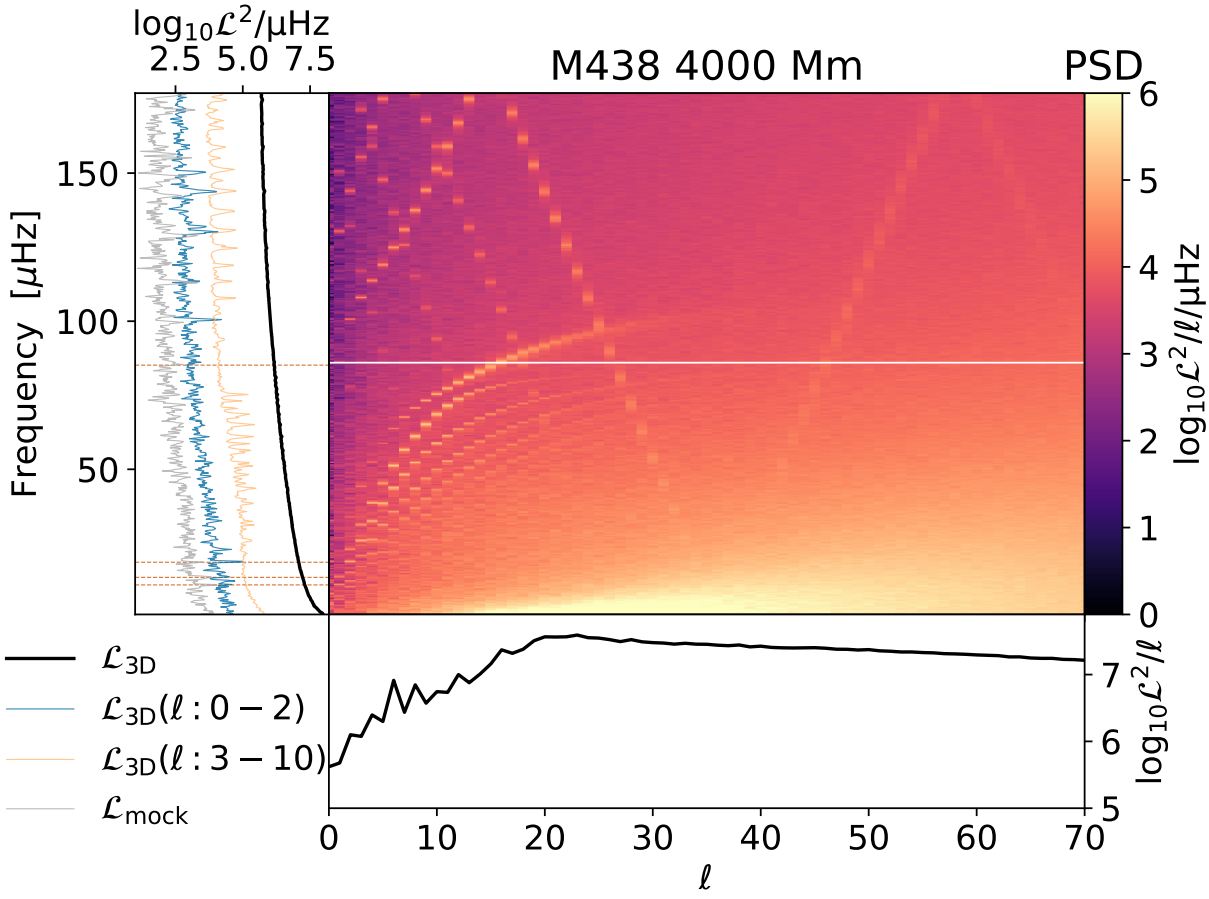

Figure 3.13: Same as Figure 3.12 but for the run M438 at 4000Mm.

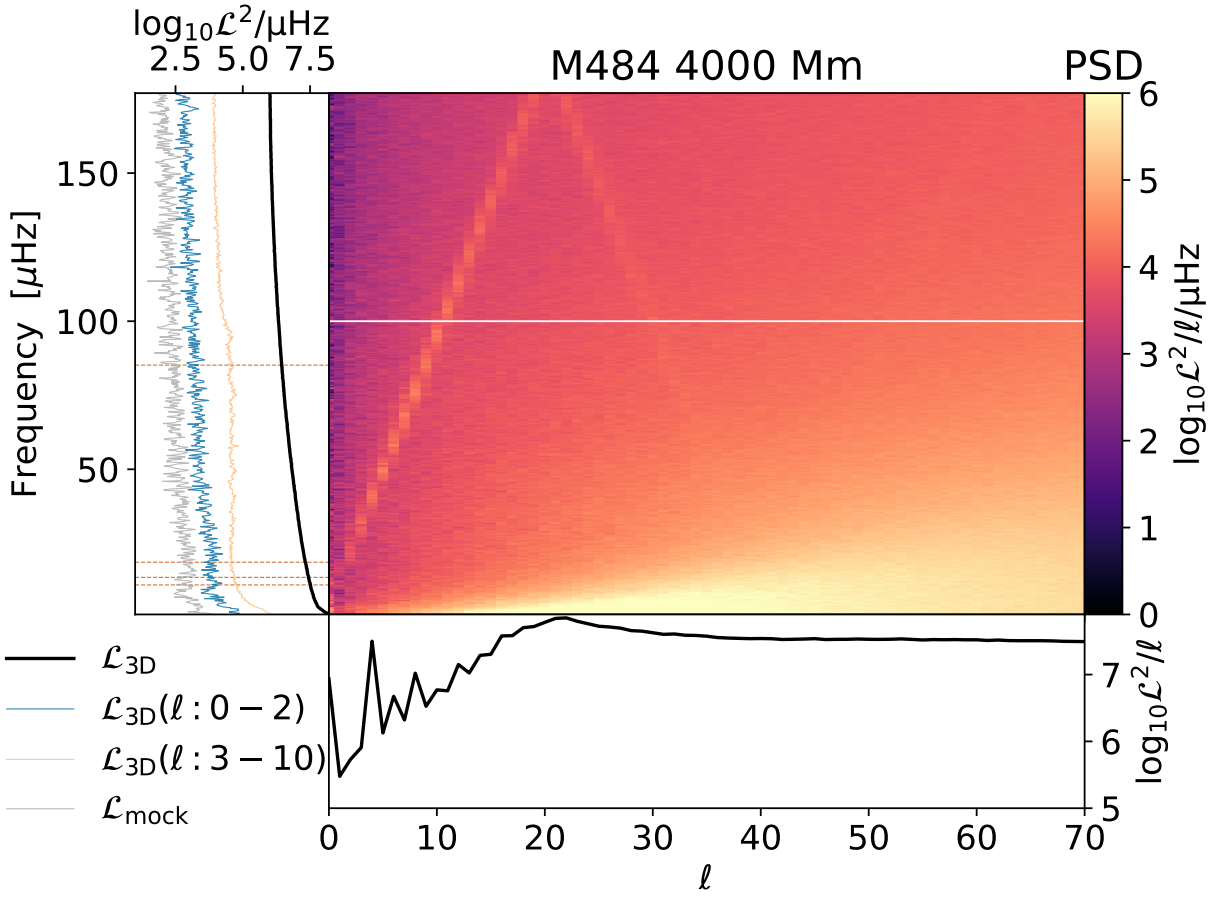

Figure 3.14: Same as Figure 3.12 but for the run M484 at 4000Mm.

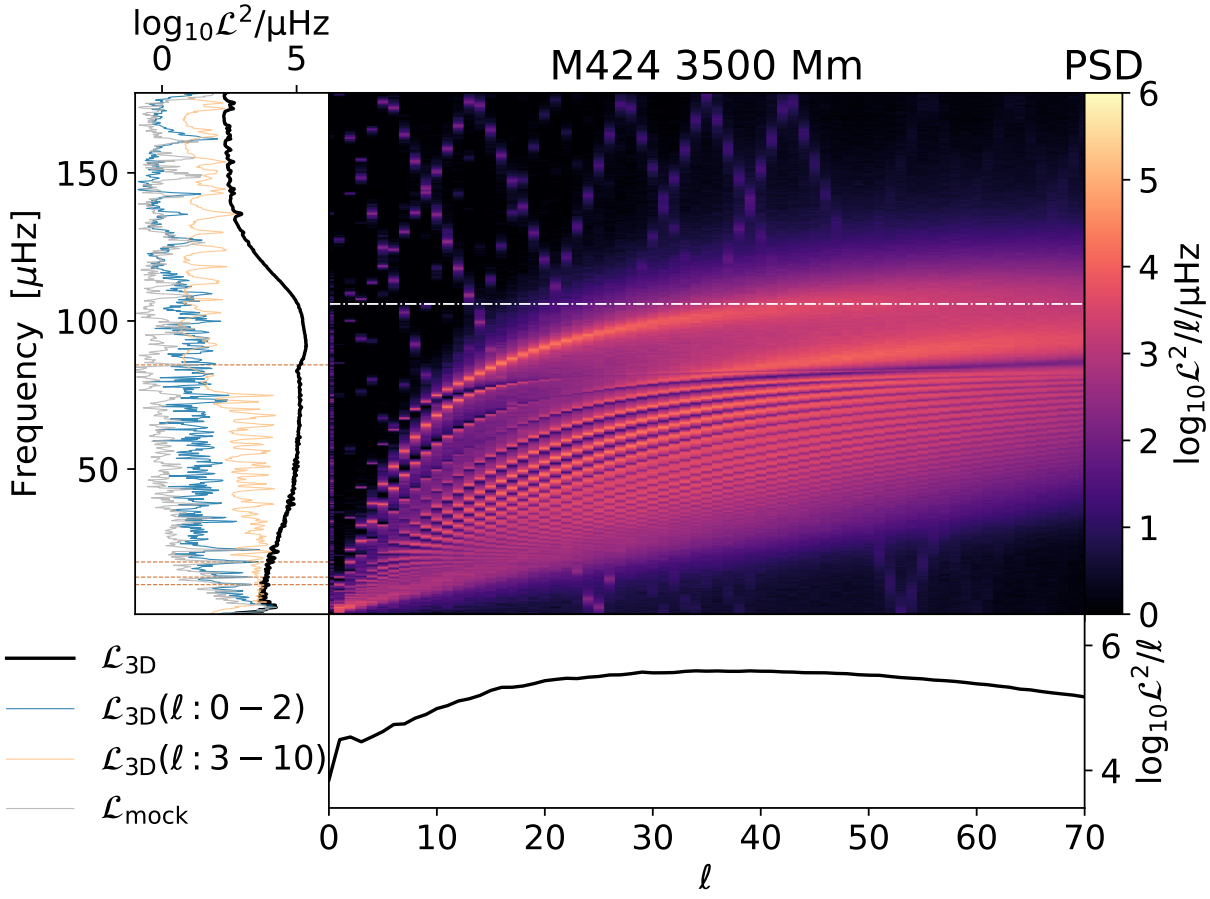

Figure 3.15: Same as Figure 3.12 but for the run M424 at 3500Mm. The horizontal dot-dashed line marks the linear Brunt–Väisälä frequency ν_{Brunt}.

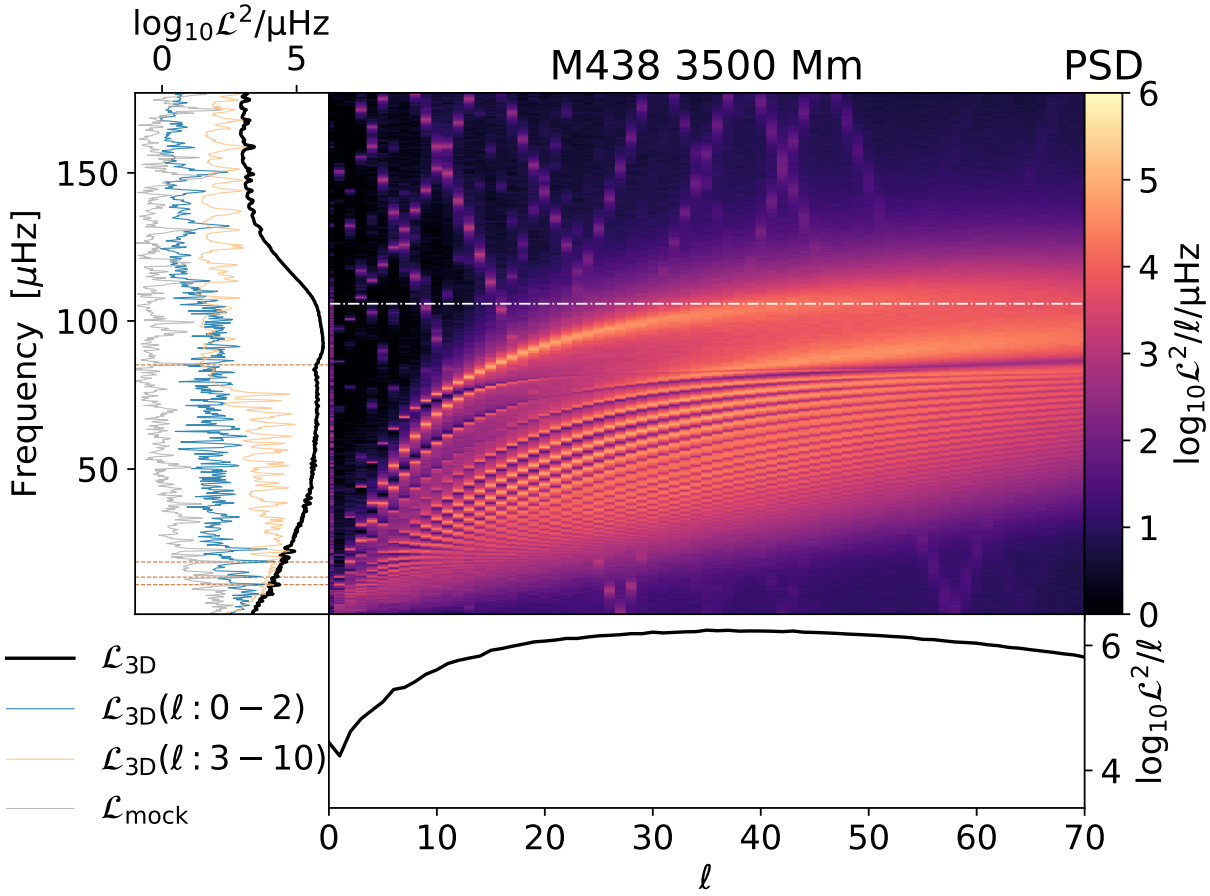

Figure 3.16: Same as Figure 3.12 but for the run M438 at 3500Mm. The horizontal dot-dashed line marks the linear Brunt–Väisälä frequency $\nu_{\rm Brunt}$.

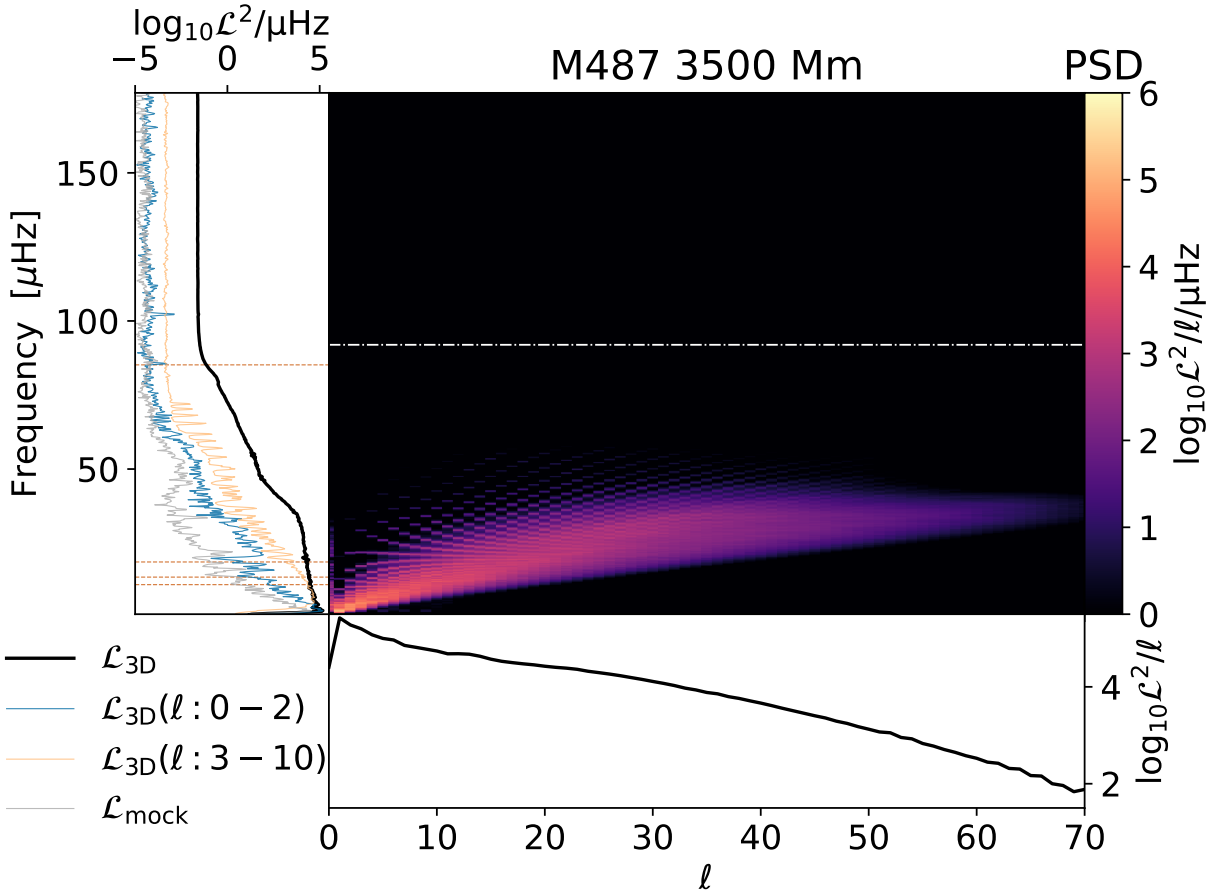

Figure 3.17: Same as Figure 3.12 but for the run M487 at 3500Mm. The horizontal dot-dashed line marks the linear Brunt–Väisälä frequency $\nu_{\rm Brunt}$.

is the power spectral density of 3D luminosity fluctuations around a sphere of fixed radius. $\mathcal{L}_{\rm mock}$ is the power spectral density of line of sight averaged mock luminosity observations obtained by hemispherically integrated 3D luminosity along a line-of-sight. The $\mathcal{L}_{\rm 3D}$ curve in these $\ell - \nu$ diagrams is a couple of orders of magnitude higher than the grey $\mathcal{L}_{\rm mock}$. This discrepancy comes from the hemispherical integration which involves cancellation of small scale modes. The difference arises between hemispherically integrated mock luminosity $\mathcal{L}_{\rm mock}$ and the power spectrum of black-body luminosity (Stefan–Boltzmann law) around the sphere calculated using 3D data.

Comparing the $\ell - \nu$ diagrams of the fullstar run M424 and the run with core heating turned off M438 reveals the presence of multiple p-modes (above Brunt–Väisälä frequency) and g-modes (below Brunt–Väisälä frequency). Marked peaks in the luminosity power spectrum in Figure 3.10 of M424 and M438 at 4000Mm are present both below and above the Brunt–Väisälä frequency, confirming features of both g-modes and p-modes in the spectrum. We also see reflected features of high-frequency p-modes. The dump cadence exceeds the simulation timesteps, causing the Fourier transform algorithm to interpret repeated patterns as modes with frequencies lower than their actual values, which are unresolvable with the dump cadence. The mode features in the $\ell - \nu$ diagrams in Figure 3.12 that follow a linear pattern with negative slope represent these reflected high-frequency p-modes, extending below the marked $\nu_{\rm Brunt}$.

The zoomed $\ell - \nu$ diagram for M424 at 3500Mm in Figure 3.18 enables identification of spatial scales for the marked features (red vertical dot-dashed lines) in Figure 3.10 and Figure 3.11. The 11 μHz and 14 μHz features correspond to $\ell = 1$ modes, confirmed by peaks at these frequencies in the $\ell = 1$ curve in Figure 3.18. Around 19 μHz, we see peaks in both $\ell = 0$ and $\ell = 2$ curves with power in $\ell = 2$ significantly higher than in $\ell = 0$ at this frequency. However, since the contribution of these modes to the mock luminosity power $\mathcal{L}_{\rm mock}$ remains unclear, either mode could dominate the observed signal. Near the 85.2 μHz feature, we see peaks in $\ell = 0$ (85.5 μHz) and $\ell = 1$ (85.7 μHz) p-mode features along with $\ell = 16$ (85.7 μHz) g-mode feature which is along the n=-1 arc. However, all the peaks are slightly offset above the feature. Although the spectral power is maximum for the g-mode feature, we still cannot distinguish which mode's contribution is dominant in $\mathcal{L}_{\rm mock}$.

Figure 3.19 shows coherence times of $\ell = 10$ eigenmodes for run M424 at 3500Mm from Figure 3.15. Mode lifetimes for run M438 at 3500Mm in Figure 3.20 are similar to M424, ranging from 350 h to 750 h. The finite lifetimes of eigenmodes could be a result from complex wave interactions with the turbulent convective boundary which requires further investigation.

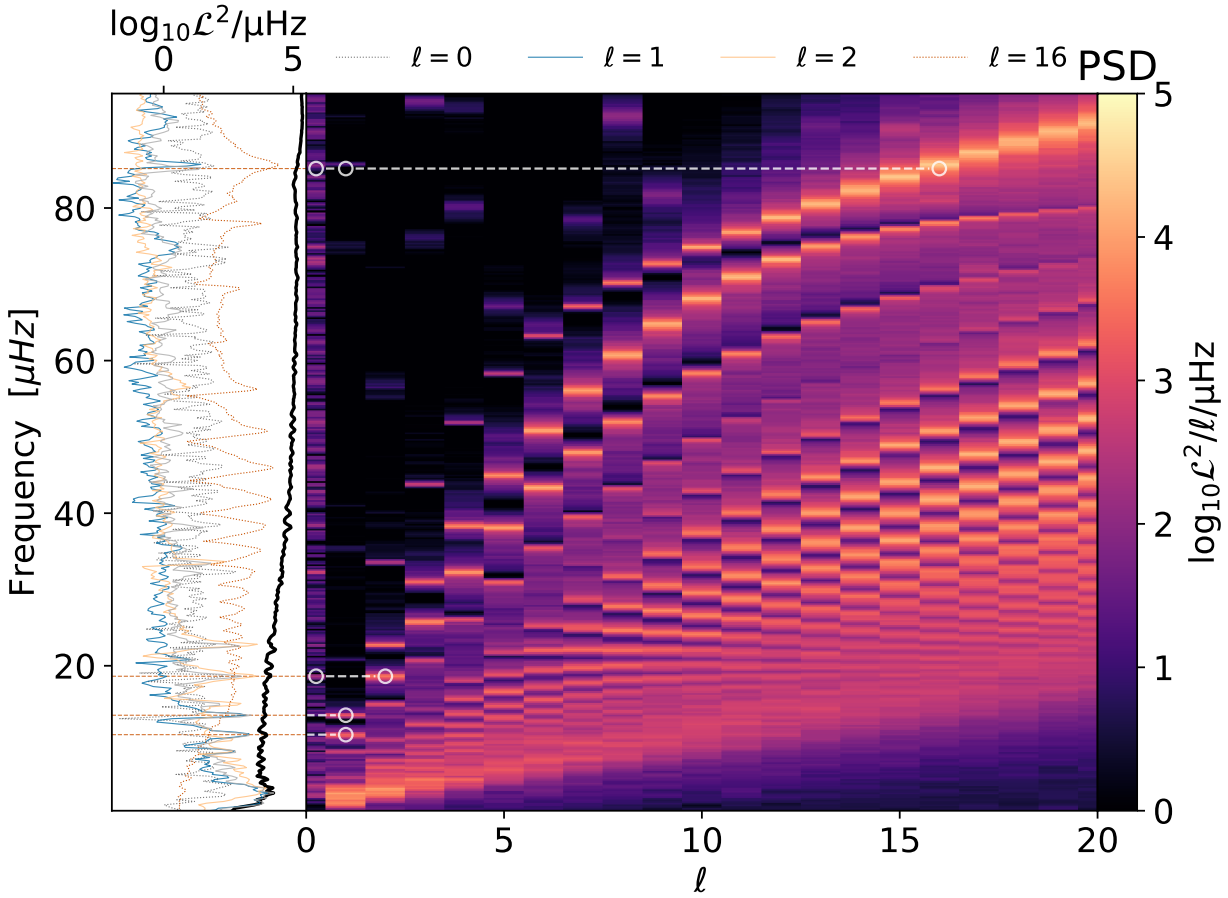

Figure 3.18: Zoomed $\ell - \nu$ diagram for run M424 at 3500Mm showing ℓ range 0–20 and frequency range 0–95 μHz. Panel along the y-axis shows $\mathcal{L}_{\rm 3D}$ and $\mathcal{L}_{\rm mock}$ as in Figure 3.15. Four additional curves show $\mathcal{L}_{\rm 3D}$ power for $\ell = 0$, 1, 2, and 16.

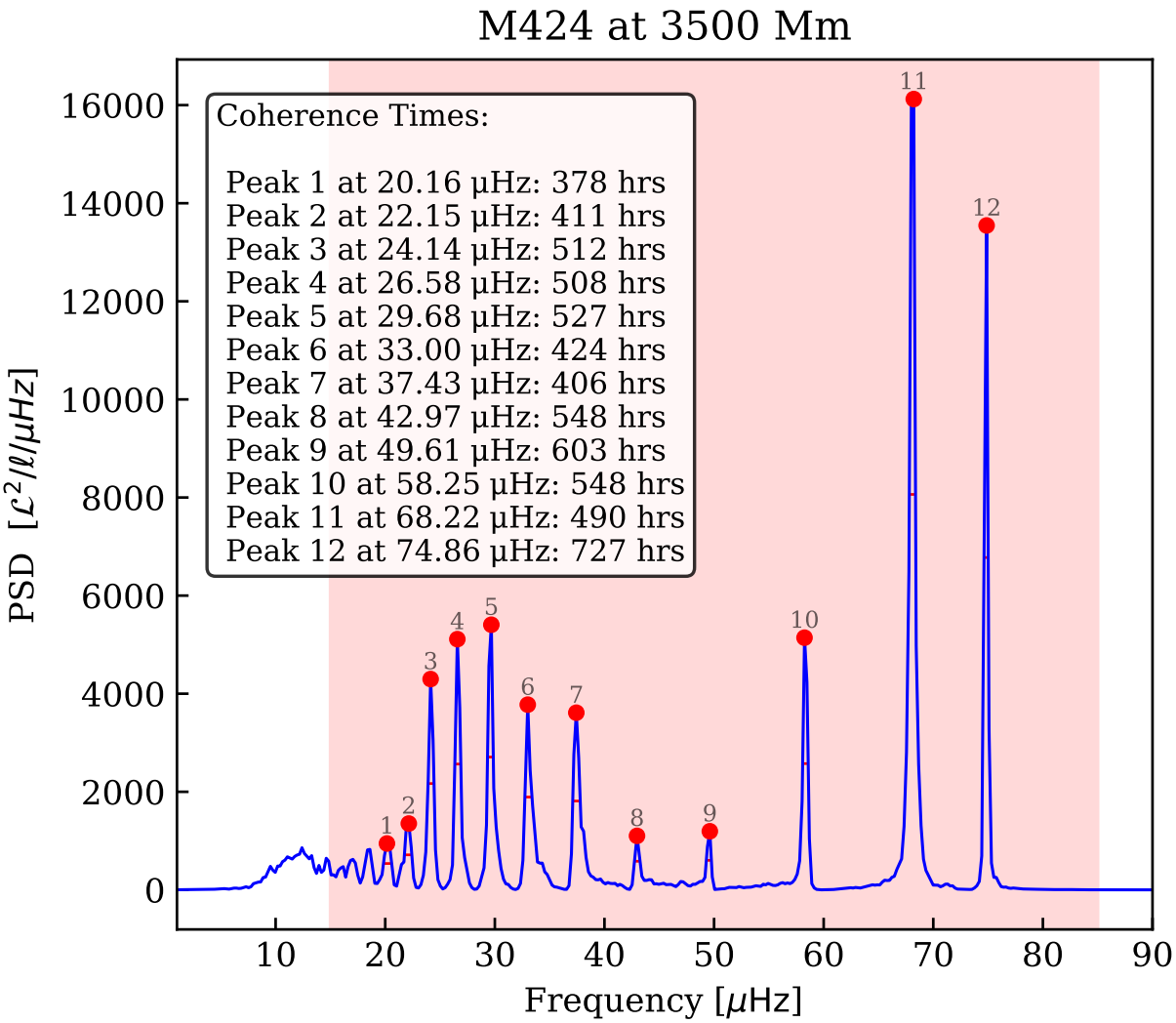

Figure 3.19: Coherence times derived from the full width half maximum of modes at $\ell = 10$ and radial coordinate of 3500Mm for run M424. The red shaded region indicates the analyzed region. Red bullets mark selected peaks with coherence times labeled.

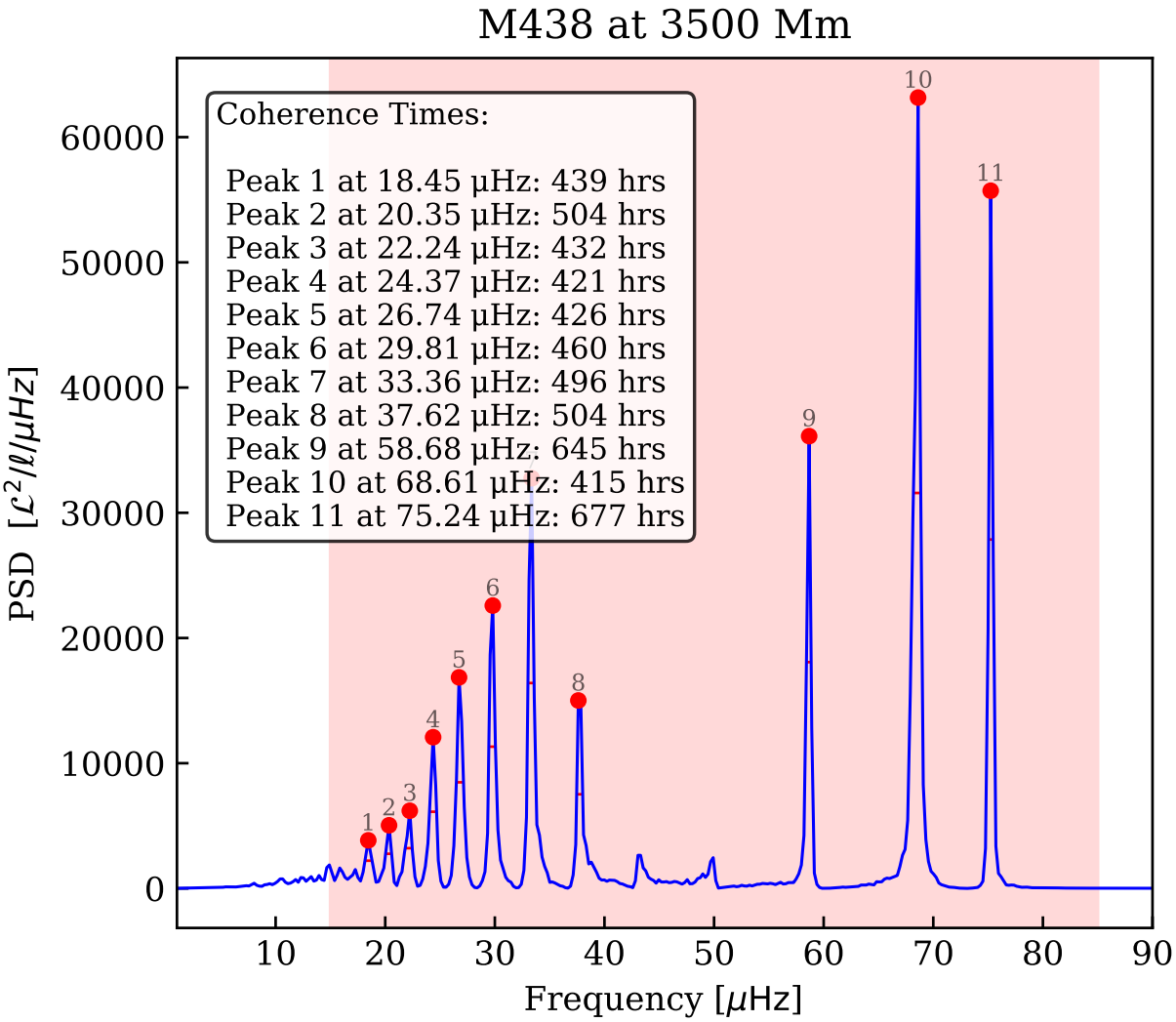

Figure 3.20: Same as Figure 3.19 but for the run M438 at 3500Mm.

3.4.3 Run with just subsurface convection zone

The preceding two runs indicate that core convection has smaller effect to spectral power, suggesting that most low-frequency power originates from the combined effect of IGWs excited near the subsurface convective boundary and from the turbulent subsurface convection zone itself. To quantify the relative contributions of these mechanisms, we conducted run M484, which simulates only the convective envelope.

Figure 3.9(b) shows the simulated thin convective envelope. The size of the envelope convection zone in M484 differs from the full-star run M424 because the penetration zone beyond the Schwarzschild boundary (at 3813Mm) from 3813Mm to approximately 3733Mm (see Appendix A.1) is not included in M484. For this run, a reflective inner boundary was positioned at $R_{min} = 3850$ Mm (with $R_{max} = 4100$ Mm, as in M424). For reference, the Schwarzschild boundary of the convective envelope is located at 3813Mm. This configuration was designed to examine the spectral characteristics of pure convection without IGW interactions. Additional configuration details for simulation M484 are provided in Appendix A.2.

In Figure 3.10, we see that the low-frequency excess power for M484 is significantly reduced compared to M424 and M438 in the envelope region (at 4000Mm). Total integrated power in M484 is 33% less as compared to M424. This means that evanescent IGWs in the subsurface convection zone contribute significantly to the low frequency excess along with the turbulent subsurface convection itself. Following the best-fit lime-colored curve to guide the eye about the trend of the spectra of M484, the power spans roughly one-order-of-magnitude from lowest to highest frequencies, qualitatively different from runs M424 and M438 which exhibit a two-order-of-magnitude power difference similar to the power spectrum of observed light curves in Figure 3.8. These runs include a stable zone below the subsurface convection zone that permits the existence and interaction of IGWs with the subsurface convection zone. The characteristic peaks in M424 and M438 spectra are absent in M484 spectra, supporting that g-mode IGWs are absent due to the lack of a stable layer below the convection zone. The $\ell - \nu$ diagram of M484 in Figure 3.14 exhibits convection patterns with propagating p-mode IGW features but without evanescent g-mode IGW signatures, consistent with the experimental design. Unlike g-mode IGWs, which require $N^2 > 0$ (stable stratification), p-modes can propagate in regions where $N^2 < 0$, the condition in convection zones.

3.4.4 Run without subsurface convection

Simulation M487 is like M424 but excludes the subsurface convection zone to isolate the effect of core convection on the low frequency excess. Due to the radiation diffusion timestep

constraints discussed in Section 3.3, it is impossible with our approach to execute a simulation without the envelope convection zone while maintaining $R_{max} = 4100$ Mm. Consequently, for simulation M487, we positioned the outer boundary R_{max} radially inward at 3600 Mm.

Figure 3.21 confirms the absence of the subsurface convective zone compared to the three previously discussed simulations. As shown in the bottom panel of Figure 3.10, M487 exhibits comparable or greater low-frequency excess levels relative to M424 at 4000Mm. A notable observation is that at frequencies $\leq 10\mu$Hz, the power levels of M487 and M424 at 3500Mm are approximately equivalent, whereas at frequencies $> 10\mu$Hz, M487 demonstrates reduced power levels compared to M424. These results indicate that at 3500Mm, the lower frequency regime ($\leq 10\mu$Hz) is predominantly influenced by IGWs originating from the core, while the higher frequency component is primarily attributable to the presence of the subsurface convection zone. This is further supported by the $\ell - \nu$ diagram for M487 presented in the bottom right panel of Figure 3.17, which shows that the maximum power is concentrated at the lowest frequencies and largest spatial scales (small ℓ values).

3.5 Discussion and Conclusion

We conducted 3D hydrodynamic simulations of a non-rotating 25 $M_\odot$ ZAMS star, encompassing approximately 95% of the stellar structure and including both core and subsurface convection zones. Analysis of the mock lightcurve power spectra reveals three key findings. The luminosity power spectra for the full star run (M424) near the envelope exhibit morphological characteristics qualitatively and quantitatively similar to the observed SLF spectra. Comparison of spectra between the full star run (M424) and the no-core-heating run (M438) at 4000Mm demonstrates small (10%) contribution from the convective core and IGWs excited at the convective core boundary to the low-frequency excess. However, this reduced contribution to observable power does not imply that observable signatures cannot probe core stellar structure. The IGW features present in the mock luminosity spectra depend on the entire stellar stratification, including the core structure, enabling inference of interior properties from surface observations. Comparative analysis of the full star run (M424) and the envelope-only run (M484) at 4000Mm indicates that the low-frequency excess results from combined effects of IGWs and pure subsurface convection, with IGWs being the dominant contributor to excess power at low frequencies, as evidenced by the $a_0 + C_w$ values near $\nu = 0$.

The $\ell - \nu$ diagrams in Figure 3.12, 3.13 and 3.14 for all simulations within the subsurface convection zone at 4000Mm show maximum power spectral density at frequencies

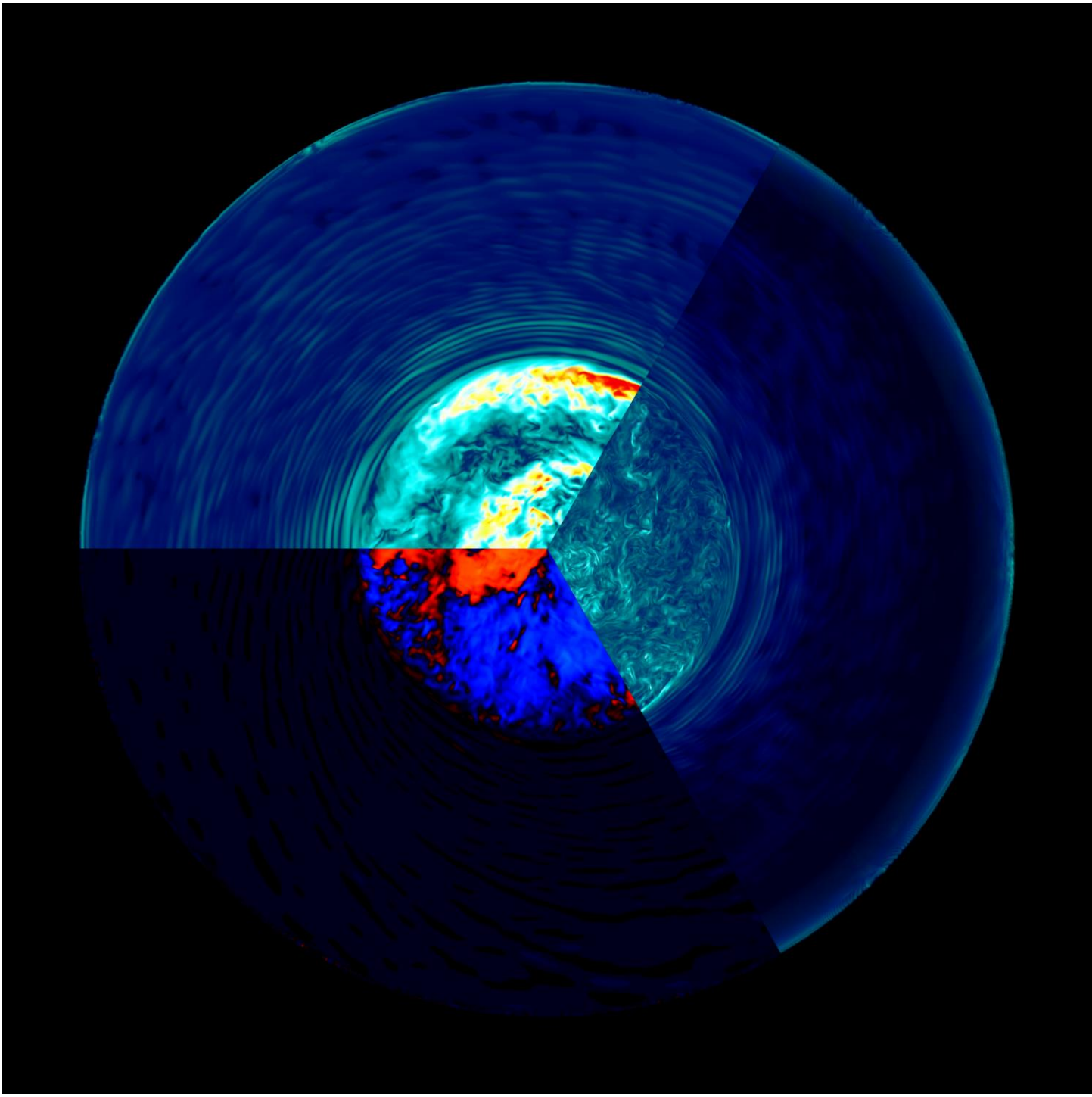

Figure 3.21: Volume rendered images similar to Figure 3.5 for subsequent runs listed in Table 3.1 after M424. (a) M438 (left) (b) M484 (middle) (c) M487 (right).

below 10 μHz. This frequency distribution appears in the mock luminosity power spectra in Figure 3.10, where dominant power occurs at frequencies < 10 μHz across all simulations at 4000Mm (left column). The subsurface convection turnover timescale is ≈ 3 h, corresponding to a convective frequency of 96 μHz. Given a convective frequency, one would expect the maximum power spectral density to occur around that frequency for a convection-dominated region, but the 3D simulations show dominant power at frequencies of order unity μHz, almost an order of magnitude lower than the envelope convective frequency. This pattern was also observed in the 3D wedge simulations of a non-rotating subsurface convection zone of a $35 M_\odot$ main sequence star by Schultz et al. (2022). Our estimate of their convective frequency is 13 μHz[4], while their Lorentzian characteristic frequency $\nu_{\rm char} \approx 110\,\mu$Hz. Despite this characteristic frequency being larger than their convective frequency, their simulations also showed the majority of power spectral density at much lower frequencies, similar to our findings, although they did not explicitly emphasize this point.

This discrepancy between simple convective frequency estimates and observed spectral distributions indicates a fundamental issue with assuming circular convective cells. Figure 3.7 shows the dominant spatial scale of $\ell \approx 40$, which corresponds to the radial extent of the subsurface convection zone. Given the velocities shown in Figure 3.6, circular convective cells would require sizes 10 times larger to accommodate the observed lower frequencies, but this is inconsistent with the observed spatial scales. The convective cells cannot be elongated horizontally either, as this would appear in the tangential velocity spatial spectrum.

The $\ell - \nu$ diagram of the global luminosity fluctuations $\mathcal{L}_{\rm 3D}$ in Figure 3.12 and 3.13 show higher spectral power density in run M438 compared to the fullstar run M424. This appears counterintuitive because M438 omits core volume heating. Core convection is the primary driver of internally generated gravity waves (IGWs) at the stellar core. However, the core remains isentropic in M438, causing it to function as a nearly perfect reflector of IGWs. The core in M424 acts as an imperfect reflector due to turbulent convective motions. The net power in the global luminosity fluctuations $\mathcal{L}_{\rm 3D}$ of the envelope convection run M484 shows higher spectral power density than the fullstar run M424. This enhancement results from two nearby reflecting boundaries in M484, which produce elevated flow velocities.

Our simulations differ from previous 3D hydrodynamic simulation studies of massive main sequence stars addressing SLF variability. Previous studies simulated a wedge or partial stellar structure (e.g. Schultz et al., 2022, 2023). We simulate the star with both core and envelope convection zones in 3D and full 4π geometry. This approach resolves modes and

[4]Convective frequency was not directly reported in Schultz et al. (2022). We used the ratio of convective velocity and the radial extent of convection zone to determine the convective frequency.

eigenwaves at the scale of the entire stratification and assesses their impact on the power spectrum. We take timesteps limited by CFL condition (Courant et al., 1928), thereby resolving pressure modes and their interaction and effects in the dynamics, as opposed to simulations with order of magnitude higher Courant number, and hence larger timesteps, like Anders et al. (2023).

The results from the simulation without envelope convection (M487) show extremely low power levels at higher frequencies ($\nu > 10$ μHz), consistent with Anders et al. (2023). However, we observe significantly elevated power at low frequencies ($\nu \leq 10$ μHz), contrary to their results. This discrepancy may results from two differences between our simulations and theirs. First, their simulations use flow Courant number for timesteps that are orders of magnitude larger than the timesteps we employ based on the CFL condition. Second, their simulations do not capture finite mode lifetimes, the excitation and de-excitation of internal gravity waves (IGWs), as described by Herwig et al. (2023). The ℓ–ν diagram in Figure 3.12 reveal multiple acoustic modes (p-modes) at various scales above the Brunt–Väisälä frequency. The interaction between acoustic waves and large convective plumes could on small scales affect the excitation and de-excitation of IGWs, processes that are not represented in their simulations.

Several limitations must be acknowledged when interpreting these results. Our simulations were performed with both core luminosity and radiative diffusivity set to 100 times their nominal values from the `MESA` model. Previous work by Herwig et al. (2023) shows that core convective velocities scale with core luminosity (L; nuclear burning) as $L^{1/3}$. This indicates that our core convective velocities are enhanced by a factor of approximately 4.64, while the core convective turnover timescale is reduced by the same factor compared to the `MESA` model.

Our simulations exclude the outer 5% of the stellar radius. Waves propagating toward the outer regions could experience additional damping due to radiative diffusion (Bühler, 2009) and amplification due to decreasing density (pseudomomentum conservation, Kumar et al., 1999). Following Rogers and McElwaine (2017), the wave amplitude near the surface, accounting for both effects, can be estimated as:

$$\nu_{\text{wave}}(\omega, k_h, r) = \nu_{\text{rms-cz}} \sqrt{\frac{\rho_{\text{tcz}}}{\rho(r)}} \exp\left[-\tau(\omega, k_h, r)\right] \tag{3.7}$$

$$\implies \frac{\nu_{\text{wave}}(\omega, k_h, r)}{\nu_{\text{rms-cz}}} = \sqrt{\frac{\rho_{\text{tcz}}}{\rho(r)}} \exp\left[-\tau(\omega, k_h, r)\right] \tag{3.8}$$

where $\nu_{\text{wave}}(\omega, k_h, r)$ represents the wave amplitude at outer radial location r for a wave

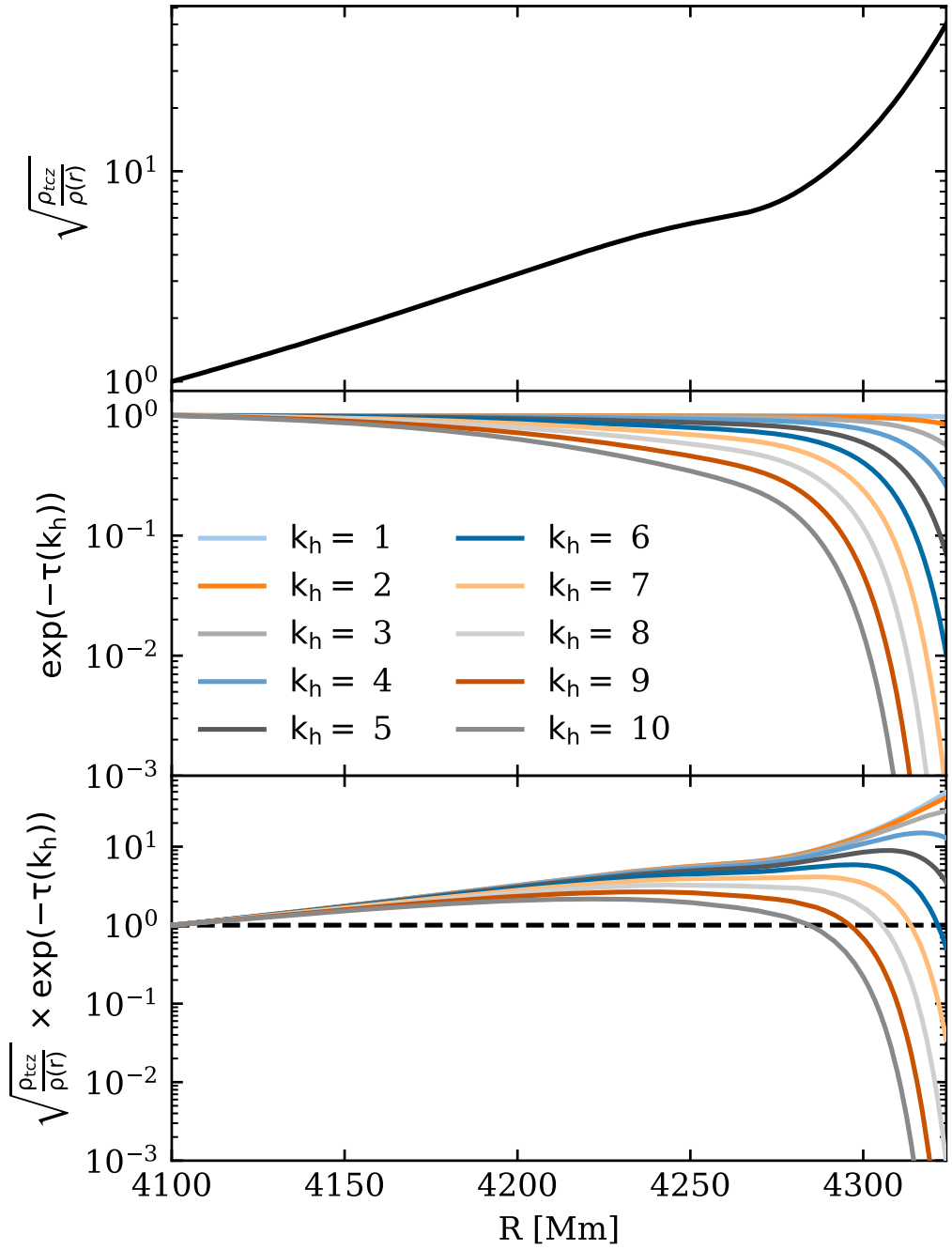

Figure 3.22: Radial dependence of IGW amplification and damping factors. *Top panel:* Wave amplification factor $\sqrt{\rho_{\rm tcz}/\rho(r)}$ due to decreasing density with radius, applicable to all horizontal wavenumbers k_h. *Middle panel:* Wave damping factor $\exp[-\tau(\omega, k_h, r)]$ for horizontal wavenumbers $k_h = 1$ to 10. *Bottom panel:* Combined amplification and damping factor $\nu_{\rm wave}(\omega, k_h, r)/\nu_{\rm rms-cz}$ for $k_h = 1$ to 10. The curves extend from the outer boundary of the fullstar simulation at 4100 Mm to the outer boundary of the `MESA` model at 4322 Mm. Labels are shown only in the middle panel.

of frequency ω, $\nu_{\mathrm{rms-cz}}$ is the rms velocity within the convection zone, k_h is the horizontal wavenumber, ρ_{tcz} is the density at the top of the convection zone, $\rho(r)$ is the density at the outer radial location, and $\tau(\omega, k_h, r)$ is the wave damping optical depth defined as (Kumar et al., 1999):

$$\tau(\omega, k_h, r) = \int_{r_{\mathrm{tcz}}}^{r} \frac{\kappa k_h^3 N^3}{\omega^4 (2\pi r)^3}\, dr \tag{3.9}$$

where r_{tcz} is the radius at the top of the convection zone, κ is the radiative diffusivity at radial location r.

Using parameters from the ZAMS `MESA` model, maximum Brunt–Väisälä frequency near the surface $N \approx 2\pi \times 270\, rad\, s^{-1}$, frequency of the sharpest observed peak in M424 luminosity power spectrum in Figure 3.10 $\omega = 2\pi \times 10\,\mu$Hz, and assuming the subsurface convection zone terminates at 4100Mm with a radiative zone extending to the outer boundary in the `MESA` model at 4322Mm, we calculate wave amplification and dissipation factor radial profiles using Equation 3.8. Figure 3.22 shows that amplitudes of IGWs with $k_h \leq 5$ are amplified whereas higher k_h amplitudes are damped. The $\ell - \nu$ diagram in Figure 3.12 indicate that the peak at around $10\,\mu$Hz corresponds to $\ell \leq 5$. Therefore, assuming the extrapolation using Equation 3.8, some of the marked IGW peaks in Figure 3.10 could be visible near the photosphere.

The implementation of a reflecting outer boundary at 4100Mm, necessitated by challenges in resolving radiation diffusion in the outermost layers, could artificially modify standing IGW amplitudes. This may influence the power spectrum near the surface, as IGW features are evident in the spectrum. This artificial effect is inherent to our simulation approach. Quantifying its impact would be valuable, though the methodology for doing so remains unclear.

Chapter 4

Conclusion and future work

4.1 Conclusion

This thesis presents two distinct investigations into stellar physics using different computational approaches. The first study quantifies systematic uncertainties in white dwarf cooling age determinations arising from uncertainties in core composition profiles, envelope masses, and conductive opacities. Using `MESA` simulations, we demonstrate that these systematic uncertainties are comparable to observational uncertainties and recommend their inclusion in all future white dwarf age studies. The relative age uncertainty ranges from 3-10% for effective temperatures between 20,000-3,000 K, with additional potential delays of 10-50% from ^{22}Ne shell distillation for crystallized white dwarfs.

The second study presents 3D hydrodynamic simulations of a 25 $M_\odot$ main-sequence star spanning 95% of the stellar structure, incorporating both core and subsurface convection zones. The simulations reproduce power spectra qualitatively similar to observed stochastic low-frequency variability in massive stars. Through systematic comparison of different stellar configurations, we identify that the low-frequency excess results primarily from internal gravity waves excited at the subsurface convective boundary, with minimal contribution from core convection. The work on white dwarf cooling provided essential experience with 1D stellar evolution codes, which subsequently informed the construction of initial conditions for the 3D hydrodynamic simulations described in the second study.

4.2 Future Work

The white dwarf cooling age uncertainty study provides a framework for systematic uncertainty assessment that we encourage the astronomical community to incorporate with observational uncertainties when determining cooling ages. This work has been cited by three

publications (Roberts et al., 2025; Limbach et al., 2025; Vorberger et al., 2025), demonstrating its immediate utility. The study identifies envelope hydrogen and helium layer thicknesses as critical parameters affecting cooling timescales. Future work could employ 3D hydrodynamic simulations of the pre-white dwarf evolutionary phase to better constrain these envelope parameters and reduce systematic uncertainties.

The spread in envelope hydrogen and helium layer thicknesses represents a fundamental uncertainty that cannot be fully eliminated through improved stellar evolution modeling, as it reflects the diverse evolutionary pathways leading to white dwarf formation. White dwarfs of identical mass can form through different channels: some progenitors experience late thermal pulses that burn most of their hydrogen envelopes, others undergo born-again episodes with partial hydrogen depletion, while binary evolution can strip envelope material through mass transfer or common envelope phases. Additionally, as white dwarfs cool, some hydrogen-atmosphere (DA) white dwarfs transition to helium-atmosphere (DB) white dwarfs when a deepening superficial convection zone within the helium layer eventually reaches and dilutes the outer hydrogen envelope. The onset temperature of this DA→DB transformation depends critically on the initial hydrogen and helium layer thicknesses and the detailed mixing processes at the envelope interface. Dr. Simon Blouin has initiated a project using 3D plane-parallel hydrodynamic simulations of white dwarf atmospheres using `PPMstar` to investigate these mixing processes and better understand the DA→DB transformation, which will help constrain envelope evolution and reduce associated cooling age uncertainties.

The 3D hydrodynamic simulations of massive stars present multiple avenues for future investigation. Parameter studies examining the dependence of power spectra on stellar rotation, mass, metallicity, and evolutionary phase (zero-age, mid, or terminal-age main sequence) would provide comprehensive understanding of stochastic low-frequency variability across different stellar populations. The current simulations employ reflecting outer boundary conditions that may artificially enhance internal gravity wave amplitudes. Implementation of free outer boundary conditions would provide more realistic wave propagation and damping in the stellar envelope.

Detailed spectral analysis to identify specific peaks and map them to individual eigenmodes in observed spectra represents another important direction. The artificial enhancement of the subsurface convection zone implemented in Chapter 3 could be relaxed in future simulations to achieve more realistic stellar models. These modifications require substantial code development within the `PPMstar` framework.

Several of these proposed improvements require code modifications to the `PPMstar` framework. Our group maintains ongoing collaboration with the `PPMstar` code architect Prof. Paul

Woodward. Through an IReNA Visiting Fellowship, a scheduled visit to Prof. Woodward in July 2025 will focus on learning code development techniques and implementing modifications essential for these future investigations. This work will serve as the foundation for PhD research under the supervision of Prof. Falk Herwig.

The ultimate goal of this research is to understand the oscillation physics underlying stochastic low-frequency variability in massive stars and develop the capability to invert observed low-frequency spectra to reconstruct internal stellar flow fields. This could enable direct inference of convective velocities, mixing length parameters, and turbulent structure from external photometric observations. Such capabilities could revolutionize our understanding of internal mixing processes, which remain one of the fundamental uncertainties in stellar physics. Current stellar evolution models rely on parametric prescriptions for convective mixing, but direct observational constraints on these processes are lacking. The ability to probe stellar interiors through asteroseismology could provide empirical validation of mixing theories and constrain key parameters governing stellar structure and evolution. These parameters include convective core sizes, overshooting distances, rotation-induced mixing rates,etc.

The aim is to enable full scientific utilization of upcoming observational capabilities. Time-resolved spectroscopy of oscillating stars will provide unprecedented detail on surface velocity patterns and their correlation with internal dynamics. Understanding the physics of microturbulence through comparison of simulated and observed spectral line profiles will improve stellar parameter determinations and abundance measurements. Space-based missions including PLATO (PLAnetary Transits and Oscillations of stars), CubeSpec and HAYDN (High-precision AsteroseismologY in DeNse stellar fields) will deliver high-precision photometric and spectroscopic time series spanning extended durations. The combination of these advanced observational data with detailed 3D stellar models will establish asteroseismology as a precision tool for stellar interior diagnostics.

Bibliography

Aerts, C. (2021). Probing the interior physics of stars through asteroseismology. *Reviews of Modern Physics*, 93(1):015001.

Aerts, C., Christensen-Dalsgaard, J., and Kurtz, D. W. (2010). *Asteroseismology*.

Aerts, C. and Rogers, T. M. (2015). Observational Signatures of Convectively Driven Waves in Massive Stars. , 806(2):L33.

Althaus, L. G., Córsico, A. H., Isern, J., and García-Berro, E. (2010). Evolutionary and pulsational properties of white dwarf stars. , 18(4):471–566.

Anders, E. H., Lecoanet, D., Cantiello, M., Burns, K. J., Hyatt, B. A., Kaufman, E., Townsend, R. H. D., Brown, B. P., Vasil, G. M., Oishi, J. S., and Jermyn, A. S. (2023). The photometric variability of massive stars due to gravity waves excited by core convection. *Nature Astronomy*, 7:1228–1234.

Andrassy, R., Herwig, F., Woodward, P., and Ritter, C. (2020). 3D hydrodynamic simulations of C ingestion into a convective O shell. , 491(1):972–992.

Andrassy, R., Higl, J., Mao, H., Mocák, M., Vlaykov, D. G., Arnett, W. D., Baraffe, I., Campbell, S. W., Constantino, T., Edelmann, P. V. F., Goffrey, T., Guillet, T., Herwig, F., Hirschi, R., Horst, L., Leidi, G., Meakin, C., Pratt, J., Rizzuti, F., Röpke, F. K., and Woodward, P. (2022). Dynamics in a stellar convective layer and at its boundary: Comparison of five 3D hydrodynamics codes. , 659:A193.

Arazimova, E., Kawka, A., and Vennes, S. (2009). Spectroscopic Observations of High Proper Motion DA White Dwarfs. *Publications de l'Observatoire Astronomique de Beograd*, 86:297–300.

Arnett, D. (1996). *Supernovae and Nucleosynthesis: An Investigation of the History of Matter from the Big Bang to the Present*.

Baker, N. and Kippenhahn, R. (1962). The Pulsations of Models of δ Cephei Stars. With 17 Figures in the Text. , 54:114.

Bauer, E. B. (2023). Carbon-Oxygen Phase Separation in Modules for Experiments in Stellar Astrophysics (MESA) White Dwarf Models. , 950(2):115.

Bédard, A., Bergeron, P., Brassard, P., and Fontaine, G. (2020). On the Spectral Evolution of Hot White Dwarf Stars. I. A Detailed Model Atmosphere Analysis of Hot White Dwarfs from SDSS DR12. , 901(2):93.

Blomme, R., Mahy, L., Catala, C., Cuypers, J., Gosset, E., Godart, M., Montalban, J., Ventura, P., Rauw, G., Morel, T., Degroote, P., Aerts, C., Noels, A., Michel, E., Baudin, F., Baglin, A., Auvergne, M., and Samadi, R. (2011). Variability in the CoRoT photometry of three hot O-type stars. HD 46223, HD 46150, and HD 46966. , 533:A4.

Blouin, S. (2024). White dwarf fundamentals. *arXiv e-prints*, page arXiv:2409.03941.

Blouin, S. and Daligault, J. (2021). Direct evaluation of the phase diagrams of dense multi-component plasmas by integration of the Clapeyron equations. , 103(4):043204.

Blouin, S., Daligault, J., and Saumon, D. (2021). ^{22}Ne Phase Separation as a Solution to the Ultramassive White Dwarf Cooling Anomaly. , 911(1):L5.

Blouin, S., Herwig, F., Mao, H., Denissenkov, P., and Woodward, P. R. (2024). 3D hydrodynamics simulations of a 3 $M_\odot$ core helium burning star. , 527(3):4847–4862.

Blouin, S., Mao, H., Herwig, F., Denissenkov, P., Woodward, P. R., and Thompson, W. R. (2023). 3D hydrodynamics simulations of internal gravity waves in red giant branch stars. , 522(2):1706–1725.

Blouin, S., Shaffer, N. R., Saumon, D., and Starrett, C. E. (2020). New Conductive Opacities for White Dwarf Envelopes. , 899(1):46.

Blouin, S., Shaffer, N. R., Saumon, D., and Starrett, C. E. (2020). New conductive opacities for white dwarf envelopes. *The Astrophysical Journal*, 899(1):46.

Blouin, S. and Xu, S. (2022). No evidence for a strong decrease of planetesimal accretion in old white dwarfs. , 510(1):1059–1067.

Böhm-Vitense, E. (1958). Über die Wasserstoffkonvektionszone in Sternen verschiedener Effektivtemperaturen und Leuchtkräfte. Mit 5 Textabbildungen. , 46:108.

Bowman, D. M. (2023). Making waves in massive star asteroseismology. , 368(12):107.

Bowman, D. M., Aerts, C., Johnston, C., Pedersen, M. G., Rogers, T. M., Edelmann, P. V. F., Simón-Díaz, S., Van Reeth, T., Buysschaert, B., Tkachenko, A., and Triana, S. A. (2019a). Photometric detection of internal gravity waves in upper main-sequence stars. I. Methodology and application to CoRoT targets. , 621:A135.

Bowman, D. M., Burssens, S., Pedersen, M. G., Johnston, C., Aerts, C., Buysschaert, B., Michielsen, M., Tkachenko, A., Rogers, T. M., Edelmann, P. V. F., Ratnasingam, R. P., Simón-Díaz, S., Castro, N., Moravveji, E., Pope, B. J. S., White, T. R., and De Cat, P. (2019b). Low-frequency gravity waves in blue supergiants revealed by high-precision space photometry. *Nature Astronomy*, 3:760–765.

Bowman, D. M., Burssens, S., Simon-Diaz, S., Edelmann, P. V. F., Rogers, T. M., Horst, L., Ropke, F. K., and Aerts, C. (2020). VizieR Online Data Catalog: OB stars TESS phot. & high-resolution spectroscopy (Bowman+, 2020). VizieR On-line Data Catalog: J/A+A/640/A36. Originally published in: 2020A&A...640A..36B.

Bowman, D. M., Van Daele, P., Michielsen, M., and Van Reeth, T. (2024). Photometric detection of internal gravity waves in upper main-sequence stars: IV. Comparable stochastic low-frequency variability in SMC, LMC, and Galactic massive stars. , 692:A49.

Brickhill, A. J. (1991). The pulsations of ZZ Ceti stars. III. The driving mechanism. , 251:673–680.

Bromm, V. (2013). Formation of the first stars. *Reports on Progress in Physics*, 76(11):112901.

Bühler, O. (2009). *Waves and Mean Flows*. Cambridge Monographs on Mechanics. Cambridge University Press.

Cantiello, M., Langer, N., Brott, I., de Koter, A., Shore, S. N., Vink, J. S., Voegler, A., Lennon, D. J., and Yoon, S. C. (2009). Sub-surface convection zones in hot massive stars and their observable consequences. , 499(1):279–290.

Cantiello, M., Lecoanet, D., Jermyn, A. S., and Grassitelli, L. (2021). On the Origin of Stochastic, Low-Frequency Photometric Variability in Massive Stars. , 915(2):112.

Caron, A., Bergeron, P., Blouin, S., and Leggett, S. K. (2023). A spectrophotometric analysis of cool white dwarfs in the Gaia and pan-STARRS footprint. , 519(3):4529–4549.

Cassisi, S., Potekhin, A. Y., Pietrinferni, A., Catelan, M., and Salaris, M. (2007). Updated Electron-Conduction Opacities: The Impact on Low-Mass Stellar Models. , 661(2):1094–1104.

Cassisi, S., Potekhin, A. Y., Salaris, M., and Pietrinferni, A. (2021). Electron conduction opacities at the transition between moderate and strong degeneracy: Uncertainties and impacts on stellar models. , 654:A149.

Chandrasekhar, S. (1931). The Maximum Mass of Ideal White Dwarfs. , 74:81.

Chidester, M. and Timmes, F. (2022). On Trapped Modes In Variable White Dwarfs As Probes of the ^{12}C(α,γ)^{16}O Reaction Rate. In *American Astronomical Society Meeting #240*, volume 240 of *American Astronomical Society Meeting Abstracts*, page 415.05.

Chidester, M. T., Timmes, F. X., and Farag, E. (2023). Seismic Signatures of the ^{12}C(α, γ)^{16}O Reaction Rate in White Dwarf Models with Overshooting. , 954(1):51.

Choi, J., Dotter, A., Conroy, C., Cantiello, M., Paxton, B., and Johnson, B. D. (2016). Mesa Isochrones and Stellar Tracks (MIST). I. Solar-scaled Models. , 823(2):102.

Cimatti, A. and Moresco, M. (2023). Revisiting the Oldest Stars as Cosmological Probes: New Constraints on the Hubble Constant. , 953(2):149.

Clarkson, O., Herwig, F., Andrassy, R., Woodward, P., Pignatari, M., and Mao, H. (2019). H-He Shell Interactions and Nucleosynthesis in Massive Population III Stars. In *Nuclei in the Cosmos XV*, volume 219, pages 321–325.

Colella, P. and Woodward, P. R. (1984). The piecewise parabolic method (ppm) for gas-dynamical simulations. *Journal of Computational Physics*, 54(1):174–201.

Constantino, T., Campbell, S. W., Christensen-Dalsgaard, J., Lattanzio, J. C., and Stello, D. (2015). The treatment of mixing in core helium burning models - I. Implications for asteroseismology. , 452(1):123–145.

Courant, R., Friedrichs, K., and Lewy, H. (1928). Über die partiellen Differenzengleichungen der mathematischen Physik. *Mathematische Annalen*, 100:32–74.

Cox, J. P. and Giuli, R. T. (1968). *Principles of stellar structure*.

Cukanovaite, E., Tremblay, P. E., Toonen, S., Temmink, K. D., Manser, C. J., O'Brien, M. W., and McCleery, J. (2023). Local stellar formation history from the 40 pc white dwarf sample. , 522(2):1643–1661.

Cyburt, R. H., Fields, B. D., Olive, K. A., and Yeh, T.-H. (2016). Big bang nucleosynthesis: Present status. *Reviews of Modern Physics*, 88(1):015004.

De Gerónimo, F. C., Althaus, L. G., Córsico, A. H., Romero, A. D., and Kepler, S. O. (2017). Asteroseismology of ZZ Ceti stars with fully evolutionary white dwarf models. I. The impact of the uncertainties from prior evolution on the period spectrum. , 599:A21.

De Gerónimo, F. C., Battich, T., Miller Bertolami, M. M., Althaus, L. G., and Córsico, A. H. (2019). On the recent parametric determination of an asteroseismological model for the DBV star KIC 08626021. , 630:A100.

Denissenkov, P. A., Herwig, F., Woodward, P., Andrassy, R., Pignatari, M., and Jones, S. (2019). The i-process yields of rapidly accreting white dwarfs from multicycle He-shell flash stellar evolution models with mixing parametrizations from 3D hydrodynamics simulations. , 488(3):4258–4270.

Dotter, A. (2016). MESA Isochrones and Stellar Tracks (MIST) 0: Methods for the Construction of Stellar Isochrones. , 222(1):8.

Edelmann, P. V. F., Ratnasingam, R. P., Pedersen, M. G., Bowman, D. M., Prat, V., and Rogers, T. M. (2019). Three-dimensional Simulations of Massive Stars. I. Wave Generation and Propagation. , 876(1):4.

Elms, A. K., Tremblay, P.-E., Gänsicke, B. T., Koester, D., Hollands, M. A., Gentile Fusillo, N. P., Cunningham, T., and Apps, K. (2022). Spectral analysis of ultra-cool white dwarfs polluted by planetary debris. , 517(3):4557–4574.

Fantin, N. J., Côté, P., McConnachie, A. W., Bergeron, P., Cuillandre, J.-C., Gwyn, S. D. J., Ibata, R. A., Thomas, G. F., Carlberg, R. G., Fabbro, S., Haywood, M., Lançon, A., Lewis, G. F., Malhan, K., Martin, N. F., Navarro, J. F., Scott, D., and Starkenburg, E. (2019). The Canada-France Imaging Survey: Reconstructing the Milky Way Star Formation History from Its White Dwarf Population. , 887(2):148.

Fields, B. D., Olive, K. A., Yeh, T.-H., and Young, C. (2020). Big-Bang Nucleosynthesis after Planck. , 2020(3):010.

Fontaine, G., Brassard, P., and Bergeron, P. (2001). The Potential of White Dwarf Cosmochronology. , 113(782):409–435.

Gaia Collaboration, Babusiaux, C., van Leeuwen, F., Barstow, M. A., Jordi, C., Vallenari, A., Bossini, D., Bressan, A., Cantat-Gaudin, T., van Leeuwen, M., Brown, A. G. A., Prusti, T., de Bruijne, J. H. J., Bailer-Jones, C. A. L., Biermann, M., Evans, D. W., Eyer, L., Jansen, F., Klioner, S. A., Lammers, U., Lindegren, L., Luri, X., Mignard, F., Panem, C., Pourbaix, D., Randich, S., Sartoretti, P., Siddiqui, H. I., Soubiran, C., Walton, N. A., Arenou, F., Bastian, U., Cropper, M., Drimmel, R., Katz, D., Lattanzi, M. G., Bakker, J., Cacciari, C., Castañeda, J., Chaoul, L., Cheek, N., De Angeli, F., Fabricius, C., Guerra, R., Holl, B., Masana, E., Messineo, R., Mowlavi, N., Nienartowicz, K., Panuzzo, P., Portell, J., Riello, M., Seabroke, G. M., Tanga, P., Thévenin, F., Gracia-Abril, G., Comoretto, G., Garcia-Reinaldos, M., Teyssier, D., Altmann, M., Andrae, R., Audard, M., Bellas-Velidis, I., Benson, K., Berthier, J., Blomme, R., Burgess, P., Busso, G., Carry, B., Cellino, A., Clementini, G., Clotet, M., Creevey, O., Davidson, M., De Ridder, J., Delchambre, L., Dell'Oro, A., Ducourant, C., Fernández-Hernández, J., Fouesneau, M., Frémat, Y., Galluccio, L., García-Torres, M., González-Núñez, J., González-Vidal, J. J., Gosset, E., Guy, L. P., Halbwachs, J. L., Hambly, N. C., Harrison, D. L., Hernández, J., Hestroffer, D., Hodgkin, S. T., Hutton, A., Jasniewicz, G., Jean-Antoine-Piccolo, A., Jordan, S., Korn, A. J., Krone-Martins, A., Lanzafame, A. C., Lebzelter, T., Löffler, W., Manteiga, M., Marrese, P. M., Martín-Fleitas, J. M., Moitinho, A., Mora, A., Muinonen, K., Osinde, J., Pancino, E., Pauwels, T., Petit, J. M., Recio-Blanco, A., Richards, P. J., Rimoldini, L., Robin, A. C., Sarro, L. M., Siopis, C., Smith, M., Sozzetti, A., Süveges, M., Torra, J., van Reeven, W., Abbas, U., Abreu Aramburu, A., Accart, S., Aerts, C., Altavilla, G., Álvarez, M. A., Alvarez, R., Alves, J., Anderson, R. I., Andrei, A. H., Anglada Varela, E., Antiche, E., Antoja, T., Arcay, B., Astraatmadja, T. L., Bach, N., Baker, S. G., Balaguer-Núñez, L., Balm, P., Barache, C., Barata, C., Barbato, D., Barblan, F., Barklem, P. S., Barrado, D., Barros, M., Bartholomé Muñoz, L., Bassilana, J. L., Becciani, U., Bellazzini, M., Berihuete, A., Bertone, S., Bianchi, L., Bienaymé, O., Blanco-Cuaresma, S., Boch, T., Boeche, C., Bombrun, A., Borrachero, R., Bouquillon, S., Bourda, G., Bragaglia, A., Bramante, L., Breddels, M. A., Brouillet, N., Brüsemeister, T., Brugaletta, E., Bucciarelli, B., Burlacu, A., Busonero, D., Butkevich, A. G., Buzzi, R., Caffau, E., Cancelliere, R., Cannizzaro, G., Carballo, R., Carlucci, T., Carrasco, J. M., Casamiquela, L., Castellani, M., Castro-Ginard, A., Charlot, P., Chemin, L., Chiavassa, A., Cocozza, G., Costigan, G., Cowell, S., Crifo, F., Crosta, M., Crowley, C., Cuypers, J., Dafonte, C., Damerdji, Y.,

Dapergolas, A., David, P., David, M., and de Laverny, P. (2018a). Gaia Data Release 2. Observational Hertzsprung-Russell diagrams. , 616:A10.

Gaia Collaboration, Babusiaux, C., van Leeuwen, F., Barstow, M. A., Jordi, C., Vallenari, A., Bossini, D., Bressan, A., Cantat-Gaudin, T., van Leeuwen, M., and et al. (2018b). Gaia Data Release 2. Observational Hertzsprung-Russell diagrams. , 616:A10.

García-Berro, E. and Althaus, G. L. (2013). Stellar Structure. In Oswalt, T. D. and Barstow, M. A., editors, *Planets, Stars and Stellar Systems. Volume 4: Stellar Structure and Evolution*, volume 4, page 1.

García-Berro, E., Torres, S., Althaus, L. G., Renedo, I., Lorén-Aguilar, P., Córsico, A. H., Rohrmann, R. D., Salaris, M., and Isern, J. (2010). A white dwarf cooling age of 8Gyr for NGC 6791 from physical separation processes. , 465(7295):194–196.

Giammichele, N., Charpinet, S., and Brassard, P. (2022). Seismic Cartography of White-Dwarf Interiors From the Toulouse-Montréal Optimal-Design Approach. *Frontiers in Astronomy and Space Sciences*, 9:879045.

Giammichele, N., Charpinet, S., Fontaine, G., and Brassard, P. (2017). Toward High-precision Seismic Studies of White Dwarf Stars: Parametrization of the Core and Tests of Accuracy. , 834(2):136.

Giammichele, N., Charpinet, S., Fontaine, G., Brassard, P., Green, E. M., Van Grootel, V., Bergeron, P., Zong, W., and Dupret, M. A. (2018). A large oxygen-dominated core from the seismic cartography of a pulsating white dwarf. , 554(7690):73–76.

Handler, G. (2013). Asteroseismology. In Oswalt, T. D. and Barstow, M. A., editors, *Planets, Stars and Stellar Systems. Volume 4: Stellar Structure and Evolution*, volume 4, page 207.

Hansen, C. J., Kawaler, S. D., and Trimble, V. (2004). *Stellar interiors : physical principles, structure, and evolution*.

Heger, A., Fryer, C. L., Woosley, S. E., Langer, N., and Hartmann, D. H. (2003). How Massive Single Stars End Their Life. , 591(1):288–300.

Herwig, F. (2000). The evolution of AGB stars with convective overshoot. , 360:952–968.

Herwig, F. (2005). Evolution of Asymptotic Giant Branch Stars. , 43(1):435–479.

Herwig, F. (2013). Evolution of Solar and Intermediate-Mass Stars. In Oswalt, T. D. and Barstow, M. A., editors, *Planets, Stars and Stellar Systems. Volume 4: Stellar Structure and Evolution*, volume 4, page 397.

Herwig, F., Pignatari, M., Woodward, P. R., Porter, D. H., Rockefeller, G., Fryer, C. L., Bennett, M., and Hirschi, R. (2011). Convective-reactive Proton-^{12}C Combustion in Sakurai's Object (V4334 Sagittarii) and Implications for the Evolution and Yields from the First Generations of Stars. , 727(2):89.

Herwig, F., Woodward, P. R., Lin, P.-H., Knox, M., and Fryer, C. (2014). Global Non-spherical Oscillations in Three-dimensional 4π Simulations of the H-ingestion Flash. , 792(1):L3.

Herwig, F., Woodward, P. R., Mao, H., Thompson, W. R., Denissenkov, P., Lau, J., Blouin, S., Andrassy, R., and Paul, A. (2023). 3D hydrodynamic simulations of massive main-sequence stars - I. Dynamics and mixing of convection and internal gravity waves. , 525(2):1601–1629.

Hollands, M. A., Gänsicke, B. T., and Koester, D. (2018). Cool DZ white dwarfs II: compositions and evolution of old remnant planetary systems. , 477(1):93–111.

Horst, L., Edelmann, P. V. F., Andrássy, R., Röpke, F. K., Bowman, D. M., Aerts, C., and Ratnasingam, R. P. (2020). Fully compressible simulations of waves and core convection in main-sequence stars. , 641:A18.

Isern, J. (2019). The Star Formation History in the Solar Neighborhood as Told by Massive White Dwarfs. , 878(1):L11.

Isern, J., Hernanz, M., Mochkovitch, R., and Garcia-Berro, E. (1991). The role of the minor chemical species in the cooling of white dwarfs. , 241(1):L29–L32.

Jermyn, A. S., Anders, E. H., and Cantiello, M. (2022). A Transparent Window into Early-type Stellar Variability. , 926(2):221.

Jermyn, A. S., Bauer, E. B., Schwab, J., Farmer, R., Ball, W. H., Bellinger, E. P., Dotter, A., Joyce, M., Marchant, P., Mombarg, J. S. G., Wolf, W. M., Sunny Wong, T. L., Cinquegrana, G. C., Farrell, E., Smolec, R., Thoul, A., Cantiello, M., Herwig, F., Toloza, O., Bildsten, L., Townsend, R. H. D., and Timmes, F. X. (2023). Modules for Experiments in Stellar Astrophysics (MESA): Time-dependent Convection, Energy Conservation, Automatic Differentiation, and Infrastructure. , 265(1):15.

Jones, S., Andrassy, R., Sandalski, S., Davis, A., Woodward, P., and Herwig, F. (2017). Idealized hydrodynamic simulations of turbulent oxygen-burning shell convection in 4π geometry. , 465(3):2991–3010.

Kaiser, B. C., Clemens, J. C., Blouin, S., Dufour, P., Hegedus, R. J., Reding, J. S., and Bédard, A. (2021). Lithium pollution of a white dwarf records the accretion of an extrasolar planetesimal. *Science*, 371(6525):168–172.

Kalirai, J. S. (2012). The age of the milky way inner halo. *Nature*, 486(7401):90–92.

Karakas, A. I. and Lattanzio, J. C. (2014). The Dawes Review 2: Nucleosynthesis and Stellar Yields of Low- and Intermediate-Mass Single Stars. , 31:e030.

Kilic, M., Munn, J. A., Harris, H. C., von Hippel, T., Liebert, J. W., Williams, K. A., Jeffery, E., and DeGennaro, S. (2017). The Ages of the Thin Disk, Thick Disk, and the Halo from Nearby White Dwarfs. , 837(2):162.

Kiman, R., Xu, S., Faherty, J. K., Gagné, J., Angus, R., Brandt, T. D., Casewell, S. L., and Cruz, K. L. (2022). wdwarfdate: A Python Package to Derive Bayesian Ages of White Dwarfs. , 164(2):62.

Kippenhahn, R., Weigert, A., and Weiss, A. (2013). *Stellar Structure and Evolution*.

Krtička, J. and Feldmeier, A. (2018). Light variations due to the line-driven wind instability and wind blanketing in O stars. , 617:A121.

Krtička, J. and Feldmeier, A. (2021). Stochastic light variations in hot stars from wind instability: finding photometric signatures and testing against the TESS data. , 648:A79.

Kumar, P., Talon, S., and Zahn, J.-P. (1999). Angular Momentum Redistribution by Waves in the Sun. , 520(2):859–870.

Le Saux, A., Baraffe, I., Guillet, T., Vlaykov, D. G., Morison, A., Pratt, J., Constantino, T., and Goffrey, T. (2023). Two-dimensional simulations of internal gravity waves in a 5 $M_\odot$ zero-age-main-sequence model. , 522(2):2835–2849.

Lecoanet, D., Cantiello, M., Anders, E. H., Quataert, E., Couston, L.-A., Bouffard, M., Favier, B., and Le Bars, M. (2021). Surface manifestation of stochastically excited internal gravity waves. , 508(1):132–143.

Lecoanet, D., Cantiello, M., Quataert, E., Couston, L.-A., Burns, K. J., Pope, B. J. S., Jermyn, A. S., Favier, B., and Le Bars, M. (2019). Low-frequency Variability in Massive Stars: Core Generation or Surface Phenomenon? , 886(1):L15.

Limbach, M. A., Vanderburg, A., MacDonald, R. J., Stevenson, K. B., Jenkins, S., Blouin, S., Rauscher, E., Bowens-Rubin, R., Gallo, E., Mang, J., Morley, C. V., Sing, D. K., O'Connor, C., Venner, A., and Xu, S. (2025). Thermal Emission and Confirmation of the Frigid White Dwarf Exoplanet WD 1856+534 b. , 984(1):L28.

Mao, H., Woodward, P., Herwig, F., Denissenkov, P. A., Blouin, S., Thompson, W., and McDermott, B. (2024). 3D Hydrodynamic Simulations of Massive Main-sequence Stars. III. The Effect of Radiation Pressure and Diffusion Leading to a 1D Equilibrium Model. , 975(2):271.

Mazumdar, A., Monteiro, M. J. P. F. G., Ballot, J., Antia, H. M., Basu, S., Houdek, G., Mathur, S., Cunha, M. S., Silva Aguirre, V., García, R. A., Salabert, D., Verner, G. A., Christensen-Dalsgaard, J., Metcalfe, T. S., Sanderfer, D. T., Seader, S. E., Smith, J. C., and Chaplin, W. J. (2014). Measurement of Acoustic Glitches in Solar-type Stars from Oscillation Frequencies Observed by Kepler. , 782(1):18.

Mestel, L. (1952). On the theory of white dwarf stars. I. The energy sources of white dwarfs. , 112:583.

Metcalfe, T. S., Chaplin, W. J., Appourchaux, T., García, R. A., Basu, S., Brandão, I., Creevey, O. L., Deheuvels, S., Doğan, G., Eggenberger, P., Karoff, C., Miglio, A., Stello, D., Yıldız, M., Çelik, Z., Antia, H. M., Benomar, O., Howe, R., Régulo, C., Salabert, D., Stahn, T., Bedding, T. R., Davies, G. R., Elsworth, Y., Gizon, L., Hekker, S., Mathur, S., Mosser, B., Bryson, S. T., Still, M. D., Christensen-Dalsgaard, J., Gilliland, R. L., Kawaler, S. D., Kjeldsen, H., Ibrahim, K. A., Klaus, T. C., and Li, J. (2012). Asteroseismology of the Solar Analogs 16 Cyg A and B from Kepler Observations. , 748(1):L10.

Mombarg, J. S. G., Aerts, C., Van Reeth, T., and Hey, D. (2024). Estimates of (convective core) masses, radii, and relative ages for ∼14 000 Gaia-discovered gravity-mode pulsators monitored by TESS. , 691:A131.

O'Brien, M. W., Tremblay, P. E., Klein, B. L., Koester, D., Melis, C., Bédard, A., Cukanovaite, E., Cunningham, T., Doyle, A. E., Gänsicke, B. T., Gentile Fusillo, N. P., Hollands, M. A., McCleery, J., Pelisoli, I., Toonen, S., Weinberger, A. J., and Zuckerman, B. (2024). The 40 pc sample of white dwarfs from Gaia. , 527(3):8687–8705.

Pala, A. F., Gänsicke, B. T., Belloni, D., Parsons, S. G., Marsh, T. R., Schreiber, M. R., Breedt, E., Knigge, C., Sion, E. M., Szkody, P., Townsley, D., Bildsten, L., Boyd, D., Cook, M. J., De Martino, D., Godon, P., Kafka, S., Kouprianov, V., Long, K. S., Monard, B., Myers, G., Nelson, P., Nogami, D., Oksanen, A., Pickard, R., Poyner, G., Reichart, D. E., Rodriguez Perez, D., Shears, J., Stubbings, R., and Toloza, O. (2022). Constraining the evolution of cataclysmic variables via the masses and accretion rates of their underlying white dwarfs. , 510(4):6110–6132.

Pala, A. F., Gänsicke, B. T., Townsley, D., Boyd, D., Cook, M. J., De Martino, D., Godon, P., Haislip, J. B., Henden, A. A., Hubeny, I., Ivarsen, K. M., Kafka, S., Knigge, C., LaCluyze, A. P., Long, K. S., Marsh, T. R., Monard, B., Moore, J. P., Myers, G., Nelson, P., Nogami, D., Oksanen, A., Pickard, R., Poyner, G., Reichart, D. E., Rodriguez Perez, D., Schreiber, M. R., Shears, J., Sion, E. M., Stubbings, R., Szkody, P., and Zorotovic, M. (2017). Effective temperatures of cataclysmic-variable white dwarfs as a probe of their evolution. , 466(3):2855–2878.

Paxton, B., Bildsten, L., Dotter, A., Herwig, F., Lesaffre, P., and Timmes, F. (2011a). Modules for Experiments in Stellar Astrophysics (MESA). , 192(1):3.

Paxton, B., Bildsten, L., Dotter, A., Herwig, F., Lesaffre, P., and Timmes, F. (2011b). Modules for Experiments in Stellar Astrophysics (MESA). , 192(1):3.

Paxton, B., Cantiello, M., Arras, P., Bildsten, L., Brown, E. F., Dotter, A., Mankovich, C., Montgomery, M. H., Stello, D., Timmes, F. X., and Townsend, R. (2013a). Modules for Experiments in Stellar Astrophysics (MESA): Planets, Oscillations, Rotation, and Massive Stars. , 208(1):4.

Paxton, B., Cantiello, M., Arras, P., Bildsten, L., Brown, E. F., Dotter, A., Mankovich, C., Montgomery, M. H., Stello, D., Timmes, F. X., and Townsend, R. (2013b). Modules for Experiments in Stellar Astrophysics (MESA): Planets, Oscillations, Rotation, and Massive Stars. , 208(1):4.

Paxton, B., Marchant, P., Schwab, J., Bauer, E. B., Bildsten, L., Cantiello, M., Dessart, L., Farmer, R., Hu, H., Langer, N., Townsend, R. H. D., Townsley, D. M., and Timmes, F. X. (2015a). Modules for Experiments in Stellar Astrophysics (MESA): Binaries, Pulsations, and Explosions. , 220(1):15.

Paxton, B., Marchant, P., Schwab, J., Bauer, E. B., Bildsten, L., Cantiello, M., Dessart, L., Farmer, R., Hu, H., Langer, N., Townsend, R. H. D., Townsley, D. M., and Timmes, F. X.

(2015b). Modules for Experiments in Stellar Astrophysics (MESA): Binaries, Pulsations, and Explosions. , 220(1):15.

Paxton, B., Schwab, J., Bauer, E. B., Bildsten, L., Blinnikov, S., Duffell, P., Farmer, R., Goldberg, J. A., Marchant, P., Sorokina, E., Thoul, A., Townsend, R. H. D., and Timmes, F. X. (2018a). Modules for Experiments in Stellar Astrophysics (MESA): Convective Boundaries, Element Diffusion, and Massive Star Explosions. , 234(2):34.

Paxton, B., Schwab, J., Bauer, E. B., Bildsten, L., Blinnikov, S., Duffell, P., Farmer, R., Goldberg, J. A., Marchant, P., Sorokina, E., Thoul, A., Townsend, R. H. D., and Timmes, F. X. (2018b). Modules for Experiments in Stellar Astrophysics (MESA): Convective Boundaries, Element Diffusion, and Massive Star Explosions. , 234(2):34.

Paxton, B., Smolec, R., Schwab, J., Gautschy, A., Bildsten, L., Cantiello, M., Dotter, A., Farmer, R., Goldberg, J. A., Jermyn, A. S., Kanbur, S. M., Marchant, P., Thoul, A., Townsend, R. H. D., Wolf, W. M., Zhang, M., and Timmes, F. X. (2019a). Modules for Experiments in Stellar Astrophysics (MESA): Pulsating Variable Stars, Rotation, Convective Boundaries, and Energy Conservation. , 243(1):10.

Paxton, B., Smolec, R., Schwab, J., Gautschy, A., Bildsten, L., Cantiello, M., Dotter, A., Farmer, R., Goldberg, J. A., Jermyn, A. S., Kanbur, S. M., Marchant, P., Thoul, A., Townsend, R. H. D., Wolf, W. M., Zhang, M., and Timmes, F. X. (2019b). Modules for Experiments in Stellar Astrophysics (MESA): Pulsating Variable Stars, Rotation, Convective Boundaries, and Energy Conservation. , 243(1):10.

Pepper, B. T., Istrate, A. G., Romero, A. D., and Kepler, S. O. (2022). The impact of the uncertainties in the $^{12}C(\alpha, \gamma)^{16}O$ reaction rate on the evolution of low- to intermediate-mass stars. , 513(1):1499–1512.

Peters, G. J. and Hirschi, R. (2013). The Evolution of High-Mass Stars. In Oswalt, T. D. and Barstow, M. A., editors, *Planets, Stars and Stellar Systems. Volume 4: Stellar Structure and Evolution*, volume 4, page 447.

Prialnik, D. (2009). *An Introduction to the Theory of Stellar Structure and Evolution*.

Ratnasingam, R. P., Edelmann, P. V. F., and Rogers, T. M. (2019). Onset of non-linear internal gravity waves in intermediate-mass stars. , 482(4):5500–5512.

Ratnasingam, R. P., Edelmann, P. V. F., and Rogers, T. M. (2020). Two-dimensional simulations of internal gravity waves in the radiation zones of intermediate-mass stars. , 497(4):4231–4245.

Ratnasingam, R. P., Rogers, T. M., Chowdhury, S., Handler, G., Vanon, R., Varghese, A., and Edelmann, P. V. F. (2023). Internal gravity waves in massive stars. II. Frequency analysis across stellar mass. , 674:A134.

Renedo, I., Althaus, L. G., Miller Bertolami, M. M., Romero, A. D., Córsico, A. H., Rohrmann, R. D., and García-Berro, E. (2010). New Cooling Sequences for Old White Dwarfs. , 717(1):183–195.

Rider, W. J. and Knoll, D. A. (1999). Time Step Size Selection for Radiation Diffusion Calculations. *Journal of Computational Physics*, 152(2):790–795.

Roberts, E. K., Tremblay, P.-E., O'Brien, M. W., Bédard, A., Cunningham, T., Byrne, C. M., and Cukanovaite, E. (2025). Comparison of methods used to derive the Galactic star formation history from white dwarf samples. , 538(4):2548–2561.

Rogers, T. M. (2015). On the Differential Rotation of Massive Main-sequence Stars. , 815(2):L30.

Rogers, T. M., Lin, D. N. C., McElwaine, J. N., and Lau, H. H. B. (2013). Internal Gravity Waves in Massive Stars: Angular Momentum Transport. , 772(1):21.

Rogers, T. M. and McElwaine, J. N. (2017). On the Chemical Mixing Induced by Internal Gravity Waves. , 848(1):L1.

Rohrmann, R. D., Althaus, L. G., and Kepler, S. O. (2011). Lyman α wing absorption in cool white dwarf stars. , 411(2):781–791.

Rosseland, S. and Randers, G. (1938). On the Stability of Pulsating Stars. *Astrophysica Norvegica*, 3:71.

Salaris, M. (2009). White dwarf cosmochronology: Techniques and uncertainties. In Mamajek, E. E., Soderblom, D. R., and Wyse, R. F. G., editors, *The Ages of Stars*, volume 258, pages 287–298.

Salaris, M., Blouin, S., Cassisi, S., and Bedin, L. R. (2024). Ne22 distillation and the cooling sequence of the old metal-rich open cluster NGC 6791. *arXiv e-prints*, page arXiv:2403.02790.

Salaris, M. and Cassisi, S. (2017). Chemical element transport in stellar evolution models. *Royal Society Open Science*, 4(8):170192.

Salaris, M., Cassisi, S., Pietrinferni, A., and Hidalgo, S. (2022). The updated BASTI stellar evolution models and isochrones - III. White dwarfs. , 509(4):5197–5208.

Salaris, M., Cassisi, S., Pietrinferni, A., Kowalski, P. M., and Isern, J. (2010). A Large Stellar Evolution Database for Population Synthesis Studies. VI. White Dwarf Cooling Sequences. , 716(2):1241–1251.

Salaris, M., Domínguez, I., García-Berro, E., Hernanz, M., Isern, J., and Mochkovitch, R. (1997). The Cooling of CO White Dwarfs: Influence of the Internal Chemical Distribution. , 486(1):413–419.

Schultz, W. C., Bildsten, L., and Jiang, Y.-F. (2022). Stochastic Low-frequency Variability in Three-dimensional Radiation Hydrodynamical Models of Massive Star Envelopes. , 924(1):L11.

Schultz, W. C., Bildsten, L., and Jiang, Y.-F. (2023). Turbulence-supported Massive Star Envelopes. , 951(2):L42.

Segretain, L. (1996). Three-body crystallization diagrams and the cooling of white dwarfs. , 310:485–488.

Smartt, S. J. (2009). Progenitors of Core-Collapse Supernovae. , 47(1):63–106.

Stephens, D., Herwig, F., Woodward, P., Denissenkov, P., Andrassy, R., and Mao, H. (2021). 3D1D hydro-nucleosynthesis simulations - I. Advective-reactive post-processing method and its application to H ingestion into He-shell flash convection in rapidly accreting white dwarfs. , 504(1):744–760.

Straniero, O., Domínguez, I., Imbriani, G., and Piersanti, L. (2003). The Chemical Composition of White Dwarfs as a Test of Convective Efficiency during Core Helium Burning. , 583(2):878–884.

Thompson, W., Herwig, F., Woodward, P. R., Mao, H., Denissenkov, P., Bowman, D. M., and Blouin, S. (2024). 3D hydrodynamic simulations of massive main-sequence stars - II. Convective excitation and spectra of internal gravity waves. , 531(1):1316–1337.

Tremblay, P.-E., Fontaine, G., Gentile Fusillo, N. P., Dunlap, B. H., Gänsicke, B. T., Hollands, M. A., Hermes, J. J., Marsh, T. R., Cukanovaite, E., and Cunningham, T. (2019). Core crystallization and pile-up in the cooling sequence of evolving white dwarfs. , 565(7738):202–205.

Tremblay, P. E., Kalirai, J. S., Soderblom, D. R., Cignoni, M., and Cummings, J. (2014). White Dwarf Cosmochronology in the Solar Neighborhood. , 791(2):92.

Vanon, R., Edelmann, P. V. F., Ratnasingam, R. P., Varghese, A., and Rogers, T. M. (2023). Three-dimensional Simulations of Massive Stars. II. Age Dependence. , 954(2):171.

Varghese, A., Ratnasingam, R. P., Vanon, R., Edelmann, P. V. F., and Rogers, T. M. (2023). Chemical Mixing Induced by Internal Gravity Waves in Intermediate-mass Stars. , 942(1):53.

Venner, A., Blouin, S., Bédard, A., and Vanderburg, A. (2023). A crystallizing white dwarf in a sirius-like quadruple system. , 523(3):4624–4642.

Verma, K., Faria, J. P., Antia, H. M., Basu, S., Mazumdar, A., Monteiro, M. J. P. F. G., Appourchaux, T., Chaplin, W. J., García, R. A., and Metcalfe, T. S. (2014). Asteroseismic Estimate of Helium Abundance of a Solar Analog Binary System. , 790(2):138.

von Hippel, T., Moss, A., Kloc, I., Moticska, N., Sargent, J., Robinson, E., Stenning, D., van Dyk, D., Jeffery, E., Fouesneau, M., and Bailer-Jones, C. (2020). A catalog of 159,238 white dwarf ages. In Barstow, M. A., Kleinman, S. J., Provencal, J. L., and Ferrario, L., editors, *White Dwarfs as Probes of Fundamental Physics: Tracers of Planetary, Stellar and Galactic Evolution*, volume 357, pages 188–191.

Vorberger, J., Graziani, F., Riley, D., Baczewski, A. D., Baraffe, I., Bethkenhagen, M., Blouin, S., Böhme, M. P., Bonitz, M., Bussmann, M., Casner, A., Cayzac, W., Celliers, P., Chabrier, G., Chamel, N., Chapman, D., Chen, M., Clérouin, J., Collins, G., Coppari, F., Döppner, T., Dornheim, T., Fletcher, L. B., Gericke, D. O., Glenzer, S., Goncharov, A. F., Gregori, G., Hamel, S., Hansen, S. B., Hartley, N. J., Hu, S., Hurricane, O. A., Karasiev, V. V., Kas, J. J., Kettle, B., Kluge, T., Knudson, M. D., Kononov, A., Konôpkov á, Z., Kraus, D., Kritcher, A., Malko, S., Massacrier, G., Militzer, B., Moldabekov, Z. A., Murillo, M. S., Nagler, B., Nettelmann, N., Neumayer, P., Ofori-Okai, B. K., Oleynik, I. I., Preising, M., Pribram-Jones, A., Ramazanov, T., Ravasio, A., Redmer, R., Rethfeld, B., Robinson, A. P. L., Röpke, G., Soubiran, F., Starrett, C. E., Steinle-Neumann, G.,

Sterne, P. A., Tanaka, S., Thompson, A. P., Trickey, S. B., Vinci, T., Vinko, S. M., Wang, L., White, A. J., White, T. G., Zastrau, U., Zurek, E., and Tolias, P. (2025). Roadmap for warm dense matter physics. *arXiv e-prints*, page arXiv:2505.02494.

Weiss, A. and Ferguson, J. W. (2009). New asymptotic giant branch models for a range of metallicities. , 508(3):1343–1358.

Winget, D. E., Hansen, C. J., Liebert, J., van Horn, H. M., Fontaine, G., Nather, R. E., Kepler, S. O., and Lamb, D. Q. (1987). An Independent Method for Determining the Age of the Universe. , 315:L77.

Woodward, P. R., Herwig, F., and Lin, P.-H. (2015). Hydrodynamic Simulations of H Entrainment at the Top of He-shell Flash Convection. , 798(1):49.

Woodward, P. R., Lin, P.-H., Mao, H., Andrassy, R., and Herwig, F. (2019). Simulating 3-D Stellar Hydrodynamics using PPM and PPB Multifluid Gas Dynamics on CPU and CPU+GPU Nodes. In *Journal of Physics Conference Series*, volume 1225 of *Journal of Physics Conference Series*, page 012020. IOP.

Woosley, S. E., Heger, A., and Weaver, T. A. (2002). The evolution and explosion of massive stars. *Reviews of Modern Physics*, 74(4):1015–1071.

Appendix A

Additional Information

A.1 Subsurface Convective Boundary

We analyze the subsurface convective boundary and overshoot region for run M424 using temperature gradient profiles and statistical moments of the radial velocity field. The left panel of Figure A.1 shows that from the interior toward the surface, the temperature gradient ∇ follows the radiative gradient $\nabla_{\rm rad}$ up to 3660Mm. Beyond this point, ∇ increases toward $\nabla_{\rm ad}$ and exceeds the Schwarzschild boundary at 3813 Mm (where $\nabla_{\rm rad} = \nabla_{\rm ad}$). Inside the subsurface convection zone, $\nabla > \nabla_{\rm ad}$, indicating superadiabatic conditions where convection cannot efficiently transport heat, and radiation contributes to energy transport.

Following the methodology of Herwig et al. (2023), which identifies convective boundaries through extrema in the product of Skew $\times$ Kurtosis, we determine from the right panel of Figure A.1 that the core convective boundary for run M424 is located at 1460 Mm, while the subsurface convection zone boundary is positioned at 3733 Mm. The left panel shows that going from surface towards the center, velocities decrease steeply until 3660Mm, confirming this region is well within the radiative zone and beyond the overshoot region from the Schwarzschild boundary.

A.2 Envelope Convection Simulation: M484

The M484 simulation focuses exclusively on the envelope convection zone. This convection region is spatially confined, with inner and outer boundaries located at 3850Mm and 4100Mm, respectively, making it susceptible to boundary effects. No heating was applied at the inner boundary during the simulation initialization. The cooling rate at the outer boundary was set equal to the core heating rate used in comparative simulations.

Figure A.2 (left panel) shows higher convective velocities in M484 as compared to the

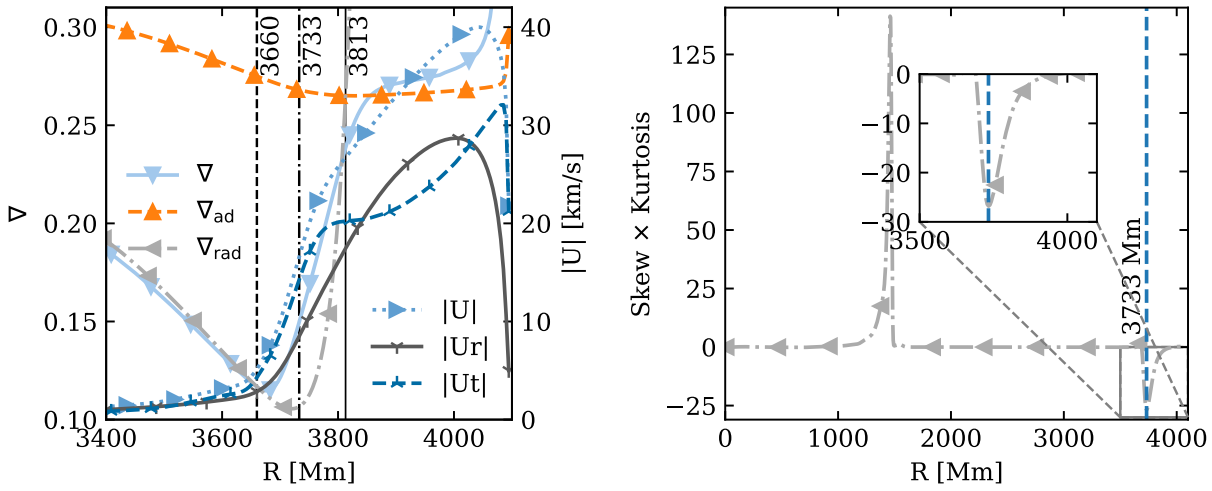

Figure A.1: *Left*: Radial profiles of the actual temperature gradient (∇; light blue solid line with downward triangles), adiabatic temperature gradient ($\nabla_{\rm ad}$; orange dashed line with upward triangles) and radiative temperature gradient ($\nabla_{\rm rad}$; grey dot-dashed line with leftward triangles) at dump 4800 ($\approx 4779\,$h) for run M424 near the subsurface convection zone. The secondary y-axis displays total velocity magnitude ($|{\rm U}|$), radial velocity magnitude ($|{\rm U_r}|$) and tangential velocity magnitude ($|{\rm U_t}|$) at dump 4800. *Right*: Radial profile of Skew $\times$ Kurtosis of radial velocity $\rm U_r$ for run M424. The vertical dashed dark blue line marks the extremum at 3733Mm, with an expanded view of this region shown in the inset.

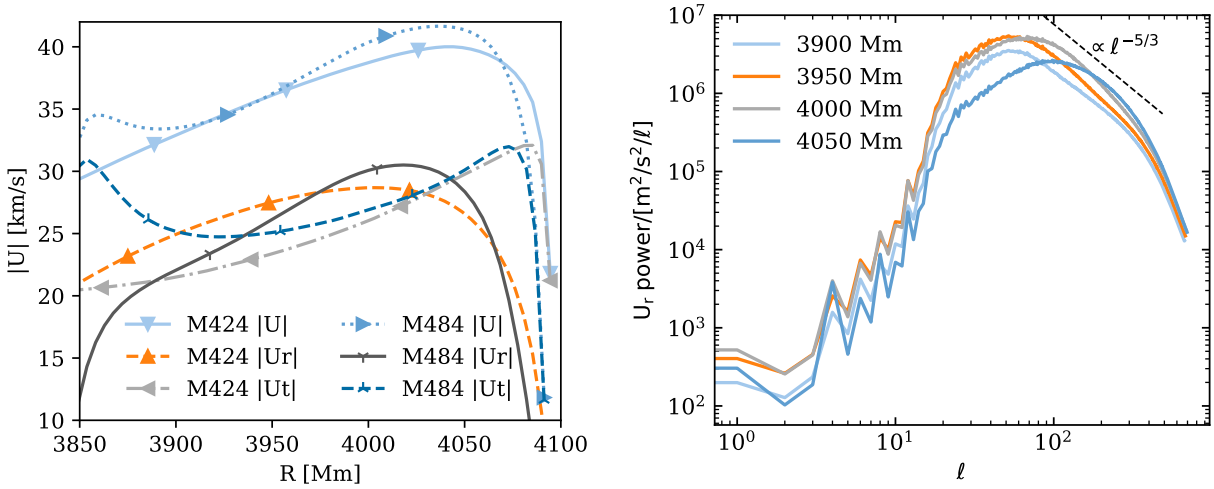

Figure A.2: (*Left*): Velocity magnitude (|U|), radial velocity magnitude (|Ur|) and tangential velocity magnitude (|Ut|) profiles of the run M424 at dump 4800 and the run M484 at dump 2600 within the envelope convection zone. (*Right*): Radial velocity spatial spectra for simulation M484 at various radial coordinates inside the subsurface convection zone, averaged over last 100 dumps.

fullstar run M424. Velocity magnitude differences are evident near the inner boundary because of reflective boundary conditions.

Despite these boundary artifacts, the spatial spectrum (Figure A.2, right panel)) reveals a scale separation between energy injection and dissipation scales. The energy spectrum follows the Kolmogorov power law proportional to $\ell^{-5/3}$, indicating the development of a turbulent cascade within the simulated convection zone.

A.3 Convergence

The mock luminosity power spectra of the fullstar run with two different grid resolutions 1792^3 and 896^3 demonstrate notable convergence characteristics in Figure A.3.

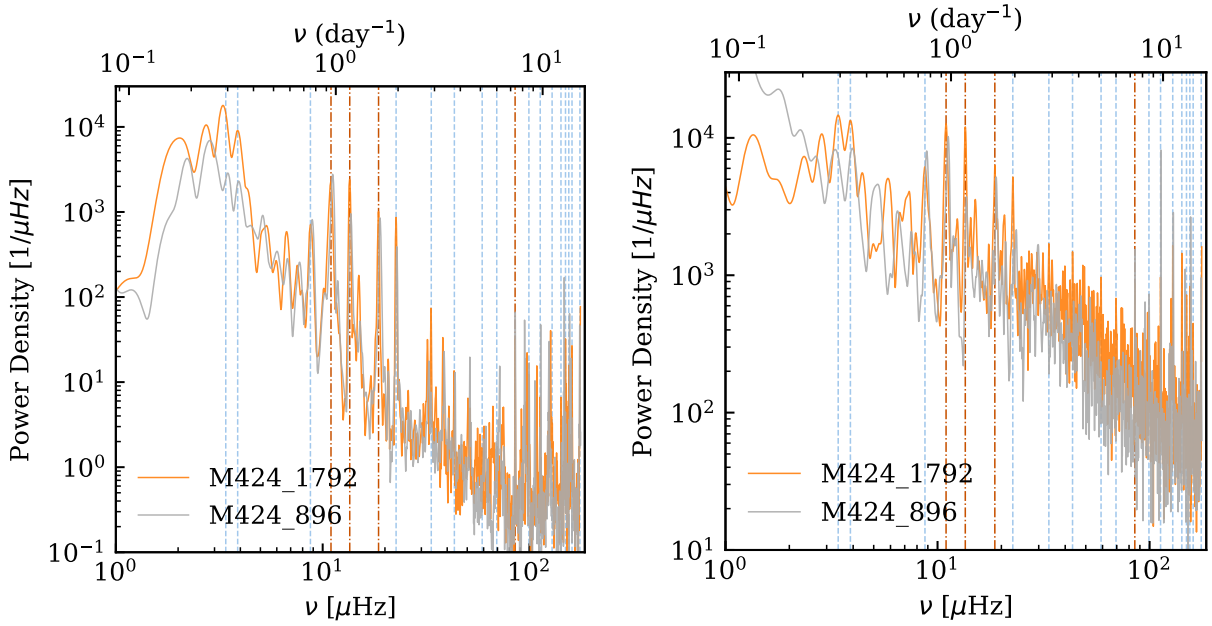

Figure A.3: Mock luminosity power spectra $\mathcal{L}_{\text{mock}}$ comparison similar to Figure 3.11 of the fullstar run with resolution 1792^3 presented in the study and with a coarser grid resolution of 896^3.